METAL PHOSPHONATE SOLIDS AND LANGMUIR-BLODGETT FILMS:
STRUCTURAL AND PHYSICAL CHARACTERIZATION

By

GAIL E. FANUCCI

To my grandparents:

Leona and Francis Reha
and
Mary and Steve Lesavage

The freedom and the opportunity to daydream are important. The freedom and the opportunity to explore paths that others don't appreciate, or even disapprove of are important. Taking the time to understand generalities and to develop a perspective is important. The freedom not to compete is important. The freedom to arouse – and survive – controversy is important.

Exploration has its dangers. Tackling the unknown can easily end in failure. Explorers rarely get their name attached to a specific contribution, because they jump from one thing to another before everyone sees their point and because it is easier to remember those who exploit an idea tens or hundreds of different variations than those who originate it only once. Today this can be deadly in funding and tenure decisions. It is a tribute to those who set the climate at the time when we were young that we did not unduly suffer for it.

Yet it is not nostalgia for the "good old times" that prompts me to underscore this point. It is simply the recognition of a simple fact. If we forget that to find and shape an idea before it comes common property is at least as important as a specific result, we as a scientific community – perhaps we as a society – are on a self-defeating path. A society that increasingly thinks only in terms of directing and channeling craftsmanship in the pursuit of clearly visible goals is cutting itself off from the source of all innovation.

<div align="right">

Oleg Jardesky
(from *Biological NMR Spectroscopy*,
Mackley, J.L., Opella, S.J. Eds.; Oxford
University Press, Oxford 1997.)

</div>

With this freedom always comes the danger of failure, and I feel that Dan had always kept a close eye on me to ensure that I did not travel down that road, and for this I am also thankful.

Additionally there are many family members whose help and guidance I will always be thankful for. For their support in many ways, I thank my mother and father, Joyce and Steve Lesavage, my grandparents, Francis and Leona Reha and Mary and Steve Lesavage, my cousin Robert Czaja (who in many ways is a younger brother to me), my husband Ted and my in-laws Ted and Diane Fanucci.

TABLE OF CONTENTS

LIST OF TABLES

LIST OF FIGURES

Abstract of Dissertation Presented to the Graduate School
of the University of Florida in Partial Fulfillment of the
Requirements for the Degree of Doctor of Philosophy

METAL PHOSPHONATE SOLIDS AND LANGMUIR-BLODGETT FILMS:
STRUCTURAL AND PHYSICAL CHARACTERIZATION

By

Gail E. Fanucci

May, 1999

Chairman: Daniel R. Talham
Major Department: Chemistry

Previously, divalent metal phosphonate Langmuir-Blodgett (LB) films have been shown to contain a two-dimensional (2D) continuous inorganic lattice analogous to that of known solid-state divalent metal phosphonate compounds. The goal now is to understand how to incorporate different metal phosphonate 2D lattice structures, such as those of the trivalent metal phosphonates, into the polar-regions of organophosphonate LB films. The results demonstrate that it is possible to prepare trivalent metal phosphonate LB and that the subphase pH plays a crucial role in determining whether or not the 2D lattice crystallizes within the polar regions of the films. Additionally, solid-state ^{31}P magic angle spinning (MAS) NMR techniques have been used to study the structure and in-plane bonding arrangement of these films, and the results confirm that the 2D continuous lattice structure of the lanthanum octadecylphosphonate LB film is isostructural with that of the analogous lanthanum butylphosphonate solid-state material.

A second goal is to understand how to incorporate larger functionalized organic groups into the non-polar regions of these organophosphonate LB films, and here a study of phenoxy

substituted organophosphonate LB films was performed. These results show that the position of the phenoxy group along the alkyl chain is an important parameter that affects the quality and processibility of the Langmuir monolayers, which thus affects the deposition of the films onto a solid support and the concurrent ability to form a crystalline 2D metal phosphonate lattice. Magnetic studies of a phenoxy substituted manganese phosphonate LB film show that it is possible to incorporate this aryl group within the metal phosphonate films without disrupting the magnetic exchange pathways of the inorganic continuous lattice network. As part of the efforts to understand the magnetic properties of the metal phosphonate LB films, antiferromagnetic resonance (AFMR) studies of a series of manganese phosphonate polycrystalline materials have been performed.

CHAPTER 1
LAYERED METAL PHOSPHONATES: POLYCRYSTALLINE SOLIDS AND THIN FILMS

Low-Dimensional Materials

Recently, both chemists and physicists have shown great interest in low-dimensional materials, whereby low-dimensional refers to those materials that possess either structural or physical properties that are strongly anisotropic in one or two dimensions.[1-3] Such materials are often referred to as 'quasi'-1D or 'quasi'-2D systems since, in reality, they are part of a three dimensional solid, but their characteristic properties appear to exist in only chains or sheets, respectively. Structurally, low-dimensional materials are of interest for their intercalation properties and phase transitions, while physical properties such as magnetism, optical response, conductivity and superconductivity that these materials exhibit in only one or two dimensions are often useful in many technological applications or as models for fundamental physical theories.[4]

The work presented in this dissertation is concerned with the 'quasi'-2D structural and physical properties of layered metal phosphonate solids and metal phosphonate Langmuir-Blodgett (LB) films. Presented in this chapter is general background information pertinent to the research described in the subsequent chapters. First, structures of various layered metal phosphates and phosphonates are presented followed by a discussion of the magnetic properties of some metal phosphonates, including a discussion of low-dimensional magnetism. The introductory material will conclude with a description of metal phosphonate thin films which include spontaneously absorbed monolayer and multilayer films and metal phosphonate Langmuir-Blodgett films, the latter having been pioneered by efforts of the Talham research group.[5-10]

1

Solid-State Metal Phosphates and Phosphonates

Metal phosphonate chemistry has attracted a great deal of attention in the past two decades primarily because these materials possess separate organic and inorganic components and their chemistry offers a possible route to supramolecular assemblies with the ability to design structures possessing specific properties.[11,12] These attractive features result from the relatively mild reaction conditions used to prepare metal phosphonate compounds. These characteristics lead to the ability to incorporate functionalized organic moieties into the materials while retaining both the structure of the inorganic phosphonate lattice and the identity and function of the organic groups. Metal phosphonates have attracted interest because of their potential applications as ion-exchangers, sorbents, proton conductors, nonlinear optical materials, photochemically active materials, catalysts, hosts for intercalation reactions, and models for low-dimensional magnetic phenomena.[11,13] A variety of metal phosphonate compounds have been formed from both simple and more complex organophosphonic acids, and their structures range from linear chains[14,15] and layered sheets,[12,16,17] to porous three dimensional pillared assemblies.[18,19] The structures of a few of these materials are described in detail below.

Layered Structures

Layered metal phosphates and phosphonates are examples of 'quasi'-2D materials that form a class of inorganic solid-state compounds containing an inorganic lattice of an essentially planar array of metal ions that are coordinated from above and below by three of the phosphate / phosphonate oxygens. In the case of the *phosphate* ligands, the fourth phosphate oxygen, which is protonated, points into the interlayer space and is often accompanied by an absorbed water molecule. Likewise, for the *phosphonates*, it is the organic moiety, which is bonded directly to the phosphorus atom, that projects into the regions between the planes of the inorganic lattice

network. In both cases, the resulting materials are layered, and as examples, the structures of α-zirconium phosphate[20] and zirconium phenylphosphonate[21] are given in Figure 1-1.

Within the class of layered metal phosphates, the most extensively studied systems consist of Group 4 (Ti^{4+}, Zr^{4+}, Hf^{4+}), Group 5 (VO^{2+}, Nb^{5+}, Ta^{5+}), Group 14 (Ge^{4+}, Sn^{4+}, Pb^{4+}) and Group 15 (Sb^{4+}) metal ions.[13] Most of the above mentioned metals form layered phosphate structures very similar to that of α-zirconium phosphate, $Zr(HOPO_3)_2 \cdot H_2O$ (the most notable exception is the structure of $(VO)_2P_2O_7$, which is described in more detail later). These solid-state materials are of interest due to the ion-exchange, 'molecular sieve', intercalation, and catalytic processes that can occur in the interlamellar channels.

The metal phosphonates, on the other hand, with the phosphate O-H group replaced by an organic substituent, are of interest for their 'quasi'-2D alternating organic and inorganic layered structural motif. These materials have been studied as models for low-dimensional magnetic systems[22,23] and as mixed organic/inorganic materials where potential optical, nonlinear optical and electronic properties have been associated with the organic layers.[24-27]

Layered metal phosphonates can be formed with a variety of metal ions and phosphonic acids.[14,16,19,28-41] These metal ions include alkaline earth metals, transition metals, trivalent lanthanide metals and the previously mentioned tetravalent Group IV ions. Furthermore, the range of organophosphonic acids used encompasses both simple alkyl/aryl phosphonic acids[16] and more complex/functionalized phosphonic acids.[15,18,42] Typically, layered metal phosphonates are formed as polycrystalline powders by aqueous precipitation reactions where stoichiometric amounts of the metal salts and phosphonic acids are mixed together at the appropriate pH. In cases where simple alkyl or aryl phosphonic acids are used, the resulting metal phosphonate structures are similar in that they are composed of alternating 2D layers of organic and inorganic networks, but these structures differ in the packing geometries of the organic groups and the mode of metal-oxygen-phosphorus bonding. Usually, the bonding

requirements of the metal ions dictate the in-plane metal phosphonate lattice structure,[12] which is sometimes rather insensitive to the identity of the organic groups. This point is illustrated by the structure of zirconium phenylphosphonate (Figure 1-1) which is obtained simply by attachment of organic phenyl rings to the α-zirconium phosphate lattice.

For organizational purposes, the following presentation divides the structures of layered metal phosphonates with simple alkyl or aryl phosphonic acids into seven categories that are summarized in Table 1-1. The structures of each of these groups are briefly described below. Figures 1-2 through 1-6 provide in-plane and cross-sectional views of the structures of select metal phosphonate compounds which illustrate the metal–oxygen–phosphorus connectivity and the alternating organic/inorganic layered motif, respectively.

Zirconium phosphonates

The in-plane arrangement of the zirconium phosphonate[43] structure (Figure 1-2) consists of a triangular array of metal ions lying approximately in a plane. The phosphonate groups alternate above and below the plane of the metal ions and occupy the center of the triangles. The three phosphate oxygens that are oriented towards the metal planes bond to three different metal ions with the organic group directed nearly perpendicular to the metal planes. The resultant structure can be described as a two-dimensional continuous inorganic lattice since it extends infinitely in two spatial directions. In addition to Zr^{4+}, the layered Fe(III) phenylphosphonate compound has been shown to adopt a similar continuous lattice structure.[14]

Divalent metal phosphonates

Most divalent metal phosphonates form a homologous series of layered solid-state compounds that crystallize in the space group $Pmn2_1$ with formula $M(O_3PR)H_2O$ where M =
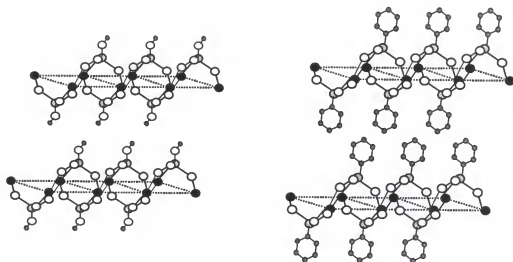
Figure 1-1. Idealized cross sectional views of the structures of (left) α-zirconium phosphonate and (right) zirconium phenyl phosphonate.
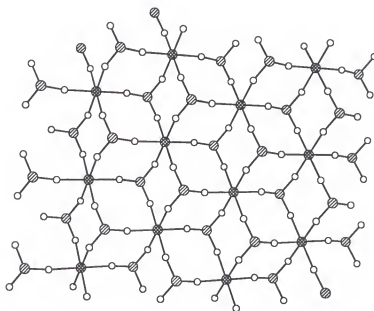
Figure 1-2. In-plane structure of α-zirconium phosphate. Key: oxygen, open circles; phosphorus, thatched circles; zirconium, cross-hatched circles. Crystallographic data are taken from reference 40.

Table 1-1. Structural Categories of Layered Metal Phosphonates with Simple Alkyl and Aryl Phosphonic Acids

Formula	Metal (M)	R	Coordination Number	Space group	Ref.
$M(O_3PR)_2$	Zr^{4+}	C_6H_5	6	$C2/c$	21, 40
$MH(O_3PR)_2$	Fe^{3+}	C_6H_5	6	$P\bar{1}$	14
$M(O_3PR)H_2O$	Mn^{2+}	C_6H_5	6	$Pmn2_1$	16
		$C_nH_{2n+1}, n = 1, 2$	6	$Pmn2_1$	16
	Mg^{2+}	C_6H_5	6	$Pmn2_1$	16
		$C_nH_{2n+1}, n = 1\text{-}12$	6	$Pmn2_1$	16
	Fe^{2+}	C_2H_5	6	$P1n1$	30
	Cr^{2+}	C_2H_5	6	$P1n1$	31
	Zn^{2+}	C_6H_5	6	$Pmn2_1$	16, 39
		$C_nH_{2n+1}, n = 1, 2$	6	$Pmn2_1$	16
	Co^{2+}	C_6H_5	6	$Pmn2_1$	40,41
	Cd^{2+}	C_6H_5	6	$Pmn2_1$	32
		CH_3	6	$Pna2_1$	32
$M(O_3PR)H_2O$	Cu^{2+}	CH_3	5	$P2_1/c$	38
		C_6H_5	5	$Pbca$	38
	Ca^{2+}	$C_nH_{2n+1}, n \leq 5$	7	$P2_1/c$	29
$M(HO_3PR)_2$	Ca^{2+}	$C_nH_{2n+1}, n > 5$	6	$P\bar{1}$	29
$M(HO_3PR)_2$	Ba^{2+}, Pb^{2+}	C_6H_5	8	$P2_1/c$	36
$MH(O_3PR)_2$	La^{3+},Ce^{3+},Sm^{3+}	CH_3	8	$P\bar{1}$	29
	La^{3+}	C_6H_5	8	$P\bar{1}$	37
		$CH_2C_6H_5$	8	$Pbcn$	37
$MO(O_3PR) \cdot xH_2O$	V^{4+}	$C_6H_5 \quad x = 1$	6	$C2/c$	33,46
		$C_nH_{2n+1}, n = 1,2 \ x=1.5$	6		33,47

Mg^{2+}, Mn^{2+}, Zn^{2+}, Cd^{2+}, Ni^{2+}, Fe^{2+}, Cr^{2+}, Co^{2+} and with R = phenyl and alkyl phosphonic acids (exceptions occur for some cadmium, iron and chromium salts which crystallize in different space groups, see Table 1-1).[16,30-32] In the $M(O_3PR)H_2O$ structure, the metal ions are coordinated in a distorted octahedral geometry by five phosphonate oxygens and one water molecule oxygen. The layered structural motif and the in-plane bonding geometry of zinc phenylphosphonate are shown in Figure 1-3. In this structure, four different phosphonate groups coordinate each metal ion, and each phosphonate group networks four different metal ions. The bonding motif of the $M(O_3PR)H_2O$ two-dimensional continuous inorganic lattice differs greatly from that of the α-zirconium structure. Here, one phosphonate oxygen is ligated to a unique metal ion while the remaining two oxygens chelate a second and also bridge to two other adjacent metal ions. The resultant 2D lattice structure consists of M atoms connected to four equivalent nearest neighbors by M-O-M linkages, whereas in the Zr phosphonates, each metal atom is connected to the next through the M-O-P-O-M linkages.

Copper phosphonates

Various copper phosphonate structures can be obtained depending upon the method of preparation.[15,19,38,44,45] However, the typical aqueous precipitation reaction used to form other divalent metal phosphonates produces a layered copper phosphonate structure with formula $Cu(O_3PR)H_2O$ where R = CH_3, C_2H_5 and C_6H_5, and in each case, the 5-coordinate copper atoms have a distorted tetragonal pyramidal geometry. Although the methyl and phenyl compounds crystallize in different space groups, they have the same coordination environment around the copper atoms.[38] In this 2D metal phosphonate continuous lattice (Figure 1-3), each phosphonate group bonds to four different copper atoms. One phosphonate oxygen bridges two copper ions in such a way that it produces the top of the pyramid in one site while occupying one of the base positions of the pyramid on the other metal site. The other phosphonate oxygens each ligate to

8
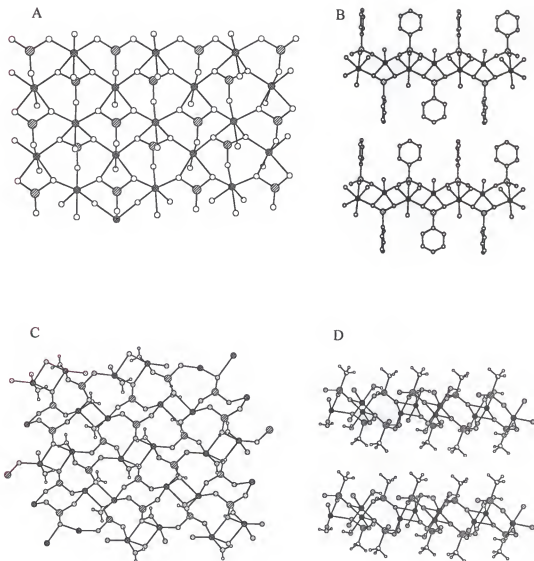
Figure 1-3. **(A)** In-plane and **(B)** cross-sectional view of the structure of zinc phenylphosphonate, $Zn(O_3PC_6H_5)H_2O$ (crystallographic data are taken from ref. 16) **(C)** In-plane and **(D)** cross-sectional view of the structure of $Cu(O_3PCH_3)H_2O$ (crystallographic data are taken from ref. 38). Key: oxygen, open circles; phosphorus, thatched circles; metal ions, cross-hatched or solid circles.
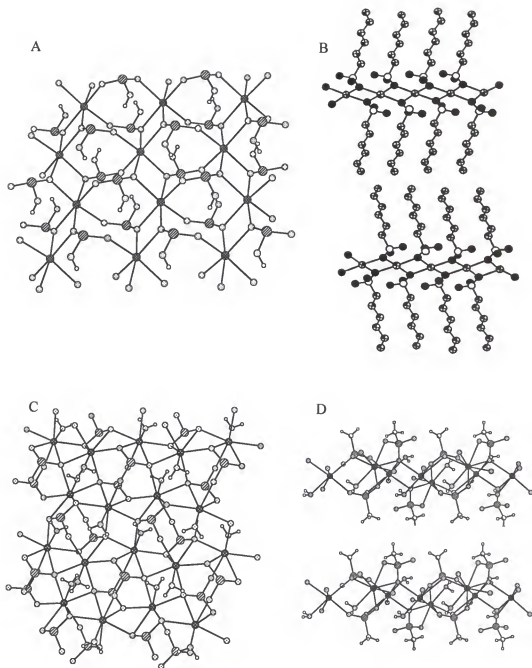
Figure 1-4. **(A)** In-plane and **(B)** cross-sectional view of the structure of calcium hexylphosphonate, $Ca(HO_3PC_6H_{13})_2$ (crystallographic data are taken from ref. 29) **(C)** In-plane and **(D)** cross-sectional view of the structure of $Ca(O_3PCH_3)H_2O$ (crystallographic data are taken from ref. 29). Key: oxygen, open circles; phosphorus, thatched circles; metal ions, cross-hatched or solid circles.

two other copper ions while hydrogen bonding to the coordinated water molecule on two other copper sites. The water molecules are coordinated to the copper atoms and occupy a basal position of the pyramidal coordination structure. In this structure, an extensive intra-plane hydrogen-bonding network is established between the coordinated water molecule and the phosphonate oxygens. When prepared in a Teflon cell of an autoclave, an anhydrous phase, α-$Cu(O_3PR)$, that contains a different metal–oxygen–phosphorus connectivity results.[44]

Calcium phosphonates

Two different calcium phosphonate structures are known and the resultant structure depends upon the identity of the organic group.[17,29] Calcium alklyphosphonates, $Ca(HO_3PC_nH_{2n+1})$ $n > 5$, are triclinic with the Ca atoms arranged in a sheet and coordinated by six phosphonate oxygens. One phosphonate oxygen is bonded to a proton and does not participate in the metal-oxygen-phosphorus inorganic lattice structure, which is closely related to the tetravalent metal phosphonate structure, $M(O_3PR)_2$. On the other hand, when n $\leq$ 5, the $Ca(O_3PC_nH_{2n+1})H_2O$ structure results where seven oxygens coordinate the calcium atoms in a distorted pentagonal bipyramidal geometry. Six oxygens originate from the phosphonate groups where one oxygen bridges three calcium ions and the seventh oxygen atom is from a coordinated water molecule. The in-plane and layered structures of both calcium phosphonates are depicted in Figure 1-4.

Barium and lead phosphonates

The crystal structures for lead and barium phenylphosphonate have recently been reported.[36] Both are isomorphous and crystallize in the C2/c space group with formula $M(HO_3PC_6H_5)_2$. The phosphonate groups use all their oxygens (one of which is protonated) to chelate and to bridge the metal ions forming a continuous inorganic lattice structure. The metal ions are eight-coordinate, and four different phosphonates interact with each metal ion. The in-

plane bonding arrangement and layered structure of barium phenyphosphonate are depicted in Figure 1-5. Although the barium and calcium phosphonate materials have the same empirical formula, $M(HO_3PR)_2$, their in-plane continuous inorganic lattice structures differ.

Trivalent lanthanide phosphonates

Layered structures with Ln^{III} metals (Ln = La, Ce, and Sm) can be formed with aryl- and alkylphosphonic acids.[29,37] These materials crystallize in the triclinic space group $P\bar{1}$ with formulas $MH(O_3PR)_2$. In this structure, the metal ions are eight-coordinate, and this coordination consists of oxygen atoms from four different phosphonate groups. Each phosphonate group interacts with four different metal centers. One oxygen chelates a single metal ion, while the other two oxygens both bond to a second metal where one bridges to a third metal and the other interacts through hydrogen bonding to an oxygen atom on a fourth metal center. The $MH(O_3PR)_2$ structure is another example of a 2D continuous inorganic lattice network and is depicted in Figure 1-5.

Vanadyl phosphonates

The vanadyl phosphonates represent a class of layered metal phosphonates that are not formed from aqueous precipitation reactions but rather are made by alcohol reduction of V_2O_5 in the presence of phosphonic acids or are grown hydrothermally.[33,34,46] For example, $VO(O_3PC_5H_6)H_2O$ can be prepared by mixing phenylphosphonic acid and V_2O_3 in a Teflon lined autoclave cell which is then sealed and heated to 200° C for 4 days.[33] A variety of vanadyl phosphonate structures are known, and the resultant structure depends upon the reaction conditions, the vandium starting material, and the identity of the phosphonic acid.[33,46-48] The in-plane and layered structure of $VO(O_3PC_5H_6)H_2O$ is depicted in Figure 1-6, where the chains of
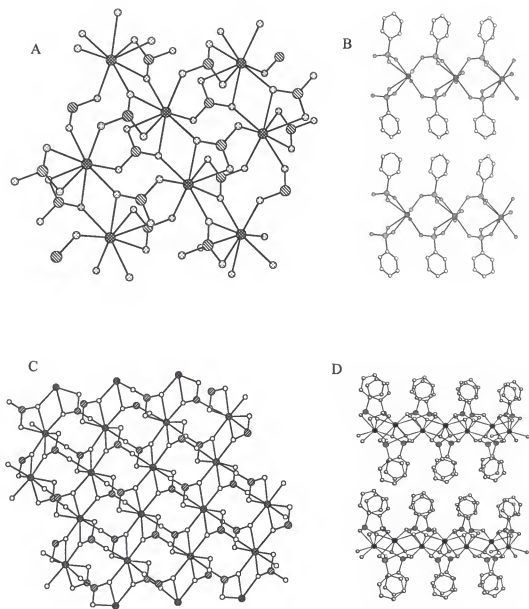
Figure 1-5. **(A)** In-plane and **(B)** cross-sectional view of the structure of barium phenylphosphonate, Ba(HO$_3$PC$_6$H$_5$)$_2$ (crystallographic data are taken from ref. 36) **(C)** In-plane and **(D)** cross-sectional view of the structure of LaH(O$_3$PC$_6$H$_5$)$_2$ (crystallographic data are taken from ref. 37). Key: oxygen, open circles; phosphorus, thatched circles; metal ions, cross-hatched or solid circles.
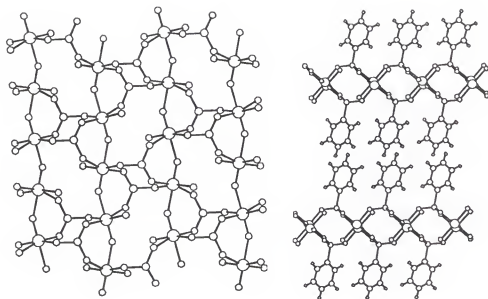
Figure 1-6. **(A)** In-plane and **(B)** cross-sectional view of the structure of vanadyl phenylphosphonate, $VO(O_3PC_6H_5)H_2O$ (crystallographic data are taken from ref. 46).

octahedrally coordinated metal ions are connected by the V=O--V linkages and the phosphonate oxygens bridge two successive vanadium ions in the chain with the third oxygen bridging to a neighboring chain. The third bridging oxygen is responsible for forming the 2D continuous lattice structure.

Non-Layered Structures

Although most aqueous preparations of metal phosphonates with simple alkyl or aryl phosphonic acids produce layered metal phosphonate structures, some non-layered phases with simple phosphonic acids have been prepared using hydrothermal or other traditional solid-state techniques. For example, the 'quasi'-1D $HFe(C_6H_5PO_3H)_4$ material has been formed by heating a mixture of phenylphosphonic acid and FeOCl in dichloromethane in a sealed Pyrex tube at 80° C for 24 h. The structure of this material consists of FeO_6 octahedra and $PO_3C_6H_5$ tetrahedra arranged in infinite chains.[14] In addition, a 3D channel-type structure for β-$Cu(O_3PCH_3)$ resulted
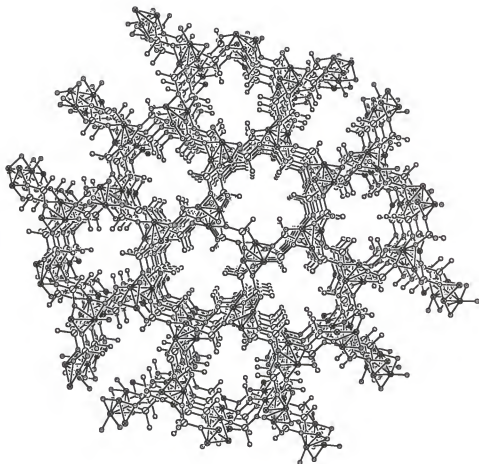
Figure 1-7. The 3D channel-type structure of β-Cu(O$_3$PCH$_3$). Crystallographic data are taken from ref. 19.

when α-Cu(O$_3$PCH$_3$) and water were heated in a Teflon cell of an autoclave at 200° C for 15 days.[19] This tubular type structure is depicted in Figure 1-7.

Other linear chain and three dimensional phosphonate structures have been formed with more complex functionalized phosphonic acids.[11] However, it appears that aqueous reactions of simple organophosphonic acids with metal salts carried out at moderate temperatures and ambient pressure result in the formation of metal phosphonate materials with layered structural motifs. Although layered metal phosphates and phosphonates have been studied for many years for their ion-exchange, sorbent, and intercalation properties, their chemistry is still rich today. However, more recent efforts focus on their chemical function and device applications that originate from the structural tunability of the inorganic lattice, the chemical diversity of the organic layers, and their overall structural and thermal stability.[11] New structures are frequently reported, and numerous examples of metal phosphonates prepared with more complex and functionalized phosphonic acids that form 3D channel structures now exist.

Metal Phosphonates as Magnetic Materials

In general, the magnetic properties of transition metal complexes and molecular based magnets have received tremendous attention in the past several years, with the major driving force being the desire to construct molecule based ferromagnets that order at or near room temperature.[1,49-51] In addition to this quest, novel magnetic materials, whether formed from either purely organic molecules or inorganic coordination compounds, or from combinations of the two, offer not only new materials with potential technological applications, but also allow for series of materials to be designed that provide a way of understanding how structure and magnetic properties are related.

Metal phosphonate solids, with separate organic and inorganic components, are suitable systems for studying such magnetostructural correlations, and this point was recently

demonstrated by Nocera and co-workers[48] who showed that the magnetic properties of a series of substituted vanadyl phenylphosphonates are correlated with the electron withdrawing effects of the organic substituents. In addition, metal phosphonates, because of their layered structures, can be used as models for studying low dimensional magnetic phenomenon.[22,23,52,53] The magnetic properties of metal phosphonates depend not only on the identity of the organic group, but also on the identity of the metal ions and the structure of the in-plane metal phosphonate lattice. The following sections provide an introduction to long-range magnetic order and low-dimensional magnetism. The magnetic properties of some copper, vanadyl and manganese phosphonates and phosphates are presented as examples of the types of magnetic interactions that exist in dimers, linear chains and ladders, and two-dimensional layers, respectively.

Introduction to Long-Range Magnetic Order

In compounds that possess unpaired electrons, there are essentially three ways that the unpaired electrons on one atom, which can collectively be referred to as the magnetic moment, can interact with those of its nearest neighbor.[49,50] These interactions are referred to as being paramagnetic, ferromagnetic or antiferromagnetic and are represented schematically in Figure 1-8. In the paramagnetic case, the orientations of the magnetic moments on neighboring atoms are independent of each other or are weakly interacting. Whereas in the ferromagnetic and antiferromagnetic cases, the neighboring moments strongly interact to be aligned parallel or antiparallel to one another, respectively.

A transition to long-range magnetic order means that in the absence of an applied external magnetic field, the magnetic moments on the nearest neighbor atoms over a relatively large domain will spontaneously align either parallel or antiparallel to one another at some critical temperature. The distance over which the spin alignments are correlated is called the magnetic correlation length, ξ. The temperature at which $\xi \to \infty$ is where spontaneous ordering

paramagnetic   ferromagnetic   antiferromagnetic
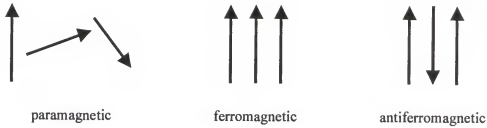
Figure 1-8. Representation of the spin vectors when the interactions between the moments are classified as paramagnetic, ferromagnetic and antiferrmagnetic.

occurs,[49,50] and this critical temperature is called the Curie temperature, T_C, or the Neel temperature, T_N, for parallel or antiparrallel alignments, respectively.[49] For second order magnetic phase-transitions, the divergence of ξ is the necessary requirement for a transition to long-range magnetic ordering to occur.[1,50]

An ordered ferromagnet refers to the state where the moments are aligned in a parallel fashion. Spontaneous ordering to a ferromagnetic state results in a net magnetization of the sample in the absence of an applied field. On the other hand, in an antiferromagnetically ordered state there is no net magnetization because the antiparallel arrangement of the spin vectors exactly cancels out the individual moments. However, there exist magnetically ordered states where the nearest neighbor spins have an antiparallel alignment but where these states still possess a spontaneous magnetization upon ordering. Two examples are ferrimagentic ordering and canted antiferromagnetic (or weak ferromagnetic) ordering.[49] The arrangement of spin vectors in the above mentioned ordered states are depicted in Figure 1-9. In a ferrimagnet, a net moment exists because each nearest neighbor spin has a different spin moment, and Figure 1-9 depicts the case for $S = 1/2$ and $S = 3/2$ moments. For this specific example, the antiparallel alignment of the $S = 1/2$ and $S = 3/2$ spins results in an incomplete cancellation of the spin vectors and produces an effective spin moment of $S = 1$ oriented in the direction parallel to the $S = 3/2$ moments. In the canted antiferromagnetic state, each spin species has the same spin value, S, but the moments are
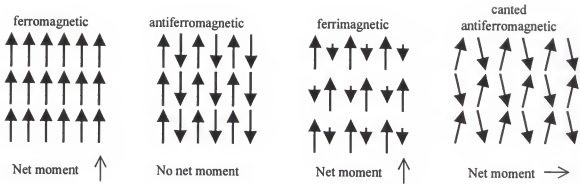
Figure 1-9. Representation of the spin vectors in an ordered ferromagnetic, antiferromagnetic, ferrimagnetic and canted antiferromagnetic states.

tilted slightly from the spin axis. This canted arrangement leads to incomplete cancellation of the spin values and produces a net magnetization with the moment oriented perpendicular to the spin axis. This moment is often very weak, and hence an alternative name for this magnetically ordered state is a 'weak ferromagnet'.

Curie law

The magnetic response of a spin system to an applied magnetic field is given by the simple relation $M = \chi H$, where M is the magnetization, χ is the magentic susceptibility and H is the applied magnetic field.[49] In paramagnetic materials, the magnetic susceptibility as a function of temperature, T, for a given applied magnetic field is well described by the Curie Law (1-1):

$$\chi = C/T \qquad (1\text{-}1)$$

where C is the Curie constant. For materials that have weak interactions between neighboring spins but where ξ does not diverge, the Curie-Weiss law (1-2) is used to describe the magnetic properties.[49]

$$\chi = C/(T - \theta) \qquad (1\text{-}2)$$

The exchange interactions between spins which cause deviations from ideal paramagnetic behavior are referred to as ferromagnetic or antiferromagnetic correlations, and the strength of these interactions are given by θ, the Weiss constant, and as defined here, with positive or negative values signifying ferromagnetic or antiferromagentic interactions, respectively. Typical plots of the static magnetic susceptibility for an ideal paramagnet and for materials with ferro- or antiferromagnetic correlations are shown in Figure 1-10. Even in materials that undergo transitions to long-range order, at temperatures well above the ordering temperaure, that is $T >> T_C$, the Curie-Weiss law can be used to interpret the magnetic data in this high-temperature regime. A detailed account of all known expressions for the temperature dependence of the magnetic susceptibility in systems that order is beyond the scope of this introduction and many have been discussed in detail in books or papers devoted to the subject.[1,49,54,55] However, a more detailed account of the magnetic behavior in dimers, chains and ladders, and 2D sheets is provided in a later section.
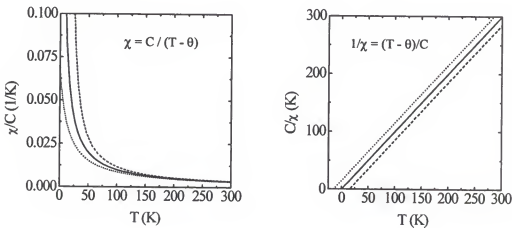
Figure 1-10. The Curie and Curie-Weiss laws. The susceptibility is normalized through division by C (the Curie constant). The solid line in both figures represents the Curie law, whereas the dashed and dotted curves represent the Curie-Weiss law with ferro- and antiferromagnetic correlations, and for these plots, values of $\theta = 15$ and -15 were used, respectively.
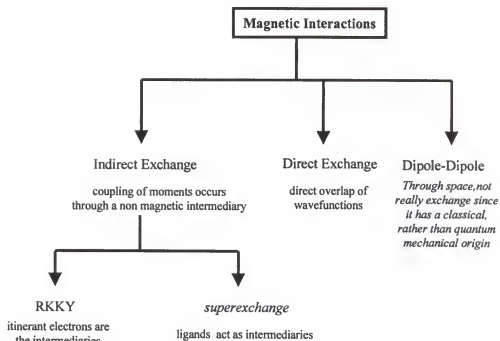
Figure 1-11. Schematic representation of exchange coupling. This figure is modeled after a flow-diagram in ref. 50.

Mechanisms of magnetic exchange

The exchange interactions that exist between unpaired spins in a magnetic system have quantum mechanical origins that are derived from electronic repulsions and the influence of the Pauli exclusion principle.[56] Two main types of exchange couplings can be distinguished. The first is *direct exchange*, which operates through space from the direct overlap of the electronic wavefunctions. On the other hand, *indirect exchange* couples moments by acting through a non-magnetic intermediary, which can be a diamagnetic atom such as a coordinating ligand in transition metal complexes, or itinerant electrons of conducting solids. In the first case, the indirect exchange is often referred to as *superexchange*, while in conducting solids, the coupling is known as *RKKY* exchange (named after those who formulated its theory : Ruderman, Kittel, Kasuya, and Yosida). An additional type of interaction that leads to the stabilization of a

magnetic state, and which is often weaker than the quantum mechanical exchange interactions, is the classical through-space dipolar interaction.[55] Although the dipole-dipole interaction is not strictly speaking a quantum mechanical exchange interaction, it is often useful to represent it in the same mathematical form as an exchange interaction.[57] These exchange mechanisms are summarized graphically in Figure 1-11.

Spin dimensionality and lattice dimensionality

When referring to a magnetic material and the theories that model the magnetic behavior, it is often necessary to discuss the spin dimensionality and lattice dimensionality of the system.[1] The lattice dimensionality, d, refers to the geometrical distribution of the spins in space, with 0D representing clusters, 1D being represented as an infinite linear chain and 2D as an infinite sheet. Similarly, the spin dimensionality, n, ranges from 1-3. Figure 1-12 graphically depicts each of the three cases, where $n = 1$ is referred to as the Ising system (where the spin has only one component, S_z), $n = 2$ is the planar system (where the spin has two components, S_x and S_y) and $n = 3$ is the Heisenberg system (where the spin three components, S_z, S_x and S_y).[1]

Both the lattice and spin dimensionalities play a crucial role in governing whether a transition to long-range magnetic order can occur.[1,55,58,59] The theoretical predictions of when to expect a transition to long-range magnetic order as a function of spin and lattice dimensionality are summarized in Table 1-2. Although the theoretical models predict no long-range order for a 2D Heisenberg system,[60] in fact, there are numerous examples of nominally 2D Heisenberg systems that have been shown to undergo such a transition.[1] The magnetic ordering phenonmenon can be understood by considering that the transition from short-range to long-range order in these systems is accompanied either by a crossover in the effective lattice dimensionality or in the effective spin dimensionality of the system.[1] A lattice dimensionality crossover indicates that, at lower temperatures, the interplane couplings become relevant (similar to kT)

Lattice Dimensionality

$d = 1$ $d = 2$ $d = 3$

Spin Dimensionality

$n = 1$ $n = 2$ $n = 3$
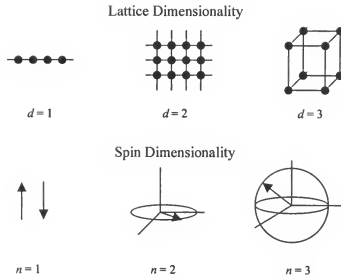
Figure 1-12. Lattice dimensionality and spin dimensionality.

Table 1-2. Effects of Spin and Lattice Dimensionality on Magnetic Ordering

	$d = 1$	$d = 2$	$d = 3$
$n = 1$ Ising	NO LONG RANGE ORDER AT $T = 0$ K		
$n = 2$ Planar		$\xi_{\text{KT}} \rightarrow \infty$ at $T_{\text{K-T}}$	
$n = 3$ Heisenberg			

and ordering occurs as a result of a transition from a 2D to a 3D lattice (typically driven by dipolar couplings[55]). Alternatively, in a truly 2D lattice, a crossover in the effective spin dimensionality can occur if there is some type of spin anisotropy present in the system. Just as the 2D Ising model has an allowed transition, it can be argued on similar grounds that any finite amount of Ising-type anisotropy present in a 2D planar or 2D Heisenberg system could thus lead to a crossover in the effective spin dimensionality.[58]

Spin anisotropy

Since the exchange coupling interactions have quantum mechanical origins, it is most appropriate to represent these interactions by a magnetic spin-Hamiltonian somewhat similar to that used to describe spin-spin couplings in NMR. The Hamiltonian often used for electronic spin-spin interactions has the form

$$\mathcal{H} = -\sum J_{ij} S_i \cdot S_j \tag{1-3}$$

where the sum is taken over all pairwise interactions of spins i and j, with the strength of those interactions given by J, the exchange constant.[49] A negative value of J indicates antiferromagnetic interactions, while a positive value is indicative of ferromagnetic interactions. Often the magnetic exchange interaction is not isotropic in all three spin dimensions and the spin-Hamiltonian is can then be written as:

$$\mathcal{H} = -\sum (J_x S_{ix} \cdot S_{jx} + J_y S_{iy} \cdot S_{jy} + J_z S_{iz} \cdot S_{jz}) \tag{1-4}$$

where $J_x = J_y = J_z$ is the isotropic Heisenberg model. Anisotropy in the exchange interaction can be introduced by allowing for the values of J to differ. For example, $J_x = J_y$, $J_z = 0$ is the XY model, $J_x = J_y = 0$, is the Z model and $J_x \neq J_y \neq J_z$ is the XYZ model.[1,54] Anisotropy in the exchange interaction often has its origins in spin-orbit coupling effects. Table 1-3 summarizes a few spin-Hamiltonian models for different cases of spin anisotropy and spin dimensionality. A subtle point to note is the distinction between the Z model and the Ising model. For the Z model,

$J_x = J_y = 0$, but $S_x \neq 0$ and $S_y \neq 0$. In the case of the classical Ising model, $S_x = S_y = 0$. The point is that in the Z model, although no exchange exists between the x- and y-components of the nearest neighbor spins, the spin dimensionality is still $n = 3$. In contrast, in the Ising model, there is no exchange because the x- and y- components of the spin are not present since $n = 1$.

However, anisotropic properties often arise not from anisotropy in the exchange interactions, but from other sources, such as the presence of a crystalline ligand field or a magnetic dipolar field that couples the moments to a certain direction in the crystal.[55] In this case, the anisotropy is represented by additional terms in the Hamiltonian. These additional single-ion anisotropy terms in the spin-Hamiltonian, are typically of the form, $-D\Sigma(S_{iz})^2$ and $E\Sigma[(S_{ix})^2 - (S_{iy})^2]$. In this manner, another types of anisotropic Heisenberg models can be obtained, and for example, for large values of the anisotropy, the predicted magnetic behavior can resemble those of the Ising and Z models.[55]

However, the assignment of the origins of the anisotropy in the magnetic interactions is not always a simple task and the interpretations can sometimes be quite confusing. The following is an excerpt from a discussion of this point:[55]

Table 1-3. Summary of Some Spin Hamiltonian Models for Different Cases of Spin Anisotropy and Spin Dimensionality.[1,54]

Spin-Dimensionality	Interaction	Model
$n = 3$ $S_x^2 + S_y^2 + S_z^2 = S(S+1)$	$J_x = J_y = J_z$ $J_x = J_y \ ; J_z = 0$ $J_x = J_y = 0; J_z$	Heisenberg XY Z
$n = 2$ $S_x^2 + S_y^2 = S(S+1)$	$J_x = J_y$ $J_x = 0; J_y$	Planar Planar Ising
$n = 1$ $S_z^2 = S(S+1)$	J_z	Ising

In fact, in comparing experiments on Ising-like substances with theory it has proven in most cases to be unimportant whether the anisotropic properties have been realized by anisotropy in the exchange or by single-ion anisotropy (note that in the latter case one can approximate closely with the Ising model only with $S = \frac{1}{2}$). Nevertheless, one should bear in mind that there is a fundamental difference between the two methods of approach, leading in some situations to contrasting results.

Additional sources of anisotropy include biquadratic exchange interactions, electric multipole interactions, virtual phonon exchange and the superexchange mechanism itself. However, when dealing with fairly ionic compounds, anisotropy in the exchange other than that derived simply from single-ion terms has been observed for only a few compounds.[55]

Magnetic Interactions in Low Dimensional Materials

Structurally, the layered metal phosphonates can be categorized as low dimensional materials. Additionally, this structural anisotropy can introduce interesting low dimensional magnetic phenomena for those compounds possessing paramagnetic metal ions. For instance, the magnetic behavior of some copper and vanadyl phosphonates can be well characterized by dimeric interactions between pairs of metal ions.[19,48] On the other hand, the magnetic properties of $(VO)_2P_2O_7$ have been characterized as ladder-like in nature or as alternating 1D Heisenberg chains.[61-64] Further examples of the metal phosphonates exhibiting low dimensional magnetic properties include the divalent metal phosphonates of formula $M^{II}(O_3PR)H_2O$ with $M^{II} = Mn^{2+}$, Ni^{2+}, Fe^{2+}, Co^{2+} and Cr^{2+} which have been shown to behave as 2D Heisenberg canted anitferromagnets.[22,31,65] In the following sections, the magnetic properties of each of these three cases are discussed in more detail. One important point to remember is that although all of these materials are structurally layered ($d = 2$), it is the finer details of how the metal centers are connected together within the in-plane structure that dictate the magnetic behavior. This principle forms the foundation of magnetostructural investigations, which aim to understand how structure and physical properties are related.
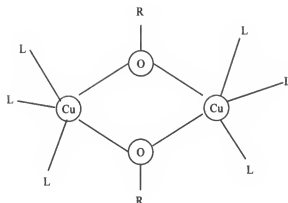
Figure 1-13. A dimeric unit of copper (II) ions connected by two oxo-bridges.

Dimers, ladders and chains

Dimers. The exchange interaction that exists between a dimeric pair of atoms represents one of the simplest types of superexchange that can occur between two metal centers that are bridged by coordinating ligands.[49,66-69] Figure 1-13 schematically depicts the structure of a dimeric copper unit connected by two oxo-bridges. Since the lattice dimensionality of dimeric interactions is $d = 0$, the proceeding discussion does not pertain to a state of long-range order, but instead describes the short range interactions that exist between pairs of metal centers. Long-range order may occur in such materials only if there is a crossover in the lattice dimensionality. The spin Hamiltonian that describes the exchange between dimeric pairs is given by:[49]

$$\mathcal{H} = -JS_1 \bullet S_2 \tag{1-5}$$

where J is the exchange constant and the summation is limited to only exchange between the two atoms (S_1 and S_2) in the dimeric molecule. Bleaney and Bowers first described the magnetic behavior of hydrated copper acetate with a model that accounted for strong antiferromagnetic coupling between the pairs of copper atoms. Because of their early application of this model, the expression that describes the temperature dependence of the magnetic susceptibility for two $S = \frac{1}{2}$ ions interacting as a dimeric pair, is readily referred to as the Bleaney-Bowers expression. This expression is given by:

$$\chi = \frac{2Ng^2\mu_B^2}{3kT}\left[1+1/3\exp\left(-\frac{J}{kT}\right)\right]^{-1}(1-f) + f\frac{Ng^2\mu_B^2}{2kT} \qquad (1-6)$$

where χ is the magnetic susceptibility, J is the superexchange constant indicative of the singlet-triplet energy gap, with a negative value of J indicating antiferromagnetic coupling, whereas a positive value is indicative of ferromagnetic exchange, f is the mole fraction that preceeds the Curie-term and accounts for the effects of uncoupled paramagnetic impurities, and where N, g, μ_B, k and T have their usual meanings. Figure 1-14 shows the temperature dependant magnetic susceptibility for the Bleaney-Bowers expression for an arbitrary system with $g = 2.2$ and $J/k = -30$ K for a pair of $S = 1/2$ copper ions with a 2% impurity.

As stated earlier, the magnetic behavior of the copper and vanadyl organophosphonates can be well described by dimeric interactions between pairs of Cu^{2+} ($S = \frac{1}{2}$) and V^{4+} ($S = \frac{1}{2}$) ions, respectively. Figure 1-15 shows the magnetic susceptibility data for some copper alklyphosphonate powders where in each case the solid line is a fit of the data using the Bleaney-Bowers equation. Although the structures of these phosphonates are layered, the major super-
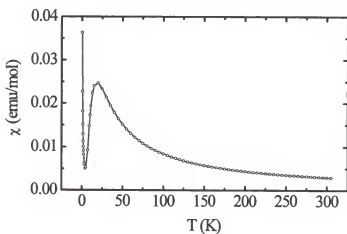
Figure 1-14. Plot of the temperature dependence of the magnetic susceptibility for the Bleaney-Bowers expression with $g = 2.2$, $J/k = -30$ K and $f = 0.02$.
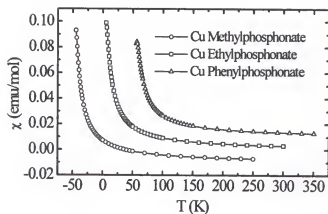
Figure 1-15. Magnetic susceptibility data of copper alkylphosphonates. The lines are fits of the data using the Bleaney-Bowers expression. The susceptibility and temperature scales are shown for copper ethylphosphonate, all others are offset by ± 50 K / ± 0.01 emu/mol. The data are taken from ref. 44 with J/k values of -7.56, -6.9, and -9.38 for copper ethyl-, methyl-, and phenylphosphonate, respectively.
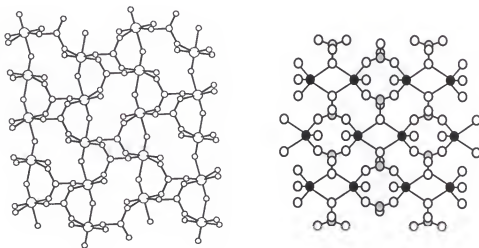
Figure 1-16. In-plane bonding arrangement of **(left)** type A and **(right)** type B vanadyl phosphonate lattices. The crystallographic data are taken from ref. 46 and 47 respectively.

exchange pathways exist only between pairs of metal centers.[19] Figure 1-16 shows the in-plane bonding arrangement of two different vanadyl phosphonate lattice-types, which are referred to as type A and B.[70] In both cases, since the magnetic (unpaired) electron resides in the $d_{x^2-y^2}$ orbital,[71] the magnetic exchange does not occur between V=O-V linkages. Figure 1-17 shows the temperature dependent static susceptibility for each of these lattice types.[47,48] It is clear that the magnetic exchange differs for the two lattice types and this difference can be understood by comparing the in-plane metal phosphonate lattice structure for each class. For the type A lattice, the exchange is mediated by V-O-P-O-V linkages, while in the type B lattice, the V-O-V linkages are the magnetic exchange pathways. Since the V-O-V pathways are shorter in distance, it is reasonable that magnetic exchange in the organophosphonates with type B lattices is larger than that in the type A materials.[71]

Additionally, the magnetic properties of a series of para-substituted vanadyl phenylphosphonates have been studied.[48] Each of these materials contains an isostructural type B metal phosphonate lattice, and Figure 1-18 shows the magnetic susceptibility data for protonated, fluoro, and nitro para-substituted vanadyl phenylphosphonates. The data show that the electronic perturbation of the substituent group affects the magnetic interaction in a well-defined manner. Specifically, the more electron withdrawing the substituent group, the weaker the magnetic exchange. These results are similar to those observed for various substituent and ligand effects in di-μ-oxo bridged copper systems which can be understood by considering how the electronic perturbations affect the energies of the metal d and oxygen p orbitals involved in the magnetic exchange pathways.[66]

Indeed, the dimeric systems in which the magnetic behavior has been most extensively studied are the of di-μ-oxo bridged copper (II) complexes.[72] The work of Hatfield and Hodgson,[68,73] Gatteschi,[69] Willett,[74] Hoffman,[66] and Kahn,[75,76] which includes experimental
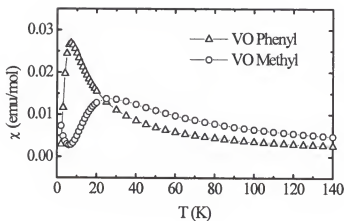
Figure 1-17. Magnetic susceptibility data for vanadyl phenylphosphonate (type A lattice) and vanadyl methylphosphonate (type B lattice). The solid lines are fits of the data using the Bleaney-Bowers expression. The data are taken from ref. 48 and 47, with $g = 1.98$ for both samples and $J/k = -11$ K and -44 K for vanadyl phenyl- and methylphosphonate, respectively.
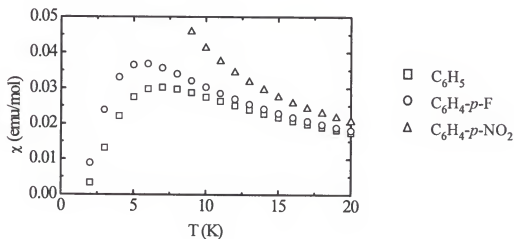
Figure 1-18. Magnetic susceptibility data for a series of para-substituted vanadyl phenylphosphonates. For each sample $g = 1.98$ and $J/k = -11$ K, -9 K and 0 K, for the protonated, fluoro and nitro p-phenyl substituents, respectively. The data are taken from ref. 48.

synthesis, measurement of the magnetic properties and theoretical formulation of the magnetic interactions of dimeric systems, has provided a fundamental understanding of how the structure of the dimeric unit, the μ-oxo substituent, and the axially coordinating ligands are correlated with the magnetic exchange properties. These experimental and theoretical endeavors have laid the foundation for numerous other chemists and physicists to pursue efforts to design and fabricate novel magnetic materials with tailored magnetic properties.

Ladders and chains. As stated previously, a low-dimensional structure refers to an arrangement of atoms or molecules that is anisotropic in space where the resultant structure appears to exist in chains or sheets. Magnetic interactions that exist between metal centers arranged as sheets, chains and clusters correspond to a lattice dimensionality of 2, 1, and 0 respectively. Somewhere between the dimensions of 1 and 2 (the chains and sheets) exist the magnetic ladders, and Figure 1-19 depicts an idealized structure of a ladder material. Magnetic interactions of ladder-like structures are of interest because they provide an interesting step from the relatively well understood one-dimensional magnetic behavior towards two-dimensional systems, or in other words, they provide a way to understand the dimensionality crossover from one to two dimensions.[77] In addition, these materials show interesting spin behavior such as spin gaps, and in doped systems, phenomena such as hole pairing and finite superfluid density have been observed.[77]

The magnetic interactions that exist in ladders are characterized by two superexchange parameters, J and J' which correspond to the exchange along the legs and rungs of the ladders, respectively (Figure 1-20). The magnetic properties of such systems are ladder-like only when $J \approx J'$. For the extreme cases of $J \gg J'$ and conversely $J' \gg J$, the magnetic properties will resemble those of 1-D chains and dimers, respectively.
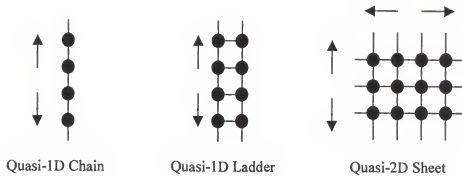
Figure 1-19. Idealized structural representation of an infinite 1D chain, a quasi-1D ladder and an infinite 2D sheet.
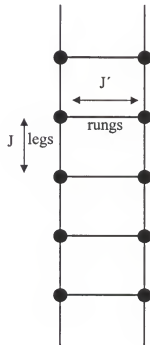
Figure 1-20. Magnetic exchange interactions in a spin ladder system.
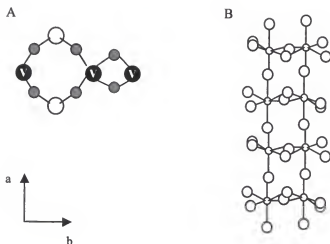
Figure 1-21. Idealized structures of (A) the 1D alternating V-O-P-O-V and V-O-V units in $(VO)_2P_2O_7$ [Key: oxygen, gray circles; phosphorus, open circles; vanadium, black circles] and (B) the ladder-like structure of $(VO)_2P_2O_7$ [Key: vanadium, smaller circles; oxygen, larger circles].

Examples of known spin-ladder materials include $SrCu_2O_3$ and $Cu_2(C_5H_{12}N_2)_2Cl_4$.[77] The compound vanadyl pyrophosphate, $(VO)_2P_2O_7$, is often referred to as an antiferromagnetic Heisenberg spin ladder system.[61,71] However, recent inelastic neutron scattering results[62,63] show that the magnetic exchange in this material does not behave as a spin-ladder, but is rather best described as an alternating spin chain.

The confusion as to the type of magnetic exchange that occurs in this material originates from primarily two considerations. Firstly, the in-plane structure of $(VO)_2P_2O_7$ has a connectivity pathway that closely resembles the structure of a ladder where the legs are formed from V=O-V linkages, and where two V-O-V pathways form the rungs of the ladder.[61] Alternatively, a second magnetic pathway can be discerned. This pathway can be described as a 1-D chain of alternating V-O-P-O-V and V-O-V units.[64,71] These two types of magnetic pathways are depicted in Figure 1-21. Although it was originally assumed that the V-O-P-O-V pathways would mediate little magnetic exchange,[71] studies on vanadyl akly- and phenylphosphonates[48] have shown that magnetic exchange through these pathways is possible and conversely, it is the V=O-V pathways that are inefficient at mediating the exchange interactions. Figure 1-22 depicts the exchange
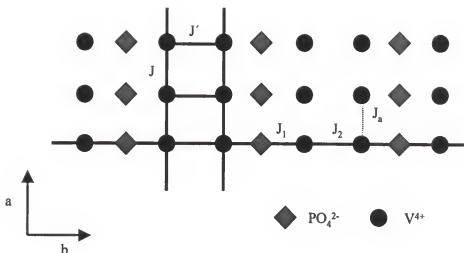
Figure 1-22. Cartoon representation of the in-plane exchange pathways for the spin ladder and alternating 1D chain model of $(VO)_2P_2O_7$. In the spin-ladder model, J and J' represent the exchange along the leg and rung directions, respectively. In the alternating 1D chain model, J_1 and J_2 represent the exchange constants along the chain. The neighboring spins in adjacent chains are coupled weakly by J_a. This figure is modeled after a figure in ref. 63.

pathways for the spin ladder model and for the alternating chain model.[63] Secondly, it is known that the temperature dependent susceptibility of a spin ladder and an alternating linear chain are quite similar,[62-64] so static magnetometry measurements cannot easily distinguish between the two models. This last point prompted a microscopic investigation of the magnetic interactions in $(VO)_2P_2O_7$ by inelastic neutron scattering techniques which show that the exchange occurs via the alternating V-O-P-O-V / V-O-V units of 1D linear chains.[63]

2D infinite sheets

The magnetic properties of organophosphonates of divalent metal ions of formula $M^{II}(O_3PR)H_2O$ (M^{II} =Mn, Ni, Co, Fe, Cr) have been studied by the groups of Day[22,23,52,53] and Bujoli,[65] and in each case, they are shown to be well characterized by the 2D quadratic layer Heisenberg antiferromagnet.[78] Although there is no analytical solution for the temperature dependence of the magnetic susceptibility of a 2D system, there is a numerical expression that

describes the magnetic exchange for metal ions arranged in a layer at the vertices of a square. This expression is given by:

$$\frac{N g^2 \mu_B^2}{J\chi} = 3\theta + \sum \left(C_n / \theta^{n-1} \right) \tag{1-7}$$

where $\theta = kT/JS(S+1)$, g is the Lande factor, N is the number of spins, μ_B is the Bohr magneton, J is the superexchange constant and C_n are coefficients. The values of the coefficients for various values of S have been calculated up to $n = 6$ by Lines and co-workers.[78] Figure 1-23 shows the magnetic susceptibility data for manganese hexylphosphonate as a function of temperature, with the dotted line as a fit using expression 1-7. The manganese phosphonates are known to order to a canted antiferromagnetic state near 15 K.[22] Although theory predicts that 2D Heisenberg materials cannot undergo a transition to long-range magnetic order,[1] this transition is allowed when a finite amount of Ising-type anisotropy is present.[58] A more detailed discussion of the magnetic properties of a series of manganese phosphonates is presented in Chapters 3 and 4.
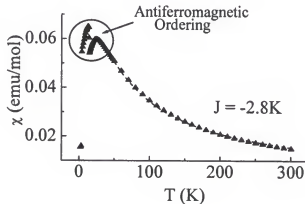
Figure 1-23. Magnetic susceptibility data for manganese hexylphosphonate, with the dotted line representing a fit of the data with the 2D quadratic layer Heisenberg antiferromagnet model.

Mixed Organic/Inorganic Thin Films

Materials that possess both organic and inorganic components are of interest from fundamental and practical points of view.   Fundamentally, there exists the possibility of synthetically producing materials that contain a composite of physical properties, each derived from the separate organic and inorganic components, that would not be found together in one single type of material.[4]   Moreover, the desire to fabricate materials that have new synergistic properties that arise from the interplay of the composite physical properties and could not exist without each of the separate components is another driving force for their investigation. From the practical point of view, materials that possess composite properties such as magnetism and non-linear optics, or both magnetic and transport properties are desirable for their use as devices such as molecular based switches and sensors.[79]

Metal phosphonates, with their separate organic and inorganic components, offer a route for the formation of such materials. Although there have been many studies of intercalating organic molecules with potential non-linear optical[80] or conducting properties[81,82] into polycrystalline zirconium phosphonate solids, thin film analogs offer alternatives to the powders to achieve these purposes.[11] The following two sections discuss metal phosphonate thin films derived from "self-assembly-like" routines and Langmuir-Blodgett depositions.

Spontaneously Absorbed Metal Phosphonate Films

The self-assembly of monolayers refers to the spontaneous adsorption of molecules onto the surface of a solid support when this substrate is submersed into a solution of the molecules to be assembled (Figure 1-24).[83] There are many types of molecules that spontaneously adsorb onto surfaces.   These include organosilanes on hydroxylated surfaces such as SiO_2 or Al_2O_3;[84,85] alkanethiols on gold, silver and copper;[79,86-88] carboxylic acids on Al_2O_3 and silver;[79] and organo-
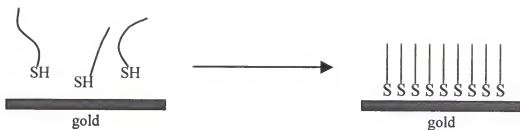
Figure 1-24. Spontaneous adsorption of an alkylthiol to a gold substrate.
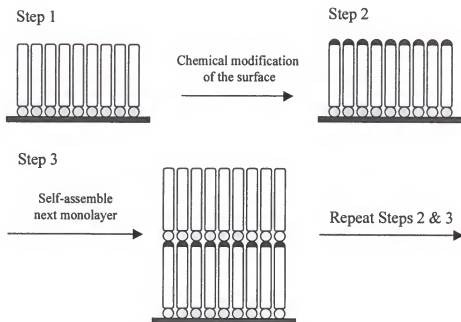
Figure 1-25. Preparation of spontaneously adsorbed multilayer films. (Step 1) The spontaneous adsorption of the first monolayer to the solid support. (Step 2) Chemical modification of the terminus of the SA monolayer, which produces a new surface for further monolayers to adsorb upon. (Step 3) SA of the next monolayer. Multilayer assemblies are built by repeating Steps 2 and 3.

amines on YBCO thin films and particles,[89-93] to name a few. In addition, organophosphonates have also been shown to spontaneously adsorb onto zirconated-silicon oxide, zirconium oxide, and titanium oxide particles.[94,95]

The stabilizing force in the SA process is the exothermic interaction of the head functional group with the surface.[79] Although many studies of SA films have centered only on the formation of monolayers, methods have been developed to prepare multilayer assemblies via SA routes. In general, these methods proceed by the assembly of monolayers with functionalized tail groups (Figure 1-25), where after the monolayer is adsorbed onto the surface, chemical modification at the tail end of the molecule produces a new surface for further chemisorption steps. Efforts for developing strategies aimed at preparing multilayer assemblies of organosilanes have been pioneered by Sagiv and co-workers,[96] whereas Mallouk and others have developed methods for preparing multilayer metal phosphonate films by SA techniques.[12,94,97-100]

The procedure for preparing metal phosphonate thin films is outlined in Figure 1-26. A substrate such as gold or silicon is functionalized by the appropriate long-chain molecule (an organothiol or organosilane, respectively) that has a tail group capable of chemical reaction to PO_3H_2 group or simply containing a PO_3H_2 group. This first step produces a film with a phosphonic acid terminated surface. This surface is then exposed to a metal ion solution, where the metal ions bind to the phosphonate end of the surface. It is the strong affinity of the phosphonate groups for binding metal ions that drives this process. For the zirconium assembled films, this step is carried out in aqueous media,[98] but for the divalent metal phosphonate films, since the metal lattice is soluble at low pH, this adsorption step is performed in aqueous alcoholic mixtures.[100] Multilayer films are grown by alternately adsorbing α,ω-diphophonic acid molecules and metal ions from solution. Films of alkylphosphonates have been deposited with
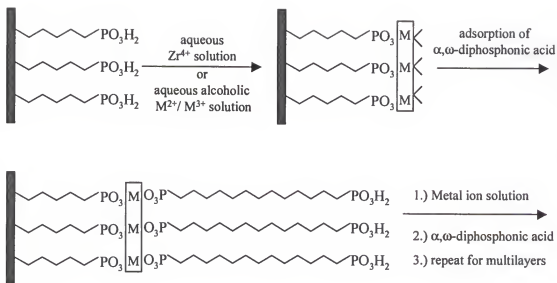
Figure 1-26. Deposition scheme for the formation of multilayer SA films of alkylphosphonates.

tetravalent, trivalent and divalent metal ions, and multilayers have been shown to be relatively pinhole free and act as good insulators.[101]

A variety of multilayer metal phosphonate films have been formed from functionalized organophosphonic acid molecules with the aim of producing non-linear optical properties.[102,103] To ensure the orientation of the molecules in the film, the adsorbing molecules are prepared with different functional groups at each end, such as a phosphonic acid group at the adsorbing end and a hydroxy terminus at the other end. After attachment of the phosphonic acid end of the molecules to the surface, the hydroxy terminated surface is chemically modified to a phosphonic acid surface for further film growth. The chemical asymmetry of the molecules ensures that they adsorb in only one direction, which retains the polar orientation of the molecules necessary for non-linear optical properties. Spontaneously adsorbed multilayer metal phosphonate films have been prepared in this way for their potential optical,[26,27] nonlinear optical[102,103] and electronic properties.[104,105]

Metal Phosphonate Langmuir-Blodgett Films

In addition to the SA metal phosphonate thin film architectures, it has been demonstrated that Langmuir-Blodgett (LB) and mixed LB/SA routes can be used to prepare multilayer metal phosphonate assemblies.[5,7,8,10,106] The LB method is an elegant way of organizing molecules on the water surface with the subsequent transfer of the assembly to a solid support.[83,107] Typically, amphiphilic molecules are spread onto the water surface from solution in a volatile solvent. As the solvent evaporates, the polar end of the molecule submerses into the aqueous subphase and the hydrophobic tail extends outwards from the surface. At this stage, the molecules are largely separated from one another and their thermodynamic behavior can be referred to as a quasi-2D gaseous state.[83] Usually the Teflon trough apparatus contains one or two movable barriers that mechanically compress the molecules into an ordered assembly. The organization of the molecules on the water surface is monitored by a change in the surface tension, which is measured by a platinum Wilhelmy plate suspended into the water surface from a microbalance. Figure 1-27 schematically shows the compression of a monolayer film from the quasi-2D gaseous state to the quasi-2D solid state. The trace of the surface pressure as a function of compression is referred to as the pressure versus area (π/A) compression isotherm (Figure 1-28).

Once the molecules are organized on the water surface, the assembly can be transferred onto a solid support by either pushing or pulling the substrate through the floating monolayer (Figure 1-29). As the substrate passes through the film, the surface pressure is maintained at a constant value in order to maintain the closed-packed organization of the film. As the film is transferred to the substrate, the barriers move in order to maintain the pressure, and a ratio of the area that the barriers transverse to the area of the substrate provides a transfer ratio for each deposition.
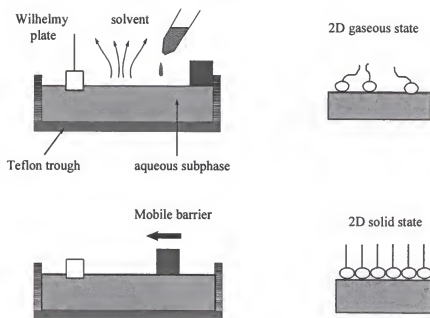
Figure 1-27. Formation of a Langmuir monolayer on the water surface.
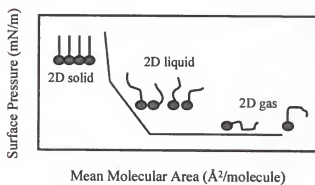
Figure 1-28. Idealized pressure versus area (π/A) compression isotherm.
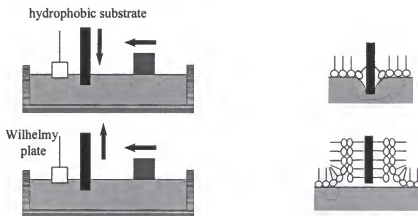
Figure 1-29. Transfer of a Langmuir-Blodgett bilayer onto a hydrophobic substrate.

Figure 1-30 depicts three different ways in which amphiphilic molecules can be arranged in deposited LB films.[83] These are referred to as X, Y, and Z type films. The Y-type film is often referred to as a head-to-head/tail-to-tail type bilayer. The structural similarity between the alternating polar and non-polar layers of the Y-type LB film and the alternating organic/inorganic layered structural motif of metal phosphonate solids,[12] prompted an idea to incorporate the metalphosphonate continuous inorganic lattice architecture into Y-type LB films of organophosphonic acids (Figure 1-31).

Previous work of others demonstrated that it is possible to form metal octadecylphosphonate LB films that each contained a different divalent metal phosphonate lattice structure.[7,9,10,106] These films were shown to be well organized and to possess a crystalline continuous 2D inorganic lattice analogous to that of the corresponding divalent metal phosphonate solid-state material. Incorporation of the inorganic lattice into the LB film provides not only structural stability and organization, but also allows a way to introduce physical phenomenon such as magnetism. In fact, the manganese octadecylphosphonate LB film was the first example of a continuous lattice LB film to undergo a transition to long-range magnetic order with spontaneous magnetization.[10] Earlier work has also demonstrated that a mixed three-step LB/SA approach can be used to form zirconium organophosphonate LB films.[5,6,108-110]
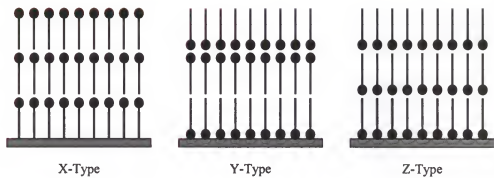
Figure 1-30. Three types of transferred LB films. The balls represent the polar head-groups, and the sticks represent the non-polar tails.
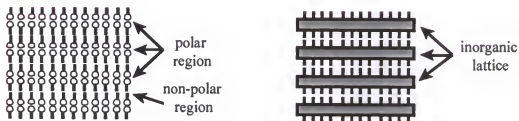
Figure 1-31. Incorporation of the metal phosphonate lattice into the polar region of Y-type LB films.

Scope of the Dissertation

Part of the work presented in this dissertation is aimed at understanding the fundamental concepts of (1) how to incoporate different metal phosphonate 2D continuous lattice structures into the polar regions of organophosphonate LB films, and (2) how to incorporate larger functionalized organic groups into the non-polar regions of these organophosphonate LB films while retaining the 2D metal phosphonate lattice structure. These topics are discussed in chapters 2 and 3, respectively. Chapter 2 demonstrates that it is possible to extend this LB technique to incorporate the lattice structure of the lanthanide phosphonates into the octadecylphosphonate LB films, and a generalization of how to form continuous lattice metal phosphonate LB films is presented. Chapter 3 contains the results of studies of phenoxy substituted organophosphonate LB films containing the crystalline Cd and Mn phosphonate lattices, including a discussion of the magnetic properties of the Mn-P4 LB film. Structural studies of phenoxysubstituted organophosphonate LB films with the 2D amorphous zirconium phosphonate lattice are also reported in this chapter. Issues such as the effects of the position of the phenoxy substituent on film stability, transfer and formation of the inorganic lattice structures are discussed.

The second half of the dissertation is concerned with magnetic resonance studies of metal phosphonate solids and LB films. Chapter 4 presents a magnetostructural study of a series of manganese organophosphonates and manganese phosphate by antiferromagnetic resonance (AFMR) and static magnetometry measurements. The effects of the organic substituents on the magnetic exchange and anisotropy energies, as well as the effects on the canting moments, are discussed. Chapter 5 reports the results of the first ^{31}P nuclear magnetic resonance (NMR) studies of organophosphonic acid LB films. These NMR studies demonstrate the feasibility of NMR as a technique for studying the structure and organization of layer-by-layer thin film constructs containing from tens to hundreds of layers. Chapter 6 contains the results of a ^{2}H quadrupole echo NMR study of phenyl ring dynamics in layered metal phosphonate powdered

materials. The results show that the phenyl rings flip by 180° around their C_{2v} axis, and the activation energies for two metal phenylphosphonates are reported.

LANGMUIR-BLODGETT FILMS BASED ON KNOWN LAYERED SOLIDS :
LANTHANIDE (III) OCTADECYLPHOSPHONATE LB FILMS

Introduction

The Langmuir-Blodgett (LB) technique is a means of transferring an organized monolayer of molecules from an air-water interface onto a solid support,[79,83,107] and this procedure offers a degree of control over the design and fabrication of thin film monolayer and multilayer assemblies. It has recently been demonstrated[5,7,8,10,106,109] that the LB methodology can be used to prepare organic/inorganic films modeled after layered solid-state materials. Specifically, metal octadecylphosphonate (ODP) LB films[10,111] have been formed which contain the inorganic continuous lattice structure of solid-state divalent metal phosphonates with formulas $M^{II}(O_3PR)H_2O$ (where $M^{II} = Mn^{2+}$, Cd^{2+}, Mg^{2+}, Co^{2+})[16,32] and $M^{II}(HO_3PR)_2$ (where $M^{II} = Ca^{2+}$ and Ba^{2+}).[29,36] Incorporation of an inorganic continuous lattice structure into LB films adds increased stability to the films through the inorganic lattice energy and offers a route to introduce physical phenomena such as long-range magnetic order.[10]

In addition to the divalent metal salts, there are other known layered metal phosphonates, including the trivalent lanthanide phosphonates[29,37] $Ln^{III}H(O_3PR)_2$. The structure of lanthanum phenylphosphonate is shown in Figure 2-1. The Ln^{III} phosphonates form with a layered structural motif where the metal ions are arranged in a sheet and are coordinated from above and below by the phosphonate oxygens, with the organic substituents projecting into the regions between the planes of metal ions. This architecture is similar to that of the divalent metal phosphonates.
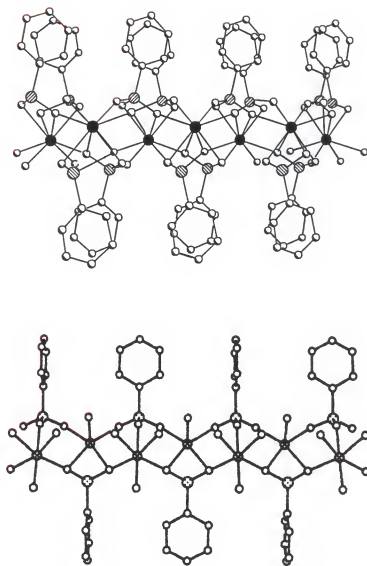
Figure 2-1. **(top)** A single layer of lanthanum phenylphosphonate, LaH(O$_3$PC$_6$H$_5$)$_2$, viewed parallel to the lanthanum ion (cross-hatched) plane. Crystallographic data are taken from ref. 37. **(bottom)** A single layer of the solid-state manganese phenylphosphonate, Mn(O$_3$PC$_6$H$_5$)H$_2$O, also viewed parallel to the metal ion plane. Crystallographic data are taken from ref. 16.

However, the metal ion coordination geometry of the trivalent lanthanide materials differs from that of the divalent metal phosphonates resulting in different metal-oxygen-phosphorus bonding arrangements in these materials. Changes in the bonding geometry of the inorganic plane has subsequent effects on the packing of the organic groups which can clearly be seen by comparing the packing of the phenyl rings in the lanthanum and manganese phenylphosphonate structures (Figure 2-1).

The work presented here shows that it is possible to extend the LB technique to incorporate the continuous lattice structure of the trivalent lanthanide metal phosphonates into LB films of octadecylphosphonic acid (ODPA). $LnH(O_3PC_{18}H_{37})_2$ LB films (where $Ln = La^{3+}$, Ce^{3+}, Sm^{3+}, and Gd^{3+}) have been characterized by X-ray diffraction (XRD), X-ray photoelectron spectroscopy (XPS) and Fourier transform infrared (FTIR) spectroscopy and are shown to have structures analogous to the solid state $LnH(O_3PR)_2$ (where $R = C_4H_9$ and C_6H_5) materials, providing further examples of continuous solid LB films. The deposition conditions are compared to those used to prepare divalent metal phosphonate LB films, and some general requirements for forming continuous lattice metal phosphonate LB films are discussed.

Experimental Section

Materials Used

All chemicals were purchased and used as supplied. Octadecylphosphonic acid (ODPA, $C_{18}H_{37}PO_3H_2$, 98%) was purchased from Ted Pella (Ward Hill, NJ). Butylphosphonic acid ($C_4H_9PO_3H_2$, 99%) was purchased from Fluka (Buchs, Switzerland). Phenylphosphonic acid ($C_6H_5PO_3H_2$, 99%), octadecyltrichlorosilane (OTS, $C_{18}H_{37}SiCl_3$, 95%), $CeCl_3 \cdot 7H_2O$ (99%), $SmCl_3 \cdot 6H_2O$ (99+%), and $GdCl_3 \cdot 6H_2O$ (99.9%) were purchased from Aldrich (Milwaukee, WI). $La(NO_3)_3 \cdot 6H_2O$ (99%) was purchased from Alfa Aesar (Ward Hill, MA). A Barnstead

NANOpure purification system produced water with an average resistivity of 18 MΩ cm for all experiments. The powdered solid-state materials were prepared by standard literature procedures for growth of metal organophosphonates.[29,37]

Substrate Preparation

Single crystal (1 0 0) silicon wafers, purchased from Semiconductor Processing Company (Boston, MA), were used as deposition substrates for XPS samples. Samples for X-ray diffraction studies were deposited onto glass petrograph slides purchased from Beuhler, Ltd. (Lake Bluff, IL). Silicon and glass substrates were cleaned using the RCA cleaning procedure[112] and dried under N_2. Germanium attenuated-total-reflectance (ATR) parallelograms (45°, 50 mm x 10 mm x 3 mm), purchased from Wilmad Glass (Buena, NJ), were used as substrates for ATR-FTIR experiments. Germanium ATR crystals were cleaned by an oxygen plasma etch and washed with chloroform in a Soxhlet extractor before use. Substrates were made hydrophobic by deposition of a monolayer of OTS.[84,96]

Instrumentation Used

The LB experiments were performed using KSV 2000 and 3000 Instruments (Stratford, CT) modified to operate with hydrophobic double barriers on home-made Teflon troughs with surface areas of 371 cm^2 (9.4 cm x 39.4 cm) and 960 cm^2 (12.8 cm x 75 cm), respectively. The surface pressure was measured with a platinum Wilhelmy plate suspended from a KSV microbalance. Infrared spectra were recorded with a Mattson Instruments (Madison, WI) Research Series-1 Fourier transform infrared spectrometer using a deuterated triglyceride sulfide detector. A Harrick (Ossining, NY) TMP stage was used for ATR experiments. ATR-FTIR spectra consist of 1000 scans at 4 cm^{-1} resolution. X-ray photoelectron spectra were obtained using a Perkin-Elmer PHI 5000 series spectrometer. All spectra were obtained using the MgKα

line source at 1253.6 eV. Multiplex scans, 65 scans over each area, were acquired over a 30-50 eV range with a pass energy of 35.75 eV. X-ray diffraction was performed with a Phillips APD 3720 X-ray powder difractometer with the CuKα line, $\lambda= 1.54$ Å, as the source.

Results and Discussion

Langmuir Monolayers

The behavior of ODPA at the air-water interface was studied as a function of pH for 0.5 mM Ln^{III} (Ln = La^{3+}, Ce^{3+}, Sm^{3+}, and Gd^{3+}) subphases, and representative pressure vs. area (π/A) isotherms are presented in Figure 2-2. The effect of subphase pH on the association of metal ions with the phosphonate head groups can be inferred from the shapes of these isotherms. For each metal ion system studied, at low pH, the compression isotherms contain three distinct regions corresponding to a two-dimensional gas analogous phase, a liquid-expanded (LE) phase and a liquid condensed (LC) phase. For example, in Figure 2-2, these three regions are clearly observed for the ODPA isotherms on each metal ion-containing subphase at pH < 3.0. These isotherms are similar to that observed for ODPA in the absence of metal ions (at a pH range of 2-3), and indicate that there are no interactions between the metal ions and the monolayer at low pH. As the pH is increased, the transition between the LE and LC phases becomes less pronounced, the slope of the compression curve becomes less steep, and film collapse occurs at a lower pressure. These observations indicate that the metal ions are beginning to associate with the phosphonate head groups.[113-115] As the pH is increased further, the mean molecular area where the surface pressure begins to rise increases, the slope of the compression curve becomes even more shallow, and the collapse pressure continues to decrease, characteristic of the formation of rigid islands at the air/water interface caused by cross-linking of the organophosphonate molecules by the tightly bound metal ions.[108] An increase in the film rigidity results in an apparent area at collapse of less than 20 Å^2/molecule. This unreasonably low area is
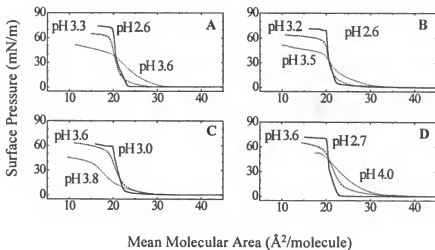
Figure 2-2. Pressure vs. area isotherms for ODPA on 0.5 mM Ln^{3+} subphases at the indicated pH values where Ln = (A) La^{3+}, (B) Ce^{3+}, (C) Sm^{3+}, and (D) Gd^{3+}.

either a result of a breakdown of the Wilhelmy plate method for measuring the surface pressure of a rigid monolayer, or is due to the monolayer folding over to form bulk metal phosphonates on the water surface. The subphase pH at which the transition between the LE and LC phases becomes hard to discern, is defined here as the "characteristic pH" to represent the metal ion's affinity for the phosphonate monolayer. The values of the "characteristic pH" are reported in Table 2-1 for 0.5 mM subphases and range from pH 2.7 to pH 3.4 following the trend of La^{3+} < Ce^{3+} < Sm^{3+} < Gd^{3+}.

Film Deposition

Langmuir-Blodgett (LB) films of the Ln^{III} octadecylphosphonates are formed by Y-type deposition onto hydrophobic surfaces (Figure 5-3). Typically, 70 μL of a 0.3 mg/ml solution of ODPA in HPLC grade chloroform is spread onto a 0.5 mM aqueous subphase of the desired metal ion. For each metal ion, the subphase is adjusted to an "optimum pH" for film deposition, (Table 2-1). The Ln^{III} ODP LB films are transferred onto a solid support by compressing the

Table 2-1. Characterisitic[a] and Optimum[b] Subphase pH Values for Ln[III] ODP LB Films.

Metal ODP-LB Film[c]	Characteristic pH (±0.05)	Optimum pH (±0.05)
LaH(O$_3$PC$_{18}$H$_{37}$)$_2$	2.70	2.50
CeH(O$_3$PC$_{18}$H$_{37}$)$_2$	2.80	2.60
SmH(O$_3$PC$_{18}$H$_{37}$)$_2$	3.30	3.10
GdH(O$_3$PC$_{18}$H$_{37}$)$_2$	3.40	3.20

[a] The characteristic pH is defined as the pH at which the compression isotherm of ODPA on the 0.5 mM Ln[III] subphases loses the sharp phase transitions that are observed on a pure water subphase at pH range of 2-3. [b] Optimum pH for forming metal phosphonate bilayers upon transfer. These values are consistently found to be 0.2 pH units below the characteristic pH. [c] Films are deposited at a monolayer surface pressure of 22 mN/m with dipping speeds of 8 mm/min on the downstroke and 3 mm/min on the up-stroke.

Langmuir monolayer of ODPA to a surface pressure of 22 mN/m, letting the film stabilize, and then lowering the hydrophobic substrate through the film at a speed of 8 mm/min, resulting in the transfer of a monolayer with the phosphonate head groups directed away from the surface. The substrate is then raised through the compressed monolayer at a speed of 3 mm/min, to complete a head-to-head bilayer. The slower deposition speed on the up-stroke allows excess subphase to drain leading to crystallization of the inorganic lattice.

Since the solid-state Ln[III] phosphonates are soluble below pH 2.0,[37] metal ions are not completely incorporated into the transferred ODPA LB films if the subphase pH is too low. If the subphase pH is too high, the phosphonate head groups become cross-linked by the metal ions at the water surface, and the Langmuir monolayer becomes too rigid to transfer. Isotherms such as those in Figure 2-2 are used to estimate the pH at which the inorganic metal phosphonate lattice will crystallize during the up-stroke of the deposition procedure. The "characteristic pH" determined from the π/A isotherms represents an upper limit of the subphase pH for deposition, since at this point, the LB monolayer is already too rigid to transfer. The "optimum pH" values for film transfer are consistently found to be 0.2 pH units below the "characteristic pH" value. The "optimum pH" values for each metal ion with ODPA are listed in Table 2-1.
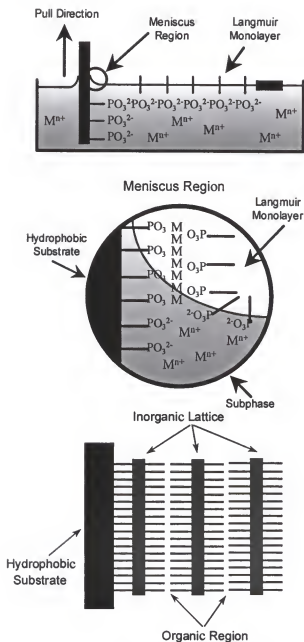
Figrue 2-3. Deposition of metal phosphonate LB films. **(top)** Scheme showing the first phosphonate monolayer deposited onto a hydrophobic substrate before withdrawing the complete bilayer. **(center)** Crystallization of the inorganic continuous lattice occurs during the upstroke of the deposition as the excess subphase drains from the polar region between the phosphonate groups. **(bottom)** Three bilayers of the metal phosphonate LB films formed by repeated cycles. In each case only one side of the substrate has been depicted for clarity.

Even when the subphase pH is adjusted to the optimum value, there is a tendency for the inorganic lattice to crosslink on the water surface over time, prohibiting the transfer of multilayer films by continuous deposition. However, "quality" multilayer samples can be prepared one bilayer at a time, where after one Y-type bilayer is transferred, the remaining Langmuir monolayer on the water surface is removed and a new ODPA monolayer is formed. A "quality" bilayer refers to a transfer ratio of 1.00 ± 0.05 on both the down-stroke and up-stroke with complete formation of the inorganic metal phosphonate continuous lattice, as evidenced by ATR-FTIR spectroscopy (discussed later in the text). For each of the metal phosphonate systems studied, this deposition technique produced quality multilayer films. Samples of up to 125 bilayers have been prepared, and no decrease in the transfer ratio was observed during deposition.

In contrast, continuous depositions at the "optimum pH" values result in transfer ratios < 0.80 ± 0.05 after two bilayers. Lowering the pH of the subphase by 0.3 pH units below the "optimum pH" values allows for continuous deposition of eight to ten bilayers with transfer ratios of unity, however, this method produces films with regions of incomplete metal phosphonate bonding.

Film Characterization by X-ray Photoelectron Spectroscopy and X-ray Diffraction

Elemental composition of the lanthanide ODP LB films is determined from X-ray photoelectron spectroscopy (XPS). XPS reveals that the only elements present are carbon, oxygen, phosphorus and the appropriate Ln^{III} metal. The observed relative signal area of the P_{2p} peak and the appropriate Ln^{III} ion peak(s) for single bilayers of each lanthanide ODP LB film are listed in Table 2-2. Using a layered model for the LB film structure[116] and accounting for differences in the photoelectron escape depths[99,117,118] which result from the different photoelectron binding energies of the P and Ln ions, the relative P_{2p} and Ln^{III} XPS peak areas

Table 2-2. Relative Intensities[a] of the Ln[III] and Phosporus[b] XPS Signals and the Bilayer Thicknesses Determined from XRD Measurements of the Lanthanide Octadecylphosphonate LB Films.

XPS Peak	Obs. Rel. Int. (± 3%)	Calc. Rel. Int.[c] (± 2%)	Bilayer Thickness[d] (± 1.0 Å)
P_{2p}	85	83	51
$La_{3d5/2}$	15	17	
P_{2p}	77	80	51
$Ce_{3d5/2}$	23	20	
P_{2p}	86	86	51
$Sm_{3d5/2}$	14	14	
P_{2p}	64	67	51
$Gd_{4d5/2}$	36	33	

[a] Intensities are reported as the percentage sum of the integrated areas of the metal and phosphorus peaks after correcting for elemental and instrumental sensitivity factors. XPS measurements were made on single bilayer Ln[III] ODPA LB films. [b] The binding energy of the P_{2p} peak is 134.5 eV for all samples, and the binding energies for the $La_{3d5/2}$, $Ce_{3d5/2}$, $Sm_{3d5/2}$ and $Gd_{4d5/2}$ are 837 eV, 886 eV, 1087 eV and 140 eV, respectively. [c] The relative intensities are calculated using a model described in ref. 23. [d] XRD measurements were performed on a 14-bilayer sample of each Ln[III] ODP LB film.
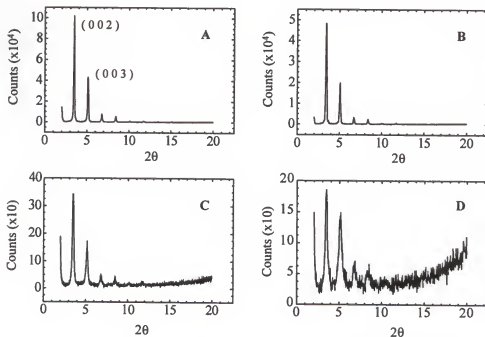
Figure 2-4. . X-ray diffraction pattern for each 14 bilayer Ln[III] ODP LB film where Ln = (A) La^{3+}, (B) Ce^{3+}, (C) Sm[3+] and (D) Gd^{3+}. The second and third order (0 0 l) Bragg reflections are indicated.

have been calculated assuming the 1:2 metal:phosphorus stoichiometry of the analogous $Ln^{III}H(O_3PR)_2$ solid-state materials (an example calculation is given in Appendix-A). These values are also listed in Table 2-2. Comparison of the observed areas with the calculated ones shows that within experimental uncertainty ($\pm 5\%$), the ODP LB films have a 1:2 metal:phosphorus ratio, consistent with the solid-state stoichiometries.

The XRD patterns from the lanthanide ODP LB films confirm the layered structure of these multilayer assemblies. Several orders of the 00l reflections are observed. Figure 2-4 shows the XRD patterns for each 14-bilayer Ln^{III} ODP LB film. The metal-metal interlayer distances are determined from the Bragg reflections, and for each of the Ln^{III} ODP LB films these distances are consistently found to be 51 ± 1Å.

Film Characterization by Infrared Spectroscopy

Analysis of the CH stretching modes in the ATR-FTIR spectra of single-bilayer and multilayer Ln^{III} ODP LB films shows that in each case the alkyl chains are closed-packed and well organized. Figure 2-5 shows ATR-FTIR spectra from 4000 to 900 cm^{-1} of the first bilayer, the second bilayer and 6 bilayers of a Gd ODP film. Peaks at 2957, 2916 and 2850 cm^{-1} are assigned to the asymmetric methyl ($v_a(CH_3)$), the asymmetric methylene ($v_a(CH_2)$) and the symmetric methylene ($v_s(CH_2)$) vibrations of the octadecyl chain, respectively. The position and shape of the C-H bands are sensitive to the conformational order and packing of the aliphatic chains in the monolayer and multilayer films.[84,119,120] The asymmetric methylene vibration occurs at 2916 cm^{-1} for each of the lanthanide ODP LB films, indicating that the C-18 alkyl chains are arranged in an all-trans conformation. The fwhm of $v_a(CH_2)$ reflects the degree to which the alkyl chains are closed-packed, and for each of the trivalent lanthanide films studied, an observed fwhm of 17 cm^{-1} indicates that the alkyl chains are organized in a closed-packed arrangement.

The intensity of the hydrocarbon stretches increases linearly (Figure 2-5) as successive bilayers are transferred, showing that each bilayer contains the same amount of ODP LB film. The structure of the outermost bilayer can be monitored by referencing the spectra of the nth bilayer to that of the $(n-1)^{th}$ bilayer. Spectra in Figure 5-5 show that the organization of the alkyl chains of the first and second bilayers of Gd ODP is similar, indicating that the substrate surface has minimal effect on the organization of these films. The structure of multilayer samples is investigated by referencing the spectra to the OTS coated Ge ATR crystal. The similarity of the shape and position of the hydrocarbon stretching modes in the spectrum of the 6 bilayer film to those of the single bilayer spectra in Figure 2-5 indicates that the structure of the transferred bilayers remain constant as additional bilayers are deposited.

The IR region between 900 and 1700 cm^{-1} can be used to determine the mode of metal-oxygen-phosphorus bonding present in the metal ODP LB films.[10] The phosphorus-oxygen vibrational modes are very sensitive to the local bonding geometry of the RPO_3^{2-}, RPO_3H^- and RPO_3H_2 groups,[121-123] and it has been previously shown that the phosphonate P-O stretches can be used to correlate the metal-phosphonate continuous lattice structures of LB films with those of known solid-state structures.[10,106,111] Figure 2-6 compares the ATR-FTIR spectrum of a lanthanum ODP LB film with those of solid-state samples of ODPA and lanthanum butylphosphonate, both prepared as KBR pellets. In the spectrum of uncoordinated ODPA, peaks occur at 1224 and 1001 cm^{-1} corresponding to P=O stretches for the free and hydrogen bonded modes,[121] respectively. These two modes are absent in the spectra of the metal coordinated solid and LB film (Figure 2-6c and Figure 2-6b, respectively). In contrast, peaks appear at 1104.5 and 978.5 cm^{-1} in the spectrum of the La ODP LB film and at 1104.5 and 978.9 cm^{-1} in the lanthanum butylphosphonate spectrum corresponding to the asymmetric and symmetric PO_3^{2-} stretching vibrations, respectively.[29] Close agreement of the shapes and frequencies of these vibrational modes indicates that the bonding geometry of the metal-oxygen-phosphorus framework within the LB film is similar to the inorganic continuous lattice structure found in the powdered solid-
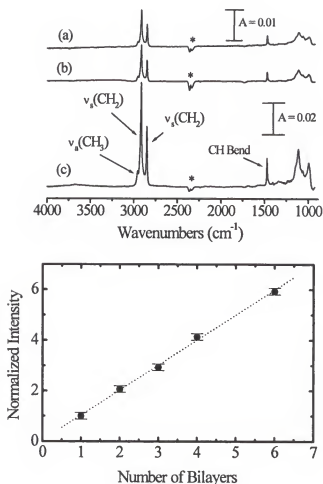
Figure 2-5. (top) ATR-FTIR spectra from 900 to 4000 cm^{-1} of (a) the first bilayer and (b) the second bilayer of a Gd ODP LB film. The spectrum of the first bilayer is referenced to the OTS coated ATR crystal, and the spectrum of the second bilayer is referenced to the first bilayer. Spectra (a) and (b) are plotted on the same scale. (c) ATR-FTIR spectrum of a 6 bilayer Gd ODP LB film (note that the absorbance scale in (c) is 1/2x that of (a) and (b)). Mode assignments are discussed in the text. The asterisks refer to the remnant CO_2 peak. (bottom) Plot of the normalized intensity of the asymmetric methylene vibration as a function of the number of bilayers for a Gd ODP LB film. The normalized intensity is defined as the intensity of $\nu_a(CH_2)$ for n bilayers divided by the intensity of the first bilayer.
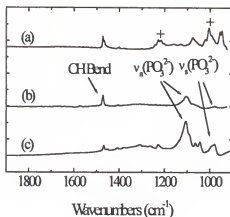
Figure 2-6. FTIR spectra from 900 to 1900 cm^{-1} of (a) a KBR pellet of ODPA illustrating the stretching vibrations of the uncoordinated R-PO$_3$H$_2$ groups, (b) a 6 bilayer La ODP LB film and (c) KBr pellet of lanthanum butylphosphonate (LaH(O$_3$PC$_4$H$_9$)$_2$) powder. Labeled peaks are discussed in the text. Spectra are scaled in intensity for easy comparison of the vibrational features of the FTIR spectra.

state analog. The phosphonate stretching modes for each of the four Ln^{III} ODP LB films are compared to those of the corresponding lanthanide butylphosphonate powders in Figure 2-7. The almost identical patterns of the phosphonate stretching modes indicates that the lanthanide ODP LB films adopt the same metal-oxygen-phosphorus bonding motifs found in the solid-state Ln^{III}H(O$_3$PC$_4$H$_9$)$_2$ powders.

Although, the complete crystal structures of the Ln butylphosphonate solids have not been solved,[29] XRD of powdered samples clearly illustrates a layered structural motif, and results from combustion analyses of the Ln butylphosphonate powders agree well with a molecular formula of Ln^{III}H(O$_3$PC$_4$H$_9$)$_2$. In addition, comparison of the FTIR spectra of lanthanum butylphosphonate and lanthanum phenylphosphonate powders (Figure 2-8b and 2-8c), indicate that the La butyl solid possesses the same metal-oxygen-phosphorus bonding geometry found in the lanthanum phenylphosphonate compound. It is instructive to contrast the Ln^{III}H(O$_3$PR)$_2$ structure to that of a different lanthanum phenylphosphonate phase, La$_2$(O$_3$PC$_6$H$_5$)$_3$·3H$_2$O. FTIR
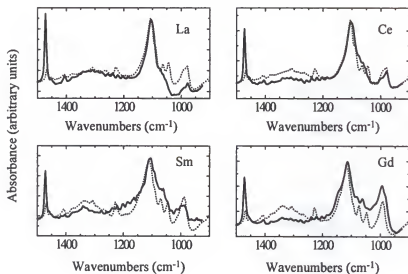
Figure 2-7. FTIR spectra from 900 to 1500 cm^{-1} of the Ln^{III} ODP LB film (solid line) and the corresponding Ln^{III} butylphosphonate powder (dashed line) for Ln = La, Ce, Sm, and Gd. Spectra are scaled for comparison of the shape and position of the R-PO$_3$$^{2-}$ stretching vibrations. The IR mode at 1463 cm^{-1} is the CH bend, and the other modes are discussed in the text

Figure 2-8. FTIR spectra of KBr pellets of the lanthanum phenylphosphonates (a)La$_2$(O$_3$PC$_6$H$_5$)$_3$·3H$_2$O, (b) LaH(O$_3$PC$_6$H$_5$)$_2$ and (c) lanthanum butylphosphonate, LaH(O$_3$PC$_4$H$_9$)$_2$ illustrating the difference between the 2:3 lanthanum:phosphonate phase and the 1:2 phases. Peaks marked by asterisks are the characteristic vibrations of the basic phase compound. Peaks between 3200 and 3700 cm^{-1} and at 1380 cm^{-1} correspond to modes of the coordinated water molecules which are absent in the 1:2 phase.

spectra of the two lanthanum phenylphosphonates are compared to the lanthanum butylphosphonate spectrum in Figure 2-8. Clearly, FTIR can be used to discern the different metal phosphonate phases, and the combination of XPS and FTIR analyses confirm that it is not the $La_2(O_3PR)_3 \cdot 3H_2O$ phase, but rather it is the $Ln^{III}H(O_3PR)_2$ phase that forms in both the butylphosphonate solids and the octadecylphosphonate LB films.

Metal Phosphonate Continuous Lattice Langmuir-Blodgett Films

In the solid-state, metal phosphonates do not form as discrete molecular complexes, but rather condense to form continuous lattice materials, and the deposition of metal phosphonate LB films generally results in single layers of the solid-state metal phosphonate architecture. However, successful deposition requires that the Langmuir-monolayer remains fluid on the water surface. This fluidity allows the continuous lattice structure to crystallize within the polar regions of organophosphonic acid LB films during the up-stroke of the deposition procedure (Figure 2-3). This process can be contrasted to the transfer of preformed crystal-like aggregates that float on the water surface. As mentioned previously, the subphase pH is a critical parameter in the condensation of the inorganic lattice and can be used to control the crystallization process that can be approximated by the equilibrium:

$$2(RPO_3H_2)_{(surface)} + Ln^{III}(H_2O)_{n(aq)} \rightleftarrows Ln^{III}H(O_3PR)_{2(s)} + 3H_3O^+_{(aq)} + (n-3)H_2O_{(l)}$$

This equilibrium indicates that if the affinity of the metal ion for the phosphonate oxygens is high, then a lower subphase pH is required to keep the equilibrium shifted to the left to maintain a fluid monolayer. On the other hand, if the affinity of the metal ion is low, then the pH can be raised to help incorporate the metal ions into the LB film.

The affinity of the metal ions for the octadecylphosphonic acid Langmuir monolayer is reflected in the "characteristic pH" values determined from π/A isotherms and in the "optimum pH" values chosen for film transfer. The "characteristic pH" values range from pH 2.7 to pH 3.4
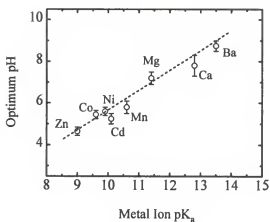
Figure 2-9. Relationship between the optimum pH of transfer of divalent metal phosphonate LB films and the metal ion pKa values.

for the trivalent lanthanide metal ions studied, and these values are lower than the range of 5.0 -

6.0 found for the divalent transition metal ions[10] Mn^{2+}, Cd^{2+}, Co^{2+} and Cd^{2+} and the range of 7.0 –

9.0 for the divalent alkaline earth metal ions[10,111] Mg^{2+}, Ca^{2+} and Ba^{2+}. The pH at which the

metal ions in the subphase begin to associate with phosphonic acid monolayer increases in the

order trivalent lanthanide metal ions < divalent transition metal ions < alkaline earth metal ions,

indicating that the affinity of the metal ion for the phosphonate monolayer parallels the acidity of

the metal ions in aqueous solution. The pKa of a metal ion is a general guide to its oxophillicity,

and here pKa reflects the metal ion's affinity for the compressed phosphonate monolayer, where a

lower pKa value indicates a stronger affinity. In fact, a relatively linear relationship is observed

for the optimum pH of transfer and the metal ion's pKa value for divalent metal ions. This

relationship is depicted in Figure 2-9. This finding is similar to results of metal ion interaction

with fatty acid monolayers where the affinity followed the trend divalent transition metal ions <

trivalent lanthanide metal ions, with the order of the transition metals following inversely their

degree of hydration.[113-115]

Many metal ions are known to form layered phosphonates, and the ion's pKa can be used to estimate whether or not a metal phosphonate LB film can be formed using this standard deposition process. The technique has been used successfully to form crystalline 2D metal phosphonate films containing the divalent metal ions Mn^{2+}, Cd^{2+}, Co^{2+}, Mg^{2+}, Ca^{2+} and Ba^{2+}, and as described here, the trivalent lanthanide ions La^{3+}, Ce^{3+}, Sm^{3+} and Gd^{3+}. For ODPA, it is observed that the deposition process is successful when the metal ion has an aqueous pKa value between 3 and 14 because this range sets practical limits for controlling the subphase pH (this range will vary if the organophosphonic acid is changed). For metal ions such as Fe^{3+} and Zr^{4+} with pKa values of 2.2 and -0.4,[124] respectively, this Y-type deposition technique is unsuccessful because the strong oxophillicity of these ions results in the formation of rigid monolayers even if the subphase is adjusted to pH 1.0. The rigidity of the film prevents successful transfer of the monolayer onto a solid support. For example, on a Zr^{4+} subphase, the octadecylphosphonic acid monolayer is cross-linked to such an extent that small crystalline islands have been observed by Brewster angle microscopy.[108] With these strongly oxophillic ions, an alternative three-step deposition process was developed that takes advantage of the strong affinity of these ions for the phosphonate monolayer.[5,6] Although the three-step process results in the successful transfer of nearly any phosphonic acid monolayer, films prepared this way possess an amorphous inorganic network.

Conclusion

Metal phosphonate LB films based upon solid-state Ln^{III} phosphonates can be prepared by a Y-type deposition procedure. Spectroscopic investigations show that these films possess the same 2D continuous lattice structure found in the analogous $Ln^{III}H(O_3PR)_2$ solid-state materials and provide another example of a continuous lattice architecture that can be incorporated into organophosphonic acid LB films. The inorganic lattice forms on the up-stroke of the Y-type

deposition procedure and has a strong dependence on the subphase pH. The trivalent Ln OPD LB films form at a lower pH than the previously studied divalent metal phosphonate LB films, and this parallels the pH dependence for formation of the solid-state compounds where their stability towards acidic solutions increases in the order alkaline earth metals < divalent transition metals < trivalent lanthanide metals. The affinity of the metal ions for the phosphonic acid monolayers also follows this trend and is inversely related to the aqueous pKa of the metal ions. The pKa of a metal ion can be used as a general guide for determining the conditions for forming a crystalline metal phosphonate LB film.

CHAPTER 3

ZIRCONIUM, CADMIUM AND MANGANESE METAL PHOSPHONATE LANGMUIR-
BLODGETT FILMS OF PHENOXY SUBSTITUTED PHOSPHONIC ACIDS

Introduction

The Langmuir-Blodgett (LB) method is an elegant technique that provides a way to organize amphiphilic molecules on a water surface with subsequent transfer of the monolayer assembly to a solid support, and organized assemblies of amphiphilic molecules have been prepared using LB techniques for a variety of applications.[79,83,107] In particular, LB films of functionalized molecules are of interest because of their potential use in areas such as chemical sensing, molecular electronic devices and non-linear optics.[83,125] LB films, with separate polar and non-polar regions offer the possibility of incorporating function into either of these regions, and although derivatized organic amphiphiles have received tremendous attention to this end, less effort has been spent investigating films where physical properties are derived from metal ions,[83,126,127] metal complexes,[128] or continuous lattice structures[5,7,10,106] incorporated into the polar regions of the films.

The concept of preparing LB films containing a continuous inorganic lattice has recently been introduced by modeling the films after transition metal phosphonates[11,12,16,37] which are known layered extended solids. Recent work has shown that it is possible to incorporate known two-dimensional metal phosphonate inorganic lattice structures into LB films of octadecylphosphonic acid (ODPA), and films formed with a variety of divalent, trivalent and tetravalent metals have been described.[5,10,111] In each case, a known metal phosphonate layered

65
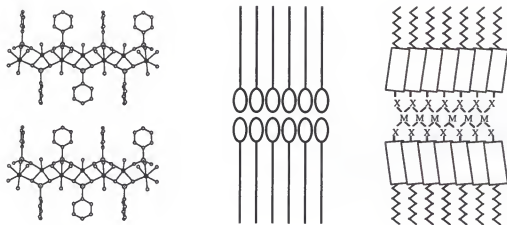
Figure 3-1. Comparison of 'dual-network' metal phosphonate LB films to polycrystalline metal phosphonate solids. **(left)** Layered structure of manganese phenylphosphonate (crystallographic data are taken from ref.16). **(center)** Representation of a Y-type LB film where the balls and sticks represent the polar and non-polar regions, respectively. **(right)** A 'dual-network' functionalized metal organophosphonate LB film containing a 2D metal phosphonate continuous lattice in the polar region and a molecular solid network in the non-polar region.

structure was observed in the polar region of head-to-head octadecylphosphonate bilayers. In the films, it is possible to tune the metal phosphonate bonding geometry among known solid-state bonding motifs by changing the metal ion,[10] which can also have subsequent effects on the packing of the organic groups.

LB films based upon the metal phosphonate architecture provide a way to form "dual-network" mixed organic/inorganic assemblies of functionalized phosphonic acids where both the separate inorganic and organic components can add physical properties (Figure 3-1). The strong ionic/covalent bonding of the inorganic continuous network adds substantial stability to the LB films, and it can also be used to introduce physical phenomenon such as magnetic order. For example, the manganese octadecylphosphonate, $Mn(O_3PC_{18}H_{37})H_2O$, film was the first example of a magnetic LB film, showing spontaneous magnetization and magnetic memory effects below the magnetic ordering temperature of 13.8 ± 0.2 K.[10] At the same time, functionalized organic groups can be incorporated into the non-polar regions of the films to add physical properties such as non-linear optical responses or molecule-based conductivity.

OC_nX_{2n+1}

$C_mH_{2m}P(O)(OH)_2$

C_mX_{2m+1}

$PO(OH)_2$

1 (P0A) X=H, n=18, m=0
2 (P4A) X=H, n=14, m=4
3 (dP4A) X=D, n=14, m=4

4 (ODPA) X=H, m=18
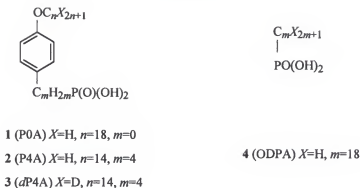
Figure 3-2. Organophosponate amphiphiles used to prepare alternating layer and symmetric layer metal phosphonate LB films.

Since previous metal phosphonate LB films have been formed only with ODPA, there was motivation to explore the range of organic functional groups that could be assembled into metal phosphonate LB films. The work presented in this chapter describes a series of zirconium, cadmium and manganese phosphonate LB films where the organophosphonic acids contain phenoxy groups at different positions along the organic tail. The organophosphonic acids (**1-4**) used are shown in Figure 3-2, and Figure 3-3 presents a summary of the naming scheme and architecture of the films prepared in this study. The acronyms for the phenoxy substituted phosphonic acids are P4A and P0A, where the letter P represents the phenoxy moiety and the number indicates the how many carbon atoms separate it from the phosphonic acid head group.

Although the zirconium phosphonate lattice does not add any potentially interesting optical, electronic, or magnetic properties to the organic/inorganic assemblies, the strong oxophilicity of the Zr^{4+} ion brings high inorganic lattice energy to the layered films, making the LB films extremely stable.[5,109] In fact, since the zirconium/phosphonate interaction is so strong, the usual LB deposition procedure where metal ions are present in the subphase is not possible because the zirconium ions cross-link the organophosphonate Langmuir monolayers, making the films too rigid to transfer.[5] Alternatively, a previously developed stepwise deposition procedure (Figure 3-4) that takes advantage of the strong zirconium ion oxophilicity is used to prepare
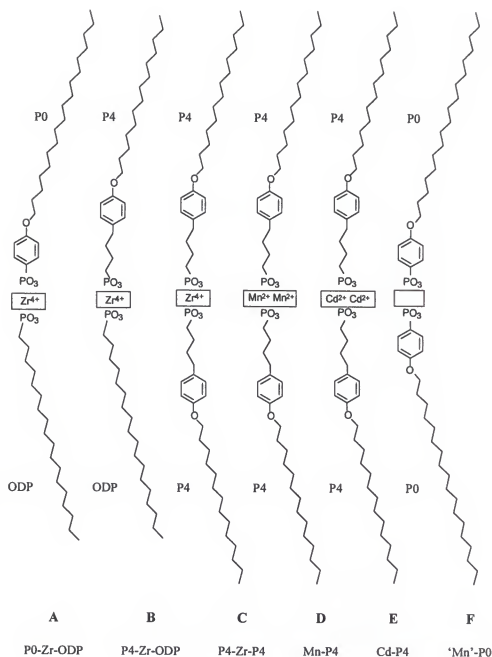
Figure 3-3 Phenoxy substituted organophosphonate films prepared with zirconium, manganese or cadmium metals.

Step 1. Formation of the LB Template Monolayer
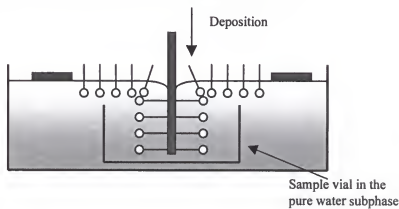
Step 2. Zirconation of the Template Monolayer
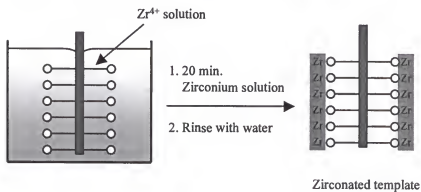
Step 3. Formation of the LB Capping Monolayer
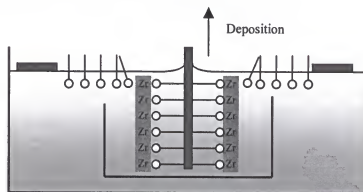
Figure 3-4. Three-step procedure for the deposition of zirconium phosphonate LB films.

zirconium phosphonate LB films. The discrete stepwise nature of this deposition procedure allows for convenient fabrication of symmetric as well as alternating-layer Y-type LB films and permits complete structural characterization of the individual layers deposited on either the down-stroke or the up-stroke of the deposition cycle.[129,130]

In addition to the zirconium phosphonate films, LB films of 4-(4'-tetradecyloxy-phenyl)butylphosphonic acid (P4A, **1**) have been formed with the $M^{II}(O_3PR)H_2O$ continuous lattice structure (M^{II} = Mn or Cd) and the magnetic properties of the manganese film are reported. These films are referred to as Mn-P4 and Cd-P4.

Although the phenoxy substituent does not add any interesting optical or conducting properties, it has been chosen as a model compound to determine whether aryl groups can be organized within the packing motif of the zirconium and divalent metal phosphonate lattice frameworks and to investigate how the larger organic group affects the magnetic interactions in the layered manganese phosphonate network. The following sections provide information regarding the detailed structural characterization of the previously mentioned films (Figure 3-3). Structural characterization of all films consists of X-ray diffraction (XRD), X-ray photoelectron spectroscopy (XPS) and Fourier transform infrared (FTIR) spectroscopic studies, and the magnetic properties of the Mn-P4 LB film were investigated by electron spin resonance (EPR) and static magnetometry measurements. The Mn-P4 film is only the second example of a continuous lattice LB film exhibiting spontaneous magnetization.

The results of these studies show that it is possible to incorporate the phenoxy group within the metal phosphonate LB films, and for the case of the Mn-P4 films, this larger aryl group does not disrupt the structure or the magnetic exchange pathways of the inorganic continuous lattice network. In addition, this model study reveals that the position of the phenoxy group along the alkyl chain is an important parameter that affects the quality and processibility of the Langmuir monolayers. The organizational quality of the Langmuir monolayers of these functionalized organophosphonates affects both the deposition and the ability to form the

crystalline two-dimensional metal phosphonate continuous inorganic lattice within the polar region of the deposited film.

Experimental Details

Materials Used

4-Octadecyloxyphenylphosphonic acid (P0A, $C_{24}H_{43}O_4P$, 1), 4-(4'-tetradecyloxyphenyl)butylphosphonic acid (P4A, $C_{24}H_{43}O_4P$, 2), 4-(4'-d_{29}-tetradecyloxyphenyl)butylphosphonic acid (dP4A, $C_{24}H_{14}D_{29}O_4P$, 3) were supplied by Melissa Petruska.[129] Octadecylphosphonic acid (ODPA, $C_{18}H_{39}O_3P$, 4), was obtained from Alfa Aesar (Ward Hill, MA) and used as supplied. Octadecyltrichlorosilane (OTS, $C_{18}H_{37}SiCl_3$, 95%) and zirconyl chloride ($ZrOCl_2$, 98%) were purchased from Aldrich (Milwaukee, WI). $MnCl_2 \cdot 6H_2O$ (99.6%) and $CdCl_2 \cdot 5/2H_2O$ (99.7%) were purchased from Fisher Scientific and used as received. HPLC grade chloroform, stabilized with amylene, was used as received from Acros (Pittsburgh, PA). A Barnstead NANOpure purification system produced water with an average resistivity of 18 MΩ cm for all experiments.

Substrate Preparation

Single crystal (1 0 0) silicon wafers were purchased from Semiconductor Processing Company (Boston, MA) and were used as deposition substrates for XPS measurements. Samples for XRD studies were deposited onto glass petrograph slides that were purchased from Beuhler, Ltd. (Lake Bluff, IL). Silicon and glass substrates were cleaned using the RCA cleaning procedure[112] and dried under N_2. Silicon and germanium attenuated-total-reflectance (ATR) crystals, 50 mm x 10 mm x 3 mm with 45° faces, purchased from Wilmad Glass (Buena, NJ), were used as substrates for ATR-FTIR experiments. Germanium ATR crystals were cleaned by an oxygen-plasma etch and washed with chloroform in a Soxhlet extractor before use. These

substrates were made hydrophobic by deposition of a monolayer of OTS.[84,96] Mylar sheets (Dupont, DE) were coated with 5 bilayers of calcium arachidate to improve the hydrophobicity of the surface and were used as substrates for EPR and magnetization measurements.

Instrumentation Details

The LB experiments were performed using KSV Instruments (Stratford, CT) 5000 and 3000 systems with homemade Teflon troughs modified to operate with double barriers. Pressure versus area (π/A) isotherms were recorded on either of these systems with surface areas of 794 cm^2 (12.8 cm x 67 cm) and 960 cm^2 (12.8 cm x 75 cm) for the 3000 and 5000 instruments, respectively. Surface pressure was measured with a platinum Wilhelmy plate suspended from a KSV microbalance. For studies of LB film behavior as a function of subphase pH, the appropriate amount of 0.012 M HCl or 0.01 M KOH was used to adjust the pH of the aqueous subphases which were prepared in 2 L volumetric flasks. The pH of the subphase was stable over the time scale of the experiments.

Infrared spectra were recorded on a Mattson Instruments (Madison, WI) Research Series-1 FTIR spectrometer with either a mercury-cadmium-telluride (MCT) or deuterated triglycine sulfate (DTGS) detector. LB films were deposited onto OTS-coated Si or Ge ATR parallelograms, and a Harrick (Ossing, NY) TMP stage was used for the ATR experiments. Polarized ATR-FTIR spectra were taken with *s*- and *p*-polarized light. All ATR-FTIR spectra consist of 1000 scans at 4 cm^{-1} resolution and were referenced to the appropriate background.

XRD patterns were obtained with a Phillips APD 3720 X-ray powder diffractometer with the CuKα line, λ = 1.54 Å as the source. XPS was performed on a Perkin-Elmer (Eden Prairie, MN) PHI 5000 series spectrometer. All spectra were taken using the MgKα line at 1253.6 eV. The spectrometer has a typical resolution of 2.0 eV, with anode voltage and power settings of 15 kV and 300 W, respectively. Typical operating pressure was 5x10^{-9} atm. All XPS spectra were

recorded with a 45° take-off angle. Survey spectra consisted of 5 scans performed with 0.5 eV/step, 20 ms/step and a pass energy of 89.45 eV. Multiplex spectra consisted of 80 scans per region taken in 10 sweeps/cycle operating at 0.1 eV/step, 50 ms/step, and a pass energy of 37.75 eV.

A 52-bilayer Mn-P4 LB film (26 bilayers per side of the substrate) was used for EPR measurements. EPR spectra were recorded on a Bruker (Billerica, MA) ER 200D spectrometer modified with a digital signal channel and a digital field controller. Data were collected using a U.S. EPR (Clarksville, MD) SPEC300 data acquisition program and converted to ASCII format using a U.S. EPR (Clarksville, MD) EPRDAP data analysis program. The ASCII data were then imported into the program Microcal[TM] Origin[TM] Vs. 4.1 and the area was integrated using a macroscript, the details of which are given in Appendix-A. The temperature was controlled by an Oxford Instruments (Whitney, England) ITC 503 temperature-controller and an EPR 900 continuous flow liquid helium cryostat. Magnetization measurements were performed with a Quantum Design MPMS SQUID magnetometer using similar procedures to those used in studies of Mn-ODP LB films.[10] A gelcap and plastic straw were used as a sample holder during the measurements. Magnetization measurements were made on the same 52-bilayer Mn-P4 LB film sample used for EPR measurements. This sample was prepared and cut into small pieces and oriented in a gelcap. Measurements were performed for orientations parallel and perpendicular to the substrate surface. The temperature dependent magnetization was measured upon warming the film between 5 K and 25 K and recorded with a measuring field of 0.01 T for both the zero-field cooled (ZFC) data and field cooled (FC) data. Field cooled data were acquired after cooling the sample in an applied field of 0.1 T.

Results and Discussion

Langmuir-Monolayers

Amphiphiles P0A and P4A, were characterized at the air/water interface as a function of pH for pure water and 0.5 mM M^{II} (M = Mn or Cd) subphases. Monolayer behavior of dP4A, where the fourteen-carbon segment is deuterated, was the same as that of P4A under all conditions studied.

Figure 3-5 shows pressure vs. area (π/A) isotherms of ODPA, P4A and P0A during compression on a pure water subphase at pH 5.5. The P4A amphiphile forms a stable monolayer on a pure water subphase, and its isotherm has a well-defined solid compression region where the film collapses at an area of 24.8 ± 0.3 Å^2/molecule at this pH. Film collapse is defined here as the point on the compression curve where deviations from linearity of the solid compression region are first observed. This collapse area of 24.8 ± 0.3 Å^2/molecule is greater than the 20 Å^2/molecule for ODPA the on same subphase.[131] A mean molecular area between 24 and 25 Å^2 corresponds nicely to the cross-sectional area of a phenoxy unit oriented with its long axis tilted slightly from the normal to the surface and indicates that interactions between the aromatic groups are responsible for determining the area per molecule within the Langmuir-monolayers.[132]

The isotherm of P0A on a pure water subphase shows a mean molecular area at collapse of 24.3 ± 0.3 Å^2/molecule, which is similar to the area observed for P4A and reflects the presence of the phenyl group in this molecule. However, the slope of the solid compression region is not as steep as that observed in the isotherm of P4A, and this film collapses at a lower surface pressure. The shallower slope results from some disorder in the packing of the film. Unlike P4A, where the four-carbon tether between the aromatic and phosphonate groups provides flexibility, the phenyl group in P0A is incorporated into a position adjacent to the head group where the packing requirements of both the aryl group and the phosphonate group appear to hinder the
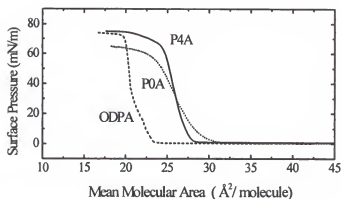
Figure 3-5. Pressure vs. area isotherms for ODPA, P4A and P0A on a pure water subphase at pH 5.5. The spreading solutions used had concentrations between 0.2 and 0.4 mg/ml in CHCl₃ for ODPA, and in 10% EtOH/CHCl₃ for both P4A and P0A.

formation of a quality Langmuir-monolayer. The poorer film quality of P0A is also apparent during film deposition, as discussed below.

Studies of π/A isotherms for both P4A and P0A on a pure water subphase as a function of pH show that at higher pH, typically greater than 7, the slopes of the solid compression region become more shallow and the films become less stable (collapse occurs at a lower pressure and the onset of pressure occurs at a higher MMA). These effects arise presumably from ionization of the phosphonic acid leading to the occurrence of repulsive forces between the now negatively charged head-groups.

Isotherms of P4A and P0A as a function of pH for 0.5 mM Mn²⁺ subphases are shown in Figure 3-6 and Figure 3-7, respectively. In general, interactions between the floating monolayers and metal ions in the subphase can be determined from π/A compression isotherms measured as the subphase pH is changed.[111,113-115] As shown in Figure 3-6, for P4A monolayers, at low pH the isotherm closely resembles that of P4A on a pure water subphase, indicating that at this pH the metal ions are not interacting with the phosphonate head groups. This point can be seen by
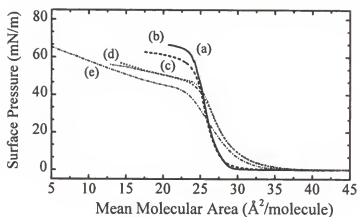
Figure 3-6. Isotherms of 4-(4'-tetradecyloxyphenyl)butylphosphonic acid (P4A, **2**) on 0.5 mM Mn^{2+} subphases at pH (a) 3.0, (b) 3.5, (c) 4.0, (d) 4.4 and (e) 4.7.
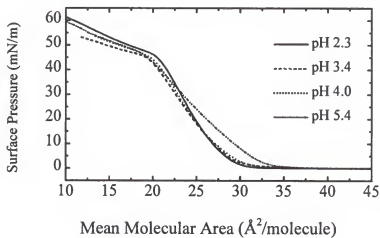
Figure 3-7. Isotherms of 4-octadecyloxyphenylphosphonic acid (P0A, **1**), on 0.5 mM Mn^{2+} subphases at pH 2.3, 3.4, 4.0, and 5.4.

noting the similarity of the isotherm of P4A in Figure 3-6 (on a 0.5 mM Mn^{2+} subphase at pH 3.0) to that of P4A in Figure 3-5 (on a pure water subphase). For the P4A monolayer on the 0.5 mM Mn^{2+} subphase, as the pH is increased to 4.0, the isotherm shape looks different from that on the pure water subphase. Here, the collapse pressure decreases and the compression isotherm becomes less steep, indicating that the metal ions are beginning to associate with the monolayer. Above pH 4.4, the shape of the isotherm indicates that the monolayer has become rigid as a result of cross-linking of the phosphonate head groups by the metal ions. Almost identical behavior was observed for monolayers of P4 on 0.5 mM Cd^{2+} subphases as a function of pH.

The isotherms of P0A on 0.5 mM Mn^{2+} subphases as a function of pH are shown in Figure 3-7. For this amphiphile, the interactions between the floating monolayer and the metal ions in the subphase are harder to discern. For a suphase pH range of 2.0 – 4.4, the shapes of the π/A isotherms look similar to those of P0A on a pure water subphase, but two differences can be noticed. First, the film collapses at a lower pressure on the 0.5 mM Mn^{2+} subphase, and secondly, the MMA at collapse is lower for the monolayers on the Mn^{2+} subphases. Above pH 4.7, the isotherms become more expanded indicating that the metal ions have cross-linked the phosphonate monolayer at the water surface. Almost identical behavior and pH dependence was observed for monolayers of P0A on 0.5 mM Cd^{2+} subphases.

Deposition of Films

The metal phosphonate films studied here are deposited in a head-to-head / tail-to-tail (Y-type) manner by use of either a three step combined Langmuir-Blodgett / self-assembly procedure[5] or a more conventional Langmuir-Blodgett deposition process.[7,10] The three step procedure is necessary for the Zr^{4+} films because the strong oxophilicity of this metal ion cross-links the organophosphonate monolayers on the water surface making the film too rigid to transfer to the substrate. The two deposition methods employed are described in detail below.

Deposition: zirconium phosphonate LB films

The zirconium organophosphonate films depicted in Figure 3-3 are prepared by use of a three-step deposition procedure that was developed previously for preparing LB bilayers of zirconium octadecylphosphonate.[5] As illustrated in Figure 3-4, the first step involves creation of a LB monolayer by dipping a hydrophobic substrate down through a compressed monolayer on a pure water subphase into a vial sitting in the dipping well of the trough. The layer deposited on the down-stroke is referred to as the template layer. The Langmuir monolayer is then decompressed and the vial containing the template-coated substrate is removed from the trough. In the second step $ZrOCl_2$ is added to the vial containing the substrate to bring the zirconium ion concentration in the vial to 5 mM. These conditions permit zirconium binding to the phosphonic acid, and after 20 minutes the substrate containing the zirconated template layer is removed from the solution and rinsed with pure water. The zirconated template is a stable structure, and information regarding its organization and structure can be obtained. Without zirconation, however, the template monolayer is metastable, and characterization cannot be performed. For the final step, the substrate containing the zirconated template is next returned to the trough, which is filled with a fresh subphase of pure water. A new Langmuir monolayer is compressed at the air-water interface, and a new LB monolayer is deposited as the substrate is drawn upward through the film. The layer deposited onto the zirconated template is referred to as the capping layer. This capping layer can also be individually characterized. Multilayer assemblies can be prepared by repeating this three-step procedure.

By exploiting the versatility of this deposition procedure, particularly the ability to prepare bilayers where the template layer is different from the capping layer, a variety of Y-type zirconium organophosphonate LB films can be generated.[129,130] Table 3-1 lists the deposition conditions used to prepare the zirconium LB films shown in Figure 3-3. Transfer ratios for all the films were 1.1 ± 0.15. For depositions, all LB films were compressed with maximum barrier

speeds of 10 mm/min. Typically 200-350 μL of a 0.3 mg/mL solution was spread on the water surface for each experiment. The compressed monolayer films were allowed to stabilize 5-20 minutes before they were transferred to the substrate.

In addition to using ODPA as a template layer, template layers can be formed with P4A. However, despite several attempts under various conditions, quality template layers of P0A monolayers could not be deposited. This difference in behavior indicates that the position of the aryl group along the aliphatic chain plays a significant role in the processability of these Langmuir monolayers. Indeed, a difference in the monolayer behavior of P4A, with a four-carbon tether between the phenoxy moiety and the phosphonate head group, and P0A, where the aryl moiety is adjacent to the phosphonate group, is also observed. Recall that the π/A isotherms show that the P0A amphiphile forms poorer quality monolayers on the water surface. Presumably, the preferred packing arrangement of the phenyl rings precludes a favorable arrangement of the phosphonic acid head-groups leading to a less stable monolayer on the water surface. In contrast, the four-carbon tether in P4A separates the aryl group from the phosphonate head group leading to a more organized and processable film. The four-carbon tether allows the two sections of the molecule to organize relatively independently of one another, separating the polar head-group from the constraints of the packing of the aromatic groups. This flexibility of the head-group leads to well-behaved isotherms and to successful down-stroke depositions of P4A monolayers.

Although quality template layers of P0A could not be formed, these films, along with P4A, can be successfully deposited as capping layers. Here, the position of the organic moiety along the alkyl chain has less influence on the film processability because the transfer of the capping layers is aided by the affinity of the phosphonate groups for the zirconium ions on the substrate. The strength of this interaction is the driving force for the deposition of the capping

Table 3-1. Deposition Conditions^a for Preparation of Phenoxy Substituted Metal Organophosphonate LB Films.

Film	Subphase	Subphase pH	Target Pressure^d (mN/m)	Dipping Speed (mm/min) ↓	↑
Template Monolayers^b					
ODP	nH$_2$O	5.0 – 6.0	20	10	
P4	nH$_2$O	5.0 – 6.0	25	3	
Capping Monolayers^c					
P4	nH$_2$O	5.0 – 6.0	25	NA	
P0	nH$_2$O	5.0 – 6.0	20	NA	
Y-type Bilayers					
P4	0.5 mM Mn^{2+}	4.2 – 4.5	24	3	
	0.5 mM Cd^{2+}	4.2 – 4.5	24	3	
P0	0.5 mM Mn^{2+}	3.8 – 4.1	17	8	

^{a} For all depositions, films were compressed with barrier speeds of 10 mm/min. ^{b}Template layers were initially transferred onto an OTS coated substrate. ^{c} Deposition conditions for the capping layers are the same regardless of the identity of the zirconated LB template monolayer. ^{d} Target pressures correspond to an area of 24 ± 1 Å/molecule for films of ODP and 27 ± 1 Å/molecule for P4 and P0 films.

monolayers, and it overcomes any rigidity or disorganization of the monolayer on the water surface. The transfer of P0A and P4A onto zirconated ODP template layers produced alternating layer films of P0-Zr-ODP and P4-Zr-ODP, respectively. In addition, the transfer of P4A capping layers onto a zirconated P4 template layers produced symmetric bilayer films of P4-Zr-P4. The various zirconium phosphonate LB films formed are summarized in Figure 3-3.

Deposition: manganese and cadmium phosphonate LB films

M^{II}-P4. In contrast to the deposition of zirconium phosphonate LB films, formation of divalent metal phosphonate LB films proceeds by a more traditional Y-type deposition procedure where one bilayer of a continuous lattice metal phosphonate film is formed during each deposition cycle (Figure 3-8). It has recently been demonstrated that metal phosphonate LB films are formed by transferring phosphonic acid monolayers from aqueous subphases containing the appropriate metal ions.[10,106,111] The two-dimensional continuous inorganic lattice crystallizes,

when bilayers are formed, during the up-stroke of the deposition. A variety of LB films of ODPA with formulas $M^{II}(O_3PR)H_2O$ ($M^{II} = Mn^{2+}$, Cd^{2+}, Co^{2+} and Mg^{2+}); $M^{II}(HO_3PR)_2$ ($M^{II} = Ca^{2+}$ or Ba^{2+}); and $Ln^{III}H(O_3PR)_2$ ($Ln^{III} = La^{3+}$, Ce^{3+}, Sm^{3+} and Gd^{3+}) ($R = C_{18}H_{37}$) have been prepared where the inorganic network has the same structure as the corresponding solid-state metal phosphonate of the same formula.[10,106,111] Crystallization of the continuous metal phosphonate inorganic lattice in divalent and trivalent metal octadecylphosphonate LB films depends strongly upon the subphase pH. If the pH is too low, the metal phosphonate continuous lattice does not form in the transferred LB films. If the subphase pH is too high, the metal ions cross-link the phosphonate head groups on the water surface, and the Langmuir monolayer becomes too rigid to transfer. Isotherms such as those in Figure 3-6 are used to estimate the subphase pH where quality metal phosphonate LB bilayers are deposited. A quality bilayer means 100% transfer from the water surface to the solid substrate on both the down-stroke and up-stroke of the deposition process with complete formation of the metal phosphonate continuous lattice. From Figure 3-6, the optimum subphase pH range to deposit quality bilayers of P4 with manganese ions is pH 4.0 - 4.4. This same pH range was also provides the optimum conditions for the transfer of quality Cd-P4 films.

The deposition of M^{II}-P4 LB films onto a solid support proceeds by compression of the Langmuir-monolayer to a surface pressure of 25 mN/m, letting the film stabilize for 3-5 minutes, and then lowering the hydrophobic substrate through the film at a speed of 3 mm/min. The substrate is then raised through the compressed monolayer at a speed of 1 mm/min, to complete a head-to-head bilayer. The slower deposition speed on the up-stroke allows the excess subphase to drain with the crystallization of the inorganic lattice. However, even within the optimum pH range, the monolayers of P4A become too rigid to transfer after an extended time period. This gradual increase in film rigidity prevents the continuous deposition of multilayer samples and has also been observed for other metal phosphonate LB films.[10] Consequently, after the deposition of
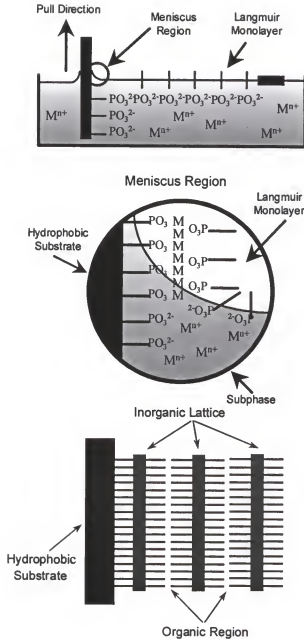
Figure 3-8. Deposition of metal phosphonate LB films. **(top)** Scheme showing the first phosphonate monolayer deposited onto a hydrophobic substrate before withdrawing the complete bilayer. **(center)** Crystallization of the inorganic continuous lattice occurs during the upstroke of the deposition as the excess subphase drains from the polar region between the phosphonate groups. **(bottom)** Three bilayers of the metal phosphonate LB films formed by repeated cycles. In each case only one side of the substrate has been depicted for clarity.

one bilayer, the monolayer is cleaned from the water surface and a new monolayer is spread. Repeated deposition results in multilayer assemblies.

M^{II}-P0. Although the amphiphile P0A forms poorer quality monolayers on the water surface and could not be successfully transferred from pure water subphases, films of P0A were deposited from a 0.5 mM Mn^{2+} subphase at pH 4.0. The conditions used to deposit this film are similar to those of P4A (Table 3-1), however a faster deposition speed of 8 mm/min on the down-stroke was necessary for film transfer. Transfer ratios during deposition for both the up-stroke and down-stroke were 1.0 ± 0.2. However, as will be shown below by FTIR and XPS analyses, these films do not contain Mn^{2+} ions and hence, the two-dimensional metal phosphonate lattice is not formed within this film. This film is referred to as 'Mn'-P0 since the counter-ions in the subphase are required for successful transfer of the organic film but are not included in the transferred assembly. No effort was made to transfer the P0A film with cadmium ions because similar behavior is expected.

Because the P0A amphiphile forms poorer quality monolayers on the water surface, it is difficult to infer from the π/A isotherms as a function of subphase pH the interactions between the monolayers and the metal ions. However, depositions where the subphase pH was outside of the range of $3.8 - 4.1$ resulted in very poor transfers (typically < 50%).

X-ray Photoelectron Spectroscopy Measurements

XPS is used to provide the relative percentages of metal ions and phosphorus atoms present in the films, and the results are used to determine the metal:phosphorus stoichiometry.[10] In addition, XPS measurements can be used to survey the identity of all elements present in the films.[133,134] Unless stated otherwise, the XPS measurements were performed on single bilayer films or zirconated template monolayer samples.

XPS: zirconium phosphonate LB films

The XPS results of each zirconium phosphonate film in Figure 3-3 and of the zirconated ODP and P4 templates show that C, O, P, and Zr are the only elements present in each film. Table 3-2 lists the relative percentages of Zr and P observed for each sample. The values are determined by integrating the areas of the P_{2p} and the Zr_{3d} peaks and accounting for instrumental sensitivity factors. Within the uncertainty of the XPS method (±3%),[135] the observed Zr:P ratio of the zirconated ODP and zirconated P4 templates is 1:1, indicating that after zirconation, one zirconium ion is bound for each phosphonate group in the template layer. An example of an XPS multiplex spectrum for a single bilayer P0-Zr-ODP LB film is shown in Figure 3-9.

For the bilayer samples, the Zr:P ratios are all near 1:2, indicating complete transfer of the capping layer. The stoichiometric ratios have been calculated without correcting for differences in photoelectron escape depths because the energies of the Zr_{3d} (185.9 eV, 183.6 eV) and P_{2p} (134.3 eV) photoelectrons are similar and the Zr and P atoms are at nearly the same depth in the films, which lead to corrections that are < 1% of the observed intensities.[116] The 1:2 ratio is consistent with the Zr:P ratios and the ionic charges present in solid-state zirconium organophosphonates of formula $Zr(O_3PR)_2$.[43]

XPS: manganese and cadmium phosphonate LB films

The XPS results reveal that only C, O, P and the corresponding metal (Mn or Cd) are present in each M^{II}-P4 film sample. Table 3-2 lists the relative areas of the observed P_{2p} and M^{II} ($Mn_{2p3/2}$, $Cd_{3d5/2}$) photoelectron peaks in single bilayers of M^{II}-P4 LB films. The values are determined by integrating the areas of the P_{2p} and the corresponding M^{II} peaks and accounting for instrumental sensitivity factors. The solid-state divalent metal phosphonate materials of formula $M^{II}(O_3PR)H_2O$ have a 1:1 metal:phosphorus stoichiometry, and the observed XPS areas are within 5% of those expected for this structure assuming a layered film geometry and accounting
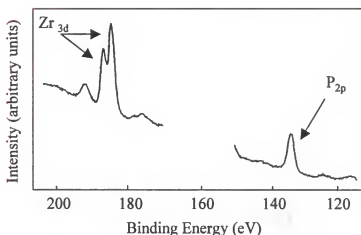
Figure 3-9. XPS multiplex spectrum of a one bilayer P0-Zr-ODP LB film. Labeled peaks correspond to the signals detected for the $Zr_{3d3/2}$, $Zr_{3d5/2}$ and P_{2p} photoelectrons.

Table 3-2. Bilayer Thicknesses[a] and Relative Intensities[b] of XPS Peaks for Phenoxy Substituted Metal Phosphonate LB Films.

Film	Bilayer thickness[a] (± 1Å)	Bilayer thickness calculated[c]	XPS obs. rel. int. (± 3%)		XPS cal. rel. int.[d] (± 1%)		P:M ratio[e]
			% P	% M	% P	% M	
Zirconated templates							
Zr-ODP	NA	NA	52	48	50	50	1:1
Zr-P4	NA	NA	52	48	50	50	1:1
Bilayer samples							
P0-Zr-ODP	53	51	69	31	66	34	2:1
P4-Zr-ODP	52	51 – 53	64	36	66	34	2:1
P4-Zr-P4	56	52 – 55	68	32	66	34	2:1
Mn-P4	51	49 – 53	63	37	60	40	1:1
Cd-P4	51	48 – 52	49	51	47	53	1:1

[a] Interlayer spacings are determined from XRD patterns of samples comprised of 10 bilayers. [b] Integrated areas are corrected for instrumental and atomic sensitivity factors. The following photoelectron peaks were used: P_{2p} (134.5 eV), $Cd_{3d5/2}$ (406.7 eV), $Mn_{2p3/2}$ (643.1eV), Zr_{3d} (185.9 and 183.6 eV). [c] Calculated bilayer thicknesses are determined from IR data as described in the text. [d] Values are calculated using the metal:phosphorus stoichiometry of the analogous solid state metal phosphonate compound $Zr(O_3PR)_2$ and $M^{II}(O_3PR)H_2O$ M = Mn and Cd. [e] Ratios of phosphorus and metal in the LB film are determined from comparison of the observed and calculated relative percentages of the phosphorus and metal XPS signals.

for differences in the photoelectron escape depths.[99,117,118] Here corrections for the photoelectron escape depths are necessary since the energies of the P_{2p} and metal ion photoelectrons differ greatly. A sample calculation is presented in Appendix-A. The close agreement between the observed relative percentages and the calculated percentages indicates a phosphorus:metal stoichiometry of 1:1 in the M^{II}-P4 LB films, and this ratio is consistent with the structure of the solid-state compounds of formula $M^{II}(O_3PR)H_2O$.

The XPS results of a single bilayer and a three bilayer 'Mn'-P0 films show that within experimental uncertainties (±3%) there are no Mn ions incorporated into the sample using the deposition conditions presented in Table 3-1.

X-ray Diffraction Measurements

X-ray diffraction (XRD) measurements are used to demonstrate the layered nature of the films. Typically 10 - 20 bilayers are deposited for XRD studies and usually 3 - 7 orders of the (0 0 l) Bragg reflections can be detected. The bilayer thicknesses are determined from the (0 0 l) reflections.

XRD: zirconium phosphonate LB films

XRD results of each Zr phosphonate film show that these films possess a layered structure. All zirconium phosphonate LB samples studied contained ten bilayers of deposited materials. On average 3 or 4 orders of (0 0 l) Bragg reflections are observed for each sample, and the bilayer thickness of each film, determined from these reflections, is reported in Table 3-3. A representative XRD pattern is shown in Figure 3-10 for a 10-bilayer P0-Zr-ODP LB film. The P0-Zr-ODP and P4-Zr-ODP films have similar bilayer thicknesses of 53 ± 1 Å and 52 ± 1 Å, respectively, and the P4-Zr-P4 film is found to have a bilayer thickness of 56 ± 1 Å.

XRD: manganese and cadmium phosphonate LB films

XRD measurements show that each of the M^{II}-P4 films is layered. Four orders of (0 0 l) Bragg reflections (l = 2 - 5) are observed for both M^{II}-P4 samples, where each sample consists of 10 bilayers. A bilayer thickness of 50 ± 1 Å is found for both M^{II}-P4 LB films. XRD measurements on a 10-bilayer 'Mn'-P0 film indicates that the sample is layered with a bilayer thickness of 56 ± 1 Å. The X-ray reflections from the 'Mn'-P0 film are considerably weaker than those of the Mn-P4 film, presumably from the absence of the metal phosphonate lattice (as evidenced from XPS measurements). Interestingly, even though the P0 and P4 compounds have the same size (i.e., P0 contains the same number of methylene groups as P4 and should be the same size), the P0 film is thicker than the corresponding P4 film which indicates a difference in molecular packing of these two amphiphiles.

Infrared Spectroscopy Measurements

For all metal organophosphonate LB films studied, ATR-FTIR spectroscopy is used to evaluate the degree of crystallinity and order of the transferred assemblies. The position and shape of the aliphatic CH stretching modes in the IR spectra of monolayer and multilayer films reflect the conformational order and packing of the aliphatic chains. In particular, the frequency of $v_a(CH_2)$ reflects the conformational order of the alkyl chains, and the full-width-at-half-maximum (fwhm) of this vibrational mode is a measure of the degree to which the alkyl chains are closed packed.[84,119,120] Polarized ATR-FTIR experiments are used to determine the tilt angles of the molecular axes of the alkyl chains and phenoxy moieties.[132,136]

In addition, since the absorbance intensity of any IR mode is proportional to the concentration of the material, infrared studies as a function of the number of deposited bilayers are used to assess the integrity of the multilayer assemblies. The results for the zirconium and divalent metal films are discussed in greater detail below.
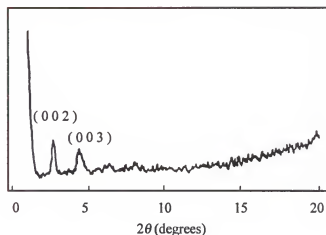
Figure 3-10. XRD pattern from a 10 bilayer P0-Zr-ODP LB film.

IR: zirconium phosphonate LB films

To investigate the organization of the organophosphonate groups in the zirconium phosphonate films shown in Figure 3-3, ATR-FTIR spectra were obtained of the zirconated template monolayers, of the subsequent capping monolayers, and of the symmetric P4-Zr-P4 films. For studies of monolayer films, ATR-FTIR scans were acquired after the second and final steps of the deposition procedure. Spectra of the individual template monolayers and capping monolayers were obtained by ratioing the acquired spectra to the appropriate background. Information regarding the arrangement of the aryl moieties was obtained through analysis of spectra of multilayer samples.

Template layers. It has previously been shown that zirconated template layers of ODP display the organized structure necessary for constructing stable, well-organized multilayer films.[5,6] Successful transfers of P4 on the deposition down-stroke results in a new template layer that may be compared with the zirconated ODP template. Figure 3-11 compares ATR-FTIR

spectra from 2700 to 3100 cm^{-1} of zirconated template monolayers of ODP and P4. In both spectra three C-H stretching bands are resolved corresponding to the asymmetric methyl stretch ($v_a(CH_3)$) at 2953 cm^{-1}, the asymmetric methylene stretch ($v_a(CH_2)$) at 2918 cm^{-1}, and the symmetric methylene stretch ($v_s(CH_2)$) at 2850 cm^{-1}. In the spectra shown in Figure 3-11, the peak position of the asymmetric methylene vibration indicates that both template layers possess alkyl chains arranged in an all-trans conformation. For the zirconated ODP template, where the alkyl chains have previously been shown to be close-packed, the fwhm of $v_a(CH_2)$ is 20 cm^{-1}. In contrast, the fwhm values for the zirconated P4 template is 27 cm^{-1}. The bands are broadened in the P4 monolayer spectra because they contain contributions from both the fourteen-carbon and four-carbon segments.

To differentiate the signals originating from the fourteen-carbon and four-carbon segments in the zirconated P4 template monolayer, ATR-FTIR spectra were taken of zirconated dP4 template monolayers (where the fourteen-carbon chain was perdeuterated). To determine how the C-D stretching modes shift as a function of the organizational state of the molecule, spectra were taken of dP4 in a liquid-like state in CHCl$_3$ solution and as a solid (KBr pellet). Spectra showing the C-D stretches of dP4 are provided in Figure 3-12. The spectrum of the solution sample of dP4 has the asymmetric methylene stretch ($v_a(CD_2)$) at 2198 cm^{-1} and the symmetric methylene stretch ($v_s(CD_2)$) at 2096 cm^{-1}. This is in contrast to the $v_a(CD_2)$ and $v_s(CD_2)$ positions in the spectrum of the solid at 2193 and 2089 cm^{-1}, respectively. The asymmetric CD$_2$ stretch also has a large fwhm of 35 cm^{-1} in the solution spectrum as opposed to the 20 cm^{-1} value for that of the solid. Figure 3-12 also shows the C-D stretch region of a zirconated dP4 template monolayer where the $v_a(CD_2)$ and $v_s(CD_2)$ bands appear at 2195 cm^{-1} and 2090 cm^{-1}, respectively. The bands are narrow, with a fwhm of 20 cm^{-1}, and appear essentially identical to the solid-state KBr spectra of dP4 shown in this same figure. This result
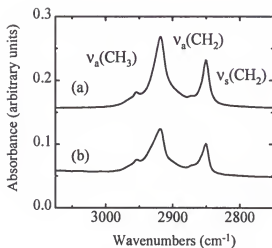
Figure 3-11. ATR-FTIR spectra of (a) a zirconated ODP template monolayer and (b) a zirconated P4 template monolayer. Spectra are vertically offset for clarity.
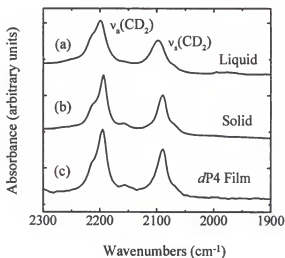
Figure 3-12. FTIR spectra of (a) a chloroform solution of dP4, (b) a KBr pellet of dP4 and (c) and an ATR-FTIR spectrum of a zirconated dP4 template monolayer. Spectra are scaled to similar intentsity and are vertically offset for clarity.

indicates that the fourteen-carbon alkyl chains in the zirconated dP4 template monolayer are well-organized and are arranged in an all-trans conformation, suggesting that the broadened $\nu_a(CH_2)$ stretch observed in the spectra of the non-deuterated zirconated P4 template layer (Figure 3-11) does not result from any disorder in the fourteen-carbon segment.

Inspection of the C-H modes resulting from the four-carbon segment in monolayer spectra of the zirconated dP4 templates reveals that the spectra closely resemble the C-H stretching modes observed in a solid-state spectrum of butylphosphonic acid, where individual CH_2 units can be distinguished. The four-carbon segment, therefore, is responsible for the broad C-H stretch modes in the spectra of undeuterated templates of P4. Although there is a resemblance to the KBr spectrum of butylphosphonic acid, it is not possible to determine how the four-carbon chains in this template are organized.

The tilt angles of the alkyl chains with respect to the surface normal in the zirconated ODP and dP4 template monolayers can be determined from polarized ATR-FTIR experiments. Detailed accounts of the procedure have been described by other researchers. .[132,136] A dichroic ratio, defined as

$$D = (A_x + A_z) / A_y, \tag{3-1}$$

where $(A_x + A_z)$ is the absorbance with p-polarized light and A_y is the absorbance with s-polarized light, can be calculated from ratios of the absorbance intensity of a given IR mode with light polarized parallel and perpendicular to the film surface. For the methylene vibrations, the CH_2 dipole moment is oriented 90° with respect to the alkyl chain axis. By taking the ratio of the absorbance intensities of $\nu_a(CH_2)$ and $\nu_s(CH_2)$ with p-polarized light to the intensities with s-polarized light and by noting the relationship between the CH_2 dipole moment and the molecular axis, it is possible to determine the angle that the alkyl chains make with respect to the surface normal. Measured dichroic ratios and calculated tilt angles for the eighteen-carbon chains in the zirconated ODP monolayers and for the fourteen-carbon chains in zirconated dP4 template

monolayers are given in Table 3-3. On average, the tilt angle for the eighteen-carbon segment in the zirconated ODP template is 30°, which correlates well with the tilt required to achieve close-packing of the alkyl chains given the constraints of the PO_3^{2-} head-group (24 Å^2 MMA at deposition opposed to 20 Å^2 for the cross-sectional area of the all-trans alkyl chain). For the zirconated template of dP4, the tilt angle of the fourteen-carbon segment is 46°. The larger alkyl chain tilt angle of dP4 relative to the ODP template arises from a greater spacing between molecules because of the larger MMA (27 Å^2 at transfer) imposed by the aryl groups. The larger distance between molecules requires the chains to tilt more to maximize van der Waals interactions.

Capping layers: P0 on a zirconated ODP template. Although quality template monolayers of P0 could not be transferred, monolayer films of this material can be successfully transferred as capping layers onto zirconated ODP templates. The organization of the alkyl chains and aryl groups in the P0 capping monolayer is determined from non-polarized and polarized IR data. Figure 3-13 shows a non-polarized ATR-FTIR spectrum of a capping monolayer of P0 deposited onto a zirconated ODP template. In this spectrum the asymmetric methylene vibration, $v_a(CH_2)$, occurs at 2918 cm^{-1}, indicating that the eighteen-carbon alkyl chains are arranged in an all-trans conformation. The fwhm value of the asymmetric methylene vibration is 20 cm^{-1}, indicating that the alkyl chains are close-packed.

Tilt angles of the phenoxy group in capping monolayers of P0 on zirconated ODP templates are determined from IR modes corresponding to the C=C skeletal deformations of the aryl group. The C=C skeletal deformation modes 8a and 19a for para-substituted benzene rings are typically found in the regions of 1570-1628 cm^{-1} and 1460-1530 cm^{-1}, respectively. Assuming $C2_v$ symmetry for the phenoxy group, these modes have their net transition dipole moments located along the C_1-C_4 axis of the aryl group.[132,137] The intensities of these modes in spectra of single monolayers of P0 are weak, which makes quantitative analysis of these bands difficult.

Table 3-3. Dichroic Ratios,[a] of Alkyl and Phenyl IR Modes and the Corresponding Molecular Axis[b] Tilt Angle for Zirconated Template and Capping Monolayers of Phenoxy Substituted Organophosphonate LB Films.

Film	Mode	Wavenumber (cm^{-1})	Dichroic Ratio D	Tilt Angle (deg)
template monolayer				
ODP	$\nu_a(CH_2)$	2918	1.04 ± 0.02	30 ± 2
	$\nu_s(CH_2)$	2850	1.04 ± 0.01	30 ± 1
dP4	$\nu_a(CD_2)$	2195	NA^c	NA^c
	$\nu_s(CD_2)$	2090	1.28 ± 0.03	46 ± 2
	C = C (8a)	1612	NA^d	NA^d
	C = C (19a)	1514	3.4 ± 0.1	20 ± 1^e
capping monolayer (on ODP)				
P0	$\nu_a(CH_2)$	2918	1.09 ± 0.02	35 ± 2
	$\nu_s(CH_2)$	2850	1.12 ± 0.02	37 ± 2
	C = C (8a)	1603	2.9 ± 0.1	22 ± 1
	C = C (19a)	1504	2.9 ± 0.1	22 ± 1
dP4	$\nu_a(CD_2)$	2195	NA^c	NA^c
	$\nu_s(CD_2)$	2090	1.12 ± 0.03	37 ± 2
	C = C (8a)	1612	NA^d	NA^d
	C = C (19a)	1514	2.8 ± 0.1	23 ± 1
capping monolayer (on P4)				
dP4	$\nu_a(CD_2)$	2195	NA^c	NA^c
	$\nu_s(CD_2)$	2090	1.19 ± 0.02	42 ± 2
	C = C (8a)	1612	NA^d	NA^d
	C = C (19a)	1514	3.4 ± 0.1	20 ± 1^e

[a] The dichroic ratio, D, is defined as $(A_x + A_z)/(A_y)$. [b] Molecular axes are defined along the C_1-C_4 axis for the phenyl moiety and at 90° to the methylene C-H bonds for the alkyl chains. [c] Tilt angles of the fourteen-carbon chains are calculated from the symmetric methylene stretch only. [d] Only mode 19a was used to determine the tilt of the phenyl ring in monolayers of dP4. [e] The tilt angle of the phenyl ring is reported as the average over the template and capping layers because these values were determined from multilayer samples of P4-Zr-P4.
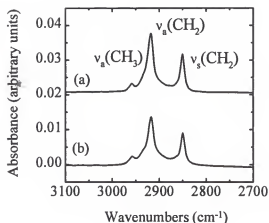
Figure 3-13. ATR-FTIR spectra of capping monolayers of (a) P0 and (b) P4 where each is deposited onto a zirconated ODP template. Spectra are vertically offset for clarity.
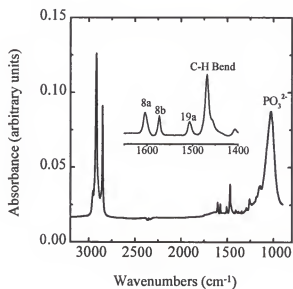
Figure 3-14. ATR-FTIR spectrum of a five-bilayer P0-Zr-ODP LB film. The inset shows an enlarged region containing the aryl C=C skeletal deformation modes.
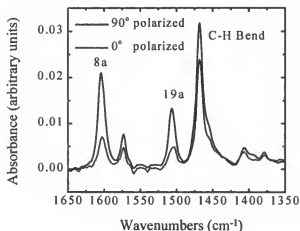
Figure 3-15. Polarized ATR-FTIR spectra of a five-bilayer P0-Zr-ODP LB film. Spectra were taken at 90° and 0° polarizations and show the difference in the absorbance intensities of the aryl C=C skeletal deformation modes for the two polarizations.

To enhance the intensity of these modes, multilayer samples (5-20 bilayers) were used for polarized IR experiments. No structural differences in the early layers as compared to the top layers are observed. Figure 3-14 shows a non-polarized ATR-FTIR spectrum of a five-bilayer P0-Zr-ODP sample. The inset in the figure shows the C=C skeletal deformation modes, labeled 8a and 19a, and occurring at 1603 cm^{-1} and 1504 cm^{-1}, respectively. Since no bands originating from the zirconated ODP template monolayer overlapped with modes 8a or 19a, it is possible to use multilayer samples for the measurement of the dichroic ratios for these IR modes. The peak at 1467 cm^{-1} is the alkyl C-H bend mode that contains contributions from both the template and capping monolayers, but its position does not distort the aryl modes.

Figure 3-15 shows the ATR-FTIR spectra taken in two polarizations of a 15 bilayer sample of P0-Zr-ODP and demonstrates how the intensities of modes 8a and 19a change as a function of polarization. The measured dichroic ratios and calculated tilt angles for the phenoxy moiety are summarized in Table 3-3. These values were determined from samples consisting of 5, 10, and 15 bilayers of P0-Zr-ODP. The measured values do not change as the number of

bilayers is increased, and the numbers reported in Table 3-3 are an average of the samples with different numbers of bilayers. Since the transition dipole moment of both skeletal modes is oriented along the same direction,[137] either or both of these modes can be used to calculate the tilt angles of the phenoxy moiety, and both modes provide a tilt angle of 22°.

Capping layers: P4 on a zirconated ODP template. An IR spectrum showing the C-H stretch bands of a capping monolayer of P4 on a zirconated ODP template is shown in Figure 3-13. The asymmetric methylene stretch is broadened in the spectrum because contributions from both the four-carbon and fourteen-carbon segments overlap in this signal. The peak position of the $v_a(CH_2)$ at 2918 cm^{-1} indicates that there are alkyl chain segments that possess an all-trans conformation. More information can be extracted from a spectrum of dP4 as a capping monolayer. The C-D stretch region of a capping monolayer of dP4 on a zirconated ODP template is identical to the C-D stretch region of the zirconated dP4 template monlayer, shown in Figure 3-12. In both of these IR spectra, the C-D peak positions of $v_a(CD_2)$ and $v_s(CD_2)$ appear at 2195 cm^{-1} and 2090 cm^{-1}, respectively, and are nearly identical to those in the spectrum of solid dP4. These positions indicate that the fourteen-carbon alkyl chains are in an all-trans conformation. The narrow fwhm values for the asymmetric methylene vibration of 20 cm^{-1} suggest that the long alkyl chains are close-packed in the films. Table 3-3 reports the measured dichroic ratios and calculated tilt angles for the fourteen-carbon alkyl chains in dP4. From tilt angle analysis of the symmetric methylene vibration, it is found that the fourteen-carbon segments tilt an average of 37°. This value is similar to the tilt angle for the eighteen-carbon chain in the P0 capping monolayer in the P0-Zr-ODP films.

The tilts of the phenoxy moieties were determined from 5, 10, and 15 bilayer samples of dP4-Zr-ODP, and Figure 3-16 shows a non-polarized ATR-FTIR spectrum of a 5-bilayer sample. The inset in this figure shows the C=C skeletal deformations with modes 8a and 19a labeled at 1612 cm^{-1} and 1514 cm^{-1}, respectively. Mode 19a is used to determine the tilt from the surface

normal of 23° for the phenoxy group. The reported tilt angle (Table 3-3) is an average of all the samples studied and its value does not change as the number of bilayers increases.

Symmetric bilayers of P4. Again, the organization of the different alkyl chain segments can be analyzed by studying the partially deuterated molecules in films. The tilt angle of the fourteen-carbon segments in capping monolayers of *d*P4 in the symmetric bilayers is determined from monolayer spectra and is reported in Table 3-3. The tilt angle of the phenoxy group in the symmetric P4-Zr-P4 bilayers is also reported in Table 3-3. However, for the symmetric films it is not possible to distinguish the phenoxy moiety in the templates from those in the capping layers, and the phenoxy tilt angle listed for these bilayers are an average over both the template and capping layers. Polarized IR analysis of the 19a mode for the P4-Zr-P4 symmetric films yielded a tilt angle of 20° for the phenoxy group.

There are slight differences between the organization of the *d*P4 capping layers in the symmetric bilayers relative to their organization when deposited onto zirconated ODP templates. Since the deposition conditions for the capping layers are identical on both templates, the organization of the template must influence the subsequent organization of the capping layer. The largest effect is seen in the four-carbon segment. The $v_a(CH_2)$ band is much narrower for the capping layer on the OPA template than on a *d*P4 template suggesting a more uniform arrangement of the four-carbon segment in the alternating layer film. As discussed above, the four-carbon chains in the templates of *d*P4 appear to be randomly ordered. Disorder among the phosphonate head groups in the template directly affects the order in the zirconium layer. When the capping layer is deposited onto an organized zirconium phosphonate surface, as in the zirconated ODP template, the arrangement of the four-carbon segment is more uniform than when the same capping layer is deposited onto the less-organized zirconium phosphonate surface provided by the P4 template. The more uniform zirconium phosphonate surface of the zirconated ODP template leads to better-organized capping layers even though the P4 capping layer is incommensurate with the ODP template layers.
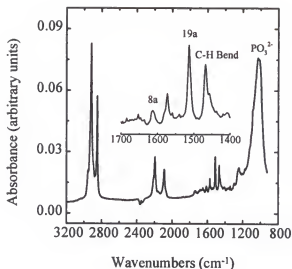
Figure 3-16. ATR-FTIR spectrum of a five-bilayer dP4-Zr-ODP LB film. The inset shows an enlarged region containing the aryl C=C skeletal deformation modes.

Because the zirconium/phosphonate binding interaction is strong, the inorganic layer is not expected to be highly crystalline (the crystallinity of solid-state zirconium phosphonates and phosphates is generally quite poor), so epitaxy between the capping and template layers is not necessary for good film transfer. The orientation and intermolecular packing of the aryl and fourteen-carbon segments in dP4 show only slight differences when transferred onto both templates, indicating that these segments are less influenced by the organization of the zirconated surface. The four-carbon segment buffers the rest of the molecule from the inorganic network, and the packing of the aryl and fourteen-carbon chain groups is determined by intermolecular forces and not by interactions with the surface.

IR: manganese and cadmium phosphonate LB films

M^{II}-P4 films. Figure 3-17 shows ATR-FTIR spectra from 4000 cm^{-1} to 950 cm^{-1} of 10-bilayer samples of both Mn-P4 and the partially deuterated Mn-dP4 with labeled peaks

corresponding to the asymmetric methylene ($v_a(CH_2)$ and $v_a(CD_2)$), symmetric methylene ($v_s(CH_2)$ and $v_s(CD_2)$) stretching vibrations and the 19a C=C skeletal deformation. The spectrum in Figure 3-17 of Mn-dP4 allows the signals arising from the separate 4-carbon and 14-carbon segments to be differentiated (where the 14-carbon segment is perdeuterated). The $v_a(CD_2)$ and $v_s(CD_2)$ stretches occur at 2193 cm^{-1} and 2090 cm^{-1}, respectively, for both the Mn- and Cd-dP4 LB films. The bands are narrow with fwhm values of 20 cm^{-1}. The frequency and shape of the bands are similar to those observed in spectra of a KBr pellet of dP4A (Figure 3-12) and reflect that the 14-carbon chains are closed-packed and arranged in an all-trans conformation.

It has been previously shown that the phosphonate (P=O) infrared stretching modes can be used to correlate the metal-phosphonate continuous lattice structures of LB films with those of the solid-state structures.[10] The P=O stretching frequencies are very sensitive to the mode of metal bonding, and the different metal phosphonate structure types give distinct P=O stretching patterns in their IR spectra.[123] Figure 3-18 shows the asymmetric phosphonate ($v_a(PO_3^{2-})$) and symmetric phosphonate ($v_s(PO_3^{2-})$) stretches, occurring at 1083.9 and 978.8 cm^{-1} for the Mn-P4 LB film and at 1084.9 and 958.6 cm^{-1} for the Cd-P4 film, respectively. The shape, relative intensity, and frequency of these modes are almost identical to those of $Mn(O_3PC_2H_4)H_2O$ and $Cd(O_3PC_2H_4)H_2O$ solid-state samples (Table 3-4). This similarity indicates that the M^{II}-P4 LB films contain the same 2D metal phosphonate continuous lattice of the analogous $M(O_3PR)H_2O$ solid-state compounds. In addition, the IR mode at 1610 cm^{-1} in the spectra of both films corresponds to the H-O-H bending mode of the coordinated water molecule present in the $M(O_3PR)H_2O$ structure, which also occurs at 1610 cm^{-1} in spectra of the solids.

The deposition of the Mn-P4 film was followed by IR measurements as a function of the number of deposited bilayers. A linear increase in the intensity of the $v_a(CH_2)$ and the 19a modes as a function of the number of bilayers deposited (Figure 3-19A) shows that the same amount of P4 is transferred during each deposition cycle. In addition, a linear increase in the intensity of the
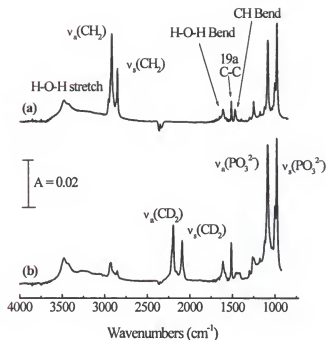
Figure 3-17. ATR-FTIR spectra of 5 bilayers of (a) Mn-P4 and (b) Mn-*d*P4 showing the IR modes originating from the separate hydrogenated 4-carbon and perdeuterated 14-carbon segments.
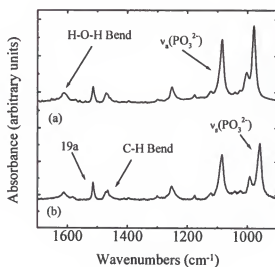
Figure 3-18. ATR-FTIR spectra of 5 bilayers of (a) Mn-P4 and (b) Cd-P4 LB films.
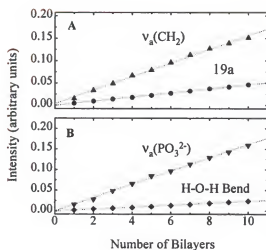
Figure 3-19. Integrated intensity of **(A)** the $v_a(CH_3)$ and 19a FTIR absorptions and **(B)** the $v_a(PO_3^{2-})$ and H-O-H bend FTIR absorptions as a function of the number of bilayers of the Mn-P4 LB film. A linear relationship in **(A)** shows that the same amount of film transfers during each deposition while in **(B)** it indicates that the metal phosphonate structure is formed and maintained throughout the repeated deposition procedure.

Table 3-4. Phosphonate Stretching Frequencies of Divalent Metal Alkylphosphonate Powders[a] and M[II]-P4 LB Films[b].

sample	$v_a(PO_3^{2-})$ (cm^{-1})	$v_s(PO_3^{2-})$ (cm^{-1})
Mn-P4 LB Film	1086	979
$Mn(O_3PC_2H_5)H_2O$ Powder	1087	988 / 964
Cd-P4 LB Film	1087	959
$Cd(O_3PC_2H_5)H_2O$ Powder	1089	957

[a] Powder samples were measured as KBr pellets. [b] LB films were deposited onto Ge ATR crystals for IR measurements.

$v_a(PO_3^{2-})$ mode and the H-O-H bending mode (Figure 3-19**B**) shows that the metal phosphonate continuous lattice structure is maintained in the multilayer films.

The tilt angles of the 14-carbon chain axes and of the phenoxy moieties in M^{II}-*d*P4 LB films are determined from polarized ATR-FTIR experiments. The dichroic ratios, (defined above) of the $v_a(CD_2)$ stretching vibration and 19a C-C skeletal deformation, as well as the corresponding tilt angles are listed in Table 3-5. For each M^{II}-P4 film, the phenoxy moiety is tilted at an angle of $23 \pm 2°$ from the surface normal. The measured dichroic ratios of the $v_a(CD_2)$ for both the Mn- and Cd-*d*P4 films correspond to a tilt angle of $47 \pm 3°$ from the surface normal for the 14-carbon chain.

'Mn'-P0 films. Figure 3-20 shows the infrared spectrum of a one-bilayer 'Mn'-P0 LB film. Peaks at 1506, 1574 and 1603 cm^{-1} are the 8a, 8b, and 19b C=C skeletal deformations. The intensity of these modes including that of the asymmetric methylene vibration at 2918 cm^{-1} indicates that a complete bilayer of the organophosphonate material has transferred. However, the broad peak between 1200 and 900 cm^{-1} corresponds to an amorphous phosphonate head group arrangement[123] and indicates that the metal phosphonate lattice has not formed within the polar region of this film. This result is consistent with those of XPS measurements that show that almost no manganese is incorporated into the films under these transfer conditions.

Structural Analysis

The tilt angles determined from polarized IR experiments can be used to estimate the bilayer thickness of each film, which can then be compared to the bilayer thickness determined from XRD measurements. To calculate the length of each molecule, the following distances were used: 1.2 Å for the length of each CH_2-CH_2 unit on an all-trans alkyl chain,[132] 1.2 Å for the C(alkyl)-O bond length,[132] 5.4 Å for the phenoxy moiety,[132] 3 Å for the van der Waals gap between the adjacent tails in the bilayer,[40] and 4.5 Å for the P – O – M – O - P distance[16,32] and
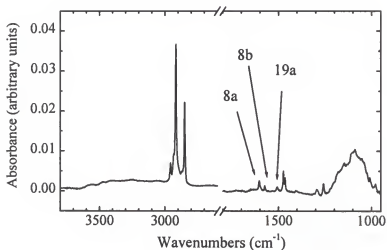
Figure 3-20. ATR-FTIR spectrum of a one-bilayer 'Mn'-P0 LB film.

Table 3-5. Dichroic Ratios[a], D, and Corresponding Molecular Axis[b] Tilt Angles for M^{II}-P4 LB Films.

sample	mode	freq (cm^{-1})	D	tilt angle (deg)
Mn-P4	$\nu_a(CH_2)$	2193	1.30 ± 0.05	48 ± 4
	C = C 19a	1515	2.6 ± 0.1	24 ± 2
Cd-P4	$\nu_a(CH_2)$	2193	1.33 ± 0.05	48 ± 4
	C = C 19a	1515	2.7 ± 0.1	23 ± 2

[a] Dichroic ratio, D, is defined as $(A_x + A_z)/(A_y)$. [b] Molecular axes are defined along the C_1-C_4 axis of the phenoxy moiety and at 90° to the methylene bonds for the alkyl-chains. Tilt angles are defined with respect to the film normal (0°).

the P-O-Zr-O-P distance is assumed to be 4.4 Å which is the distance observed in crystalline samples of zirconium phenylphosphonates.[43] The calculated thickness of 51 ± 2 Å for the P0-Zr-ODP LB film is in excellent agreement with the measured interlayer distance (Table 3-2). For films containing P4, the calculated distances are reported as a range because the tilt angle of the 4-carbon segment is unknown and disorder is expected. The range includes those values obtained when the 4-carbon segment has its maximum length (tilt angle of $0°$) and when it is oriented at a tilt angle equal to that of the 14-carbon segment. For the M^{II}-P4 films, the calculated range of 48 - 53 Å corresponds well with the bilayer thickness of 50 ± 1 Å determined from XRD measurements. For the P4-Zr-ODP and P4-Zr-P4 films, the calculated ranges were also in close agreement to those values determined form XRD measurements (Table 3-2).

Magnetic Properties of Mn-P4 Films

EPR measurements were made on a 52-bilayer Mn-P4 LB film sample that was cut into thin strips, stacked, and placed vertically into a conventional EPR tube such that the LB plane could be rotated with respect to the applied magnetic field. The inset in Figure 3-21 shows a representative EPR signal from the Mn-P4 LB film. The signal is dipolar broadened, characteristic of an exchange-coupled lattice, and no hyperfine Mn^{2+} splittings are observed. Figure 3-21 shows the peak-to-peak line width, ΔH_{p-p}, of the EPR signal at room temperature as a function of orientation. (*Note*: The LB film sample has a common axis normal to the surface since the layers are deposited parallel to the substrate, but the in-plane direction consists of a distribution of circularly averaged domains.) The direction normal to the LB planes is defined as $0°$. The line width has a maximum value of 264 G at $0°$ and $180°$ with a minimum value of 208 G at $55°$ and $125°$. Within experimental error, the value of the g-factor does not change as a function of orientation and is consistently found to be 1.99 ± 0.02. The data in Figure 3-21 are fit with the expression, $\Delta H_{p-p} = A + B(3\cos^2\phi - 1)^2$, which is characteristic of a 2D spin system with

antiferromagnetic Heisenberg exchange.[9,138] The fit yields values of $A = 208$ and $B = 16$, where A and B encompass contributions to the line width from both exchange and dipolar interactions.[138] The important result from Figure 3-21 is the observation of magnetic exchange within the 2D layers.

The peak-to-peak line width as a function of temperature for a sample that is aligned perpendicular to the magnetic field is shown in Figure 3-22. The line width is nearly constant as the temperature is lowered until a significant broadening occurs below 50 K. From $50 - 18$ K, the line width increases rapidly until the signal becomes so broad that it can no longer be detected. This broadening also occurs in the EPR signals of both the Mn-ODP LB film and the solid-state powdered manganese alkylphosphonates,[9] and results from antiferromagnetic fluctuations that signal an approaching magnetic ordering transition.[139] The magnetic resonance signals from the ordered state (the antiferromagnetic resonances[139]) are not observed because, for the manganese phosphonates, they occur outside the frequency and field range accessible by an X-band EPR spectrometer.[140]

The integrated area of an isotropic Lorentzian signal is proportional to the spin susceptibility,[138] and a plot of the area of the EPR signal as a function of temperature is shown in Figure 3-23. The solid line is a fit of the data using a series expansion solution for a 2D quadratic lattice of $S = 5/2$ spins with Heisenberg nearest-neighbor exchange.[78] The fit further illustrates that at high temperatures the magnetic exchange exists within the layers of manganese ions and that the exchange interaction is isotropic. The strength of the magnetic interaction is given by the value of the exchange constant, $J = -2.7 \pm 0.1$ K, which was determined from this fit. An estimate of J can also be determined from the temperature of the susceptibility maximum[49] by $kT\chi_{max}/J = 2.05S(S + 1)$. From Figure 3-23, $T\chi_{max}$ occurs at 25 K leading to a value of $J = -2.8 \pm 0.1$ K, which is in close agreement with the value obtained from fitting the temperature dependent data. The data can also be viewed as a Curie-Weiss plot, and the inset in Figure 3-23 shows a plot of
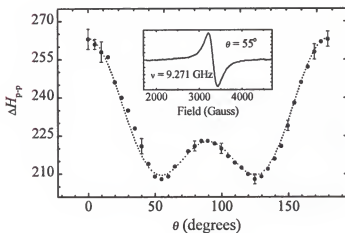
Figure 3-21. Room temperature EPR line width as a function of orientation for a 52 bilayer Mn-P4 LB film. The dotted line is a fit to the data and is discussed in the text. The direction normal to the LB planes is defined as 0°. The inset shows, as an example, the EPR signal at $\theta = 55^\circ$.
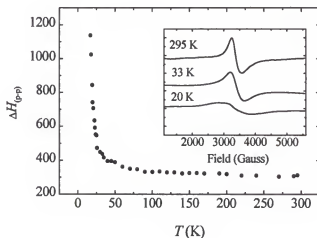
Figure 3-22. EPR line width as a function of temperature for the Mn-P4 LB film oriented 0° with respect to the magnetic field. The experimental uncertainties are given by the size of the data points. The inset gives examples of the EPR signal at 295, 33 and 20 K. The significant broadening of the line width below 50 K is characteristic of an approaching magnetic ordering transition.

1/area vs. temperature, where with the x-axis intercept of $-58 \pm 2°$ provides a value for the Weiss constant, θ. The magnetic exchange parameters of J and θ of the Mn-P4 LB film are similar in value to those of the bulk phosphonate solids,[22,23] adding further evidence that the in-plane Mn-O-Mn interactions are the same as those of the solid state materials.

Although the magnetically ordered state cannot be probed by X-band EPR spectroscopy, evidence for an ordered state is observed in magnetometry measurements. The analogous solid-state metal phosphonates are known to undergo transitions to an ordered state with a weak ferromagnetic moment due to incomplete cancellation of the spins that results from canting of the antiferromagnetically coupled sublattice moments.[22,53] Such systems are referred to as canted antiferromagnets or weak ferromagnets.[49] An up-turn in the temperature-dependent magnetic susceptibility observed at $T < T_{\chi max}$ is a signature of canted antiferromagnetic ordering,[49,141] with T_N being the temperature at which the up-turn occurs. For such materials, a non-zero magnetization, or weak ferromagnetic moment, can be observed at temperatures below T_N in difference plots of the field-cooled (FC) and zero field-cooled (ZFC) temperature-dependent magnetization, ΔM_{FC-ZFC}. Figure 3-24 shows a plot of ΔM_{FC-ZFC} vs. temperature for the Mn-P4 film oriented with the planes parallel to the applied magnetic field. The significantly large ΔM below T_N is evidence for a transition to long-range magnetic order with spontaneous magnetization and is consistent with a transition to a canted antiferromagnetic state. The ZFC data (Figure 3-25) show that the film orders at 14.8 ± 0.2 K. The net moment is larger in the parallel orientation, indicating that the magnetic easy-axis is perpendicular to the metal plane and that the canted moment lies within the metal planes. The non-zero magnetization perpendicular to the metal planes can arise from imperfect alignment of the sample or from uncompensated spins at the magnetic domain boundaries. A spin-flop[49] transition transition near 2.5 T is observed in the magnetization versus field data when the applied field is perpendicular to the metal planes, further indicating that the magnetic easy-axis lies normal to the film surface. These
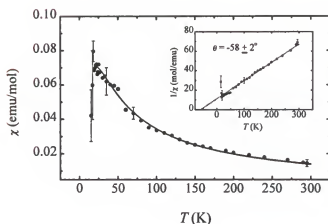
Figure 3-23. Temperature dependence of the integrated area (normalized to the room temperature spin-only susceptibility value) of the EPR signal of the Mn-P4 LB film. The solid line is a fit to the data using a model described in the text for a two-dimensional lattice of Mn^{II} $S = 5/2$ ions with Heisenberg antiferromagnetic exchange with exchange constant $J = -2.7$ K. The inset shows a plot of the inverse area vs. temperature with the solid line as a fit to the Curie-Weiss law for $T > 80$ K, and extrapolation gives an intercept, $\theta = -58$ K which indicates antiferromagnetic exchange.
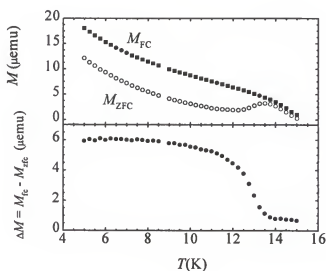
Figure 3-24. Magnetization vs. temperature for the 52 bilayer Mn-P4 LB film with measuring field applied parallel to the plane of the film. (A) Comparison of the magnetization data taken upon warming the film after cooling in zero-applied field (M_{ZFC}) and cooling in a field of 0.1 T (M_{FC}). In both cases, the measuring field is 0.01 T. (B) The difference in the FC and ZFC magnetization, ΔM_{FC-ZFC}, showing spontaneous magnetization below T_N.
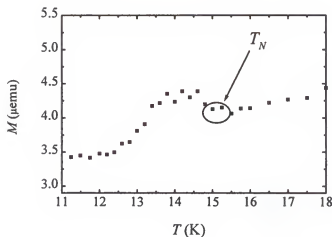
Figure 3-25. Zero-field cooled magnetization data, M_{ZFC}, for the Mn-P4 LB film oriented perpendicular to the LB planes. The ordering temperature, $T_N = 14.8 \pm 0.01$ K, is indicated by an up-turn in the data which is characteristic of canted antiferromagnetic ordering.

findings are consistent with the spin arrangement found for the Mn-ODP LB film[10] and for the analogous manganese phosphonate solid compounds.[22,53]

The Mn-P4 film is the second example of a magnetic LB film that contains the manganese phosphonate lattice structure and exhibits spontaneous magnetization. The magnetometry measurements show that the Mn-P4 film orders to a canted antiferromagnetic state and that the phenoxy moieties do not disrupt the Mn-O-Mn exchange pathways of the solid-state $Mn(O_3PR)H_2O$ network. Interestingly, the ordering temperature of the Mn-P4 film, $T_N = 14.8 \pm 0.2$ K, is higher than $T_N = 13.8 \pm 0.2$ K determined for the Mn-ODP LB film[10] and is comparable to that of polycrystalline manganese butylphosphonate where $T_N = 15.0 \pm 0.2$ K.[22,23] In the solid-state alkylphosphonates, T_N varies slightly as the alkyl group changes, possibly reflecting subtle changes in the metal-phosphonate bonding geometry.[22] It may be that the 4-carbon tether in P4 results in metal-oxygen-phosphorus bonding more like that found in the short chain alkylphosphonates than in the longer chain analogs such as manganese hexylphosphonate[140] ($T_N = 14.1 \pm 0.2$ K) and the Mn-ODP LB film. Finally, the ordering temperatures permit comment on

the magnetic and therefore, structural coherence lengths in the LB films. For a 2D spin system,[1] the magnetic coherence length diverges as $T \rightarrow T_N$. Diminished coherence lengths, caused by either impurities or small domain sizes, will suppress T_N relative to the infinite solid. The observation that T_N in both the Mn-P4 and Mn-ODP LB films are comparable to solid-state analogs suggests that the ordering temperature is not limited by the size of the domains within the films. Comparison with other 2D magnetic systems[142,143] suggests that the magnetic coherence length is at least 175 Å, providing a lower limit for the size of the structurally coherent domains in the LB films.

Conclusions

Isotherm studies of the P4A and P0A amphiphiles clearly show that the position of the phenoxy group along the alkyl tail affects the quality of the monolayer on the water surface. The position of the aryl group also affects the processibility of the films. It is found that P4A monolayers can be transferred on both the down- and up-stroke from pure water subphases and from 0.5 mM M^{II} subphases adjusted to an appropriate pH range. On the contrary, monolayers of P0A cannot be transferred on the downstroke from pure water subphases, however successful transfer of bilayers of P0A can be achieved from 0.5 mM Mn^{2+} subphase at the appropriate pH range.

The structural characterizations of all films shows that the films are layered and that the organophosphonates in each film are well organized, where in each case the phenoxy moiety is oriented in a vertical manner and tilted approximately 20° from to the surface normal. Because of the nature of the three-step LB/SA procedure used to form the zirconium phosphonate films, these films possess an amorphous 2-dimensional zirconium phosphonate layer. On the other

hand, the M^{II}-P4 (M =Mn, Cd) films contain the crystalline 2D metal phosphonate continuous lattice structure of the analogous solid state materials of formula $M(O_3PR)H_2O$.

The EPR and magnetometry measurements show that the Mn-P4 LB film is the second example of a manganese phosphonate continuous lattice LB film to possess a transition to long-range order. This transition is to a canted antiferromagnetic state with a spontaneous magnetic moment existing for temperatures below 14.8 ± 0.2 K, with the moment aligned perpendicular to the metal planes.

ANTIFERROMAGNETIC RESONANCE AS A TOOL FOR INVESTIGATING
MAGNETOSTRUCTURAL CORRELATIONS: CHARACTERIZATION OF THE CANTED
ANTIFERROMAGNETIC STATE OF A SERIES OF MANGANESE PHOSPHONATES

Introduction

Within the growing fields of magnetochemistry and molecular magnetism there is a strong motivation to have a fundamental understanding of the relationship between chemical structure and magnetic properties of materials.[74] This point is most elegantly demonstrated in various studies of d^9-d^9 Cu(μ-OH)$_2$Cu dimers,[66,68,69] where the magnetic exchange has been shown to correlate with the structure of the copper dimer unit, which includes both the Cu-O-Cu bond angle and the electrostatic properties of the coordinated ligands. The resulting magnetostructural correlations obtained from such studies are often subsequently used as guidelines for the rational design and synthesis of new magnetic materials with tailored physical properties.

The material presented in this chapter demonstrates that antiferromagnetic resonance (AFMR) can be used to probe magnetostructural correlations in a series of related layered antiferromagnets that includes the purely inorganic KMnPO$_4\cdot$H$_2$O, manganese phenylphosphonate (Mn(O$_3$PC$_6$H$_5$)H$_2$O) and four manganese alkylphosphonates (Mn(O$_3$PC$_n$H$_{2n+1}$)H$_2$O n = 3-6). The materials in this series possess nearly isostructural frameworks within the metal-oxygen-phosphorus layers[16,53] allowing for a comparison of how the phosphonate substituents influence the magnetic properties. Correlations are made between the observed magnetic behavior and the electronic structure of the bridging ligand as it changes

from a phosphate to an alkylphosphonate to a phenylphosphonate group. In addition, the AFMR measurements provide a microscopic view of the magnetically ordered states,[139] and measurements of magnetic exchange, magnetic anisotropy, spin-flop and critical fields, and spin canting are quantified for each compound.

Although AFMR is potentially a very powerful tool,[144-146] in the past, studies were restricted to a few materials with small exchange interactions because of limited technology, such as the magnetic field strength and microwave frequencies available with commercial electron paramagnetic resonance (EPR) instruments. [139] However, recent advances in instrumentation development, brought about by the availability of both larger magnetic field strengths and microwave sources ranging up to several hundred GHz, now make possible investigations of a much larger range of antiferromagnetically ordered materials.[147-152]

Currently, neutron diffraction and static magnetometry measurements are commonly used to obtain similar information about the magnetic structure and the spin exchange interactions in the ordered state. AFMR compliments these two techniques, but additionally, it offers some substantial advantages. Unlike neutron diffraction, deuteration of the sample is unnecessary for AFMR, typically 10 - 100 mgs of material affords sufficient signal to noise, and analysis of the data does not involve intensive computational methods. In addition, AFMR provides values of the anisotropy of the magnetic interactions. These values are not always easily determined from static magnetometry measurements, especially from pollycrystalline samples. AFMR can be performed on both powdered samples and single crystals, and when single crystals are available, this technique can be used to assign the relationship between the principal crystallographic axes and the magnetic axes.[153,154] The AFMR method is straight-forward, making it feasible to study a series of materials for the purpose of obtaining magnetostructural comparisons.

Background

Manganese Phosphonates

The metal phosphonates are a class of mixed organic-inorganic layered solids where metal ions, bridged by the phosphonate groups, form sheets that are separated from one another by the organic substituents of the phosphonate ligands. Layered structures are known to form with a variety metal ions and with a range of organophosphonate ligands.[11,12] The ability to pillar and intercalate the layers has stimulated interest in these materials related to uses as catalysts, sorbents and ion-exchangers.[13,155] Metal phosphonates have also attracted the attention of those interested in magnetic interactions in low-dimensional solids,[1,22] partially because of the relationship of layered antiferromagnets to layered superconductors.[151] The metal phosphonates provide a class of layered magnetic materials where magnetic interactions can be varied through changes in either the inorganic or the organic components of the solids.[19,22,48,65]

The structures of the divalent metal organophosphonates (where M^{II} = Mn, Ni, Co, Fe) are analogous to the metal phosphate hydrates, $M^I M^{II} PO_4 \cdot H_2O$ (M^I = K, NH_4; M^{II} = Mn, Ni, Co, Fe), which were reported by Bessett and Baldwell in 1933.[156] The purely inorganic analogs crystallize in the orthorhombic space group $Pmn2_1$, and their structures consist of approximately square planar sheets of M^{II} ions that are coordinated in a severely distorted octahedron by five phosphate oxygens and one water molecule, with the layers separated by the MI ions. The metal organophosphonates have a similar in-plane metal phosphonate extended layer (Figure 4-1) and also crystalize in the $Pmn2_1$ space group, but now the M^{II} planes are separated by the organic pendant groups.

Previously, Carling et al.[22,52,53] have shown, with magnetometry measurements, that the high temperature magnetic properties of $KMnPO_4 \cdot H_2O$ and the manganese alkylphosphonates ($Mn(O_3PC_nH_{2n+1})H_2O$ n = 1-4) are well described by layers of S = 5/2 manganese ions arranged in approximately a 2-dimensional square lattice with Heisenberg antiferromagnetic nearest-neighbor
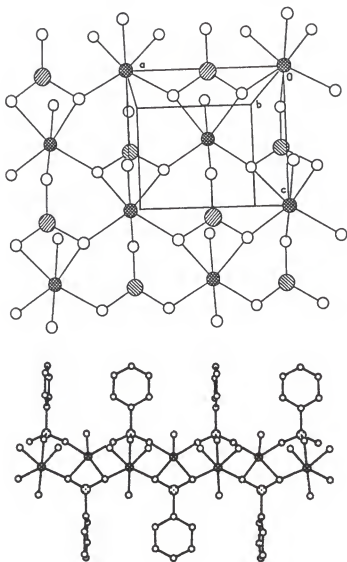
Figure 4-1. In plane and cross-sectional view of $Mn(O_3PC_6H_5)H_2O$. Crystallographic data are taken from ref. 16. Key: oxygen, small open circles; manganese, cross-hatched circles, phosphorus, diagonal-hatched circles (phosphorus atoms above and below the planes are distinguished by hatch marks with different directions).

exchange, and that each material orders antiferromagnetically between 12 and 19 K. Although nearest neighbor exchange is antiferromagnetic, below the ordering temperature the equilibrium distribution of moments is not collinear, but canted from the magnetic easy-axis, producing a spontaneous magnetization (Figure 4-2). Such systems are known as canted antiferromagnets, or "weak ferromagnets".[49]

Neutron diffraction studies of $ND_4MnPO_4 \cdot D_2O$ and $KMnPO_4 \cdot D_2O$ have determined that the magnetic and chemical unit cells of the purely inorganic phosphates are coincident and that the magnetic easy-axis lies perpendicular to the metal plane along the crystallographic b-axis (Figure 4-3).[52,53] Neutron studies also show that the layers order antiferromagnetically with a subsequent transition to 3D order. While symmetry considerations require that the canted moment lies within the metal plane,[52] the magnitude of the canting angle is too small to be resolved from the neutron data.

A microscopic characterization of the ordered state of the divalent organophosphonates has not yet been achieved because of the difficulty in obtaining large amounts of the deuterated solids needed for neutron diffraction studies. However, the magnitude of the spontaneous magnetization moment is similar to that in the inorganic phosphates, indicative of a weak ferromagnetic state, and for Langmuir-Blodgett films of manganese octadecylphosphonate, $Mn(O_3PC_{18}H_{37})H_2O$, SQUID magnetometry has shown that the manganese $S = 5/2$ moments are aligned perpendicular to the metal planes and that the "weak ferromagnetic" moment lies within the metal plane.[10] These findings indicate that the magnetic structure of the organophosphonate materials is similar to that of the purely inorganic phosphate.

Antiferromagnetism

The ordered state of an antiferromagnet is characterized by an arrangement of magnetic moments that are aligned antiparallel to one another.[49] This arrangement can be represented by
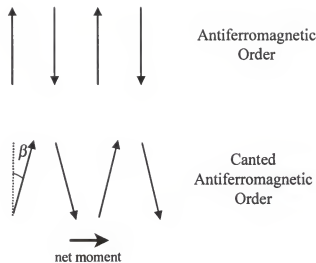
Figure 4-2. Representation of the magnetization vectors in an ordered antiferromagnetic state and in an ordered canted antiferromagnetic state.
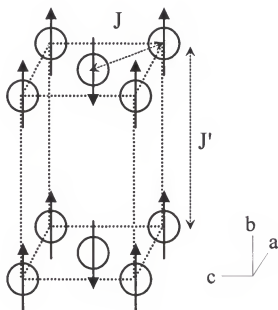
Figure 4-3. Representation of the antiferromagnetic structure of the Mn^{II} ($S = 5/2$) spins in the metal phosphates as determined from powdered neutron diffraction measurements. The canting angles are not included in this representation because the value of β is too small to be observed in the neutron data.

two interpenetrating sublattices, where each sublattice consists of spins of the same magnitude aligned parallel to one another and where the two sublattices have equal magnetization but are arranged in an antiparallel fashion (Figure 4-2). The direction parallel to the spin alignment is termed the magnetic easy-axis.

The interactions between nearest-neighbor spins are treated by mean-molecular field theory (MFT) as an effective internal magnetic field.[49] This effective internal field can be represented as an exchange field, H_E, which indicates how strongly the nearest-neighbors spins interact with each other, and as anisotropy fields, H_{A1} and H_{A2}, which give an indication of how the magnetic interactions vary as a function of orientation with respect to the magnetic principal axes. The anisotropy fields can be thought of as the sum of all internal factors that contribute to the lack of ideal isotropic magnetic interactions, with the most important quantities being single-ion interactions, such as dipole-dipole or crystal field interactions, and anisotropic exchange interactions, such as spin-orbit coupling effects. A distinction can be made between a uniaxial antiferromagnet, where $H_{A1} = H_{A2}$, and an orthorhombic antiferromagnet where $H_{A1} \neq H_{A2}$. For a uniaxial antiferromagnet, the magnetic interactions perpendicular to the magnetic easy-axis are isotropic, whereas for an orthorhombic antiferromagnet, the magnetic interactions in the plane perpendicular to the magnetic easy-axis are anisotropic.

In the ordered state of antiferromagnetic materials, a phenomenon termed spin-flop is observed when an applied magnetic field aligned parallel to the magnetic easy-axis exceeds a critical value termed the spin-flop field, H_{SF}, which is dependent upon the values of H_E, H_{A1} and H_{A2}.[49,139] For a uniaxial antiferromagnet the expression for the spin-flop field at 0 K is given by[49] $H_{SF} = [2H_E H_A - H_A^2]^{1/2}$. Immediately above this critical field, the direction of spin alignment will 'flop' to an orientation that is perpendicular to that of the original magnetic easy-axis, giving rise to a new phase called the spin-flop state (Figure 4-4).

The series of materials investigated here are known to be canted antiferromagnets. In a canted antiferromagnet, the sublattice magnetic moments are not collinear with each other, but
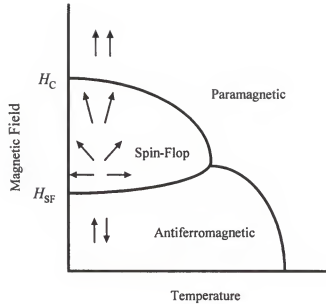
Figure 4-4. Magnetic field vs. temperature phase diagram for an antiferromagnet.

canted slightly from the magnetic easy-axis (Figure 4-2). This small perturbation from the antiferromagnetic state can be considered in the MFT approximation by an additional effective field, H_{D-M}, called the Dzyaloshinsky-Moriya interaction,[141,157] which is discussed in greater detail later.

Antiferromagnetic Resonance (AFMR)

AFMR is a type of electron magnetic resonance (EMR) that occurs in the ordered state of antiferromagnetic materials and can be described by principles similar to those used to represent nuclear magnetic resonance (NMR).[139,158] In the ordered antiferromagnetic state, the sublattice magnetic moments can be thought of as precessing about an equilibrium position. The effective internal magnetic field and the applied magnetic field act as forces that produce torques on the magnetic moments resulting in a precessional motion of the spins. This is schematically represented in Figure 4-5. The AFMR signals can be detected experimentally when the applied
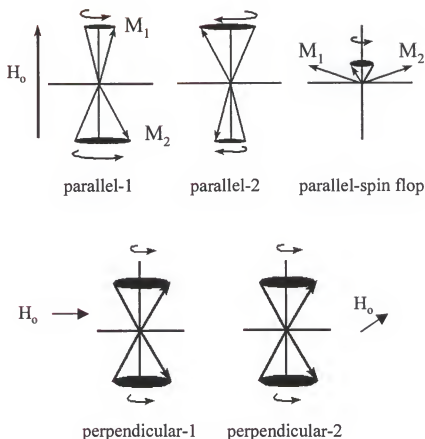
Figure 4-5. Representation of the precessional motion of the magnetization vectors as a function of orientation for an applied magnetic field that produce the antiferromagnetic resonance signals.

excitation source frequency equals the precessional frequency. Even in the absence of an applied external field, the internal fields result in a dynamic response, and this precessional frequency is referred to as the zero-field resonance. For an orthorhombic antiferromagnet, the zero-field resonance frequency is dependent upon orientation, and in a polycrystalline sample two distinct resonances can be detected, whereas in the uniaxial case, these two resonances are degenerate because $H_{A1} = H_{A2}$.

Applied external fields act as additional effective fields that modify the precessional frequency, and hence, the frequency of the observed AFMR signals from the zero-field values. The frequency of the detected AFMR signal will also depend upon the orientation of the applied magnetic field with respect to the magnetic principal axes.[153,154] Because of this orientational dependence, in a powdered sample where all possible orientations are represented equally, the AFMR signals corresponding to the modes of the three magnetic principal axes can be observed simultaneously (this is best observed when spectra are recorded as derivatives of the absorbance signals). For example, consider first the modes that originate from fields applied perpendicular to the magnetic easy-axis (Figure 4-5). For an orthorhombic antiferromagnet, there will be two signals, one from each perpendicular direction, whereas in a uniaxial antiferromagnet, these two resonances are degenerate because $H_{A1} = H_{A2}$.

The number of signals arising from the application of an applied field that is parallel to the magnetic easy axis does not differ for the uniaxial and orthorhombic antiferromagnet. When the applied field has a value $> H_{SF}$, one signal from the spin-flop state can be detected. For parallel applied fields that have values $< H_{SF}$, two parallel modes are observed, and these result as a consequence of two interpenetrating sublattices.[139] Therefore, for the parallel orientation, the value of the applied external magnetic field determines whether one or two AFMR signals are present; on the other hand, the number of perpendicular modes is determined by the presence or absence of in-plane anisotropy. The frequency dependence of the AFMR signals on the applied field for the specific case of a uniaxial antiferromagnet and for the general case of an orthorhombic antiferromagnet have been considered by Keffer and Kittel,[144,145] Nagamiya and Yosida,[146,159] and others,[160,161] and this dependence is shown graphically in Figure 4-6. Because the precessional frequencies of each mode, and hence the AFMR signals, depend upon both the applied fields and internal fields such as H_E, H_{A1}, H_{A2} and H_{D-M}, analysis of the frequency and field dependence of the AFMR signals of each of these modes gives information about the magnetic interactions of the ordered state.
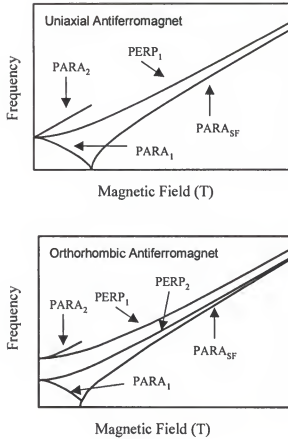
Figure 4-6. Frequency and field dependence of AFMR modes for a uniaxial and an orthorhombic antiferromangnet.

In addition to MFT, the spin-Hamiltonian formalism of superexchange is often used to describe interactions between nearest-neighbor spins. The spin-Hamiltonian for metal-metal exchange interactions in magnetic insulators is of the form $\mathcal{H} = -\Sigma J_{ij} S_i S_j$ where the sum is taken over all nearest neighbor pairwise interactions.[49] A negative value of J indicates antiferromagnetic exchange, and the magnitude of J indicates how strongly the spins interact with each other. By noting that S_i and S_j are vectors, the anisotropy of the exchange interaction[1,55] can be represented by the components $J_\alpha S_{ix} S_{jx}$, $J_\beta S_{iy} S_{jy}$ and $J_\gamma S_{iz} S_{jz}$. Single-ion anisotropy interactions, such as crystal field interactions or magnetic dipole interactions, can be introduced by additional

terms in the spin-Hamiltonian, typically of the form,[1,55] $-D\Sigma(S_{ix})^2$ and $E\Sigma[(S_{ix})^2 - (S_{iy})^2]$ (*Note*: conventionally, the z-axis is defined as the magnetic easy-axis, but here the x-axis is taken as the magnetic easy-axis because most of the original theories of AFMR are defined in this latter fashion). Although most of investigations of AFMR use the MFT formulation to interpret AFMR data, the mean field parameters H_E, H_{A1} and H_{A2} can be related to the spin-Hamiltonian formalism of magnetic interactions. The exchange field, H_E, in MFT is related to J and the number of nearest neighbor spins, and the anisotropy fields, H_{A1} and H_{A2}, are a combination of the anisotropy in the exchange and the single-ion anosotropy terms.

Experimental Section

Materials Used

Reagents used were of reagent grade quality and were obtained from commercial sources. Pentyl- and hexylphosphonic acid were prepared by acid hydrolysis of the corresponding alklyphosphonate esters prepared by the Michalis-Arbuzov reaction of the analogous alkylbromide with triethylphosphite.[162,163] All other alkyl- and arylphosphonic acids were purchased from Aldrich (Milwaukee, WI). Deionized water was purified with a Barnstead NANOpure (Boston, MA) system. Syntheses of powdered metal phosphonates have been described in detail by others,[11,12] however the procedure used here differed from the literature procedures where stoichiometric amounts of the phosphonic acid and metal salts are mixed together before adding KOH and warming. A modification of this procedure was used to help reduce the amount of precipitated manganese hydroxide impurities. Here an excess of the phosphonic acid was used and a 0.1 M KOH solution was added directly to the aqueous solution of the phosphonic acid raising the solution to pH 6-6.5. The solution was then heated to a temperature of 80° C. An aqueous solution of manganese chloride was then added to the warmed phosphonic acid solution. Warming of the solution helped to slow down the precipitation

reaction leading to a more crystalline product. The reactions were allowed to stir at 80° C for three days to help improve the crystallinity. Elemental analyses were consistent with the formulas $Mn(O_3PC_nH_{2n+1})H_2O$ for $n = 3$-6 alkylphosphonates and $Mn(O_3PC_6H_5)H_2O$ for the phenyl phosphonate. The ternary metal phosphate hydrate, $KMnPO_4 \cdot H_2O$ was prepared using published methods.[52,156]

SQUID Magnetometry Procedures

Magnetization measurements were performed using a Quantum Design MPMS SQUID magnetometer. A gel cap and plastic straw were used as a sample holder during the measurements. Background signals arising from the gel cap and straw were minimal and not subtracted from the reported data since the background contribution represented < 0.1 % of the observed signal intensity. Magnetization versus field measurements were performed at 2 and 5 K by sweeping the field both up and down over the range of 0 to 5 Tesla. Magnetization versus temperature measurements were run from 2 to 300 K. Samples were first cooled in the absence of an applied field and the magnetization was then measured on warming between 2 and 300 K in an applied field of 0.1 T to give the zero-field cooled data. Field cooled data were acquired by cooling the sample from 300 K in 0.1 T and measuring the magnetization from 2 to 300 K in the same 0.1 T applied field.

AFMR and EPR Procedures

All EPR and AFMR measurements were performed on powdered samples, and spectra were acquired using the high-field EMR facility at the National High Magnetic Field Laboratory (NHMFL) in Tallahassee, Florida. The frequency and field capabilities are summarized graphically in Figure 4-7. The EMR spectrometer design is shown in Figure 4-8 and is similar to that described earlier by Mueller et al.,[164] with the following modifications. Two different types

of millimeter and submillimeter wave radiation sources were used. Two Gunn oscillators (AB Millimetre, Paris) were used to access higher frequencies (95-380 GHz); one was tunable over the range of 92 - 98 GHz and the other over the range of 108 - 112 GHz. In addition to operating at the fundamental frequencies, these Gunn sources were equipped with sets of Schottky-diode harmonic generators and filters that enabled operation at frequencies near 190, 285, and 380 GHz for the low frequency oscillator, as well as 220 and 330 GHz for the higher frequency Gunn source. A second type of source, a Millimeter Vector Network Analyzer (MVNA) produced continuous fundamental frequencies of 8 - 18 GHz. Equipped with a series of Schottky-diode harmonic generators, the MVNA provided an essentially continuous source from 24 - 133 GHz, where the lower end was limited by the detector sensitivity. An EIP 578B counter was used as a frequency lock source for the Gunn oscillators and the MVNA source, and it also measured the frequency. The Zeeman field was produced by an Oxford Instruments Teslatron superconducting magnet capable of field sweeps from 0 - 17 T. The resonance absorption was measured at a fixed frequency by monitoring the transmitted power as a function of the applied magnetic field that is swept through the resonance with either an increasing or decreasing field. Since the signals were broad, a relatively fast sweep rate, typically 0.2 T/min was used. This resulted in a hysteresis of the magnetic field as read by the power supply current. To account for this hysteresis, typically 0.02 T, resonance fields are reported as the average of the signals detected in an up-field and down-field sweep. The field was modulated in the usual fashion with a frequency of 4 - 10 kHz, and phase detection was employed. A liquid helium cooled hot-electron InSb bolometer from QMC (London, England) was used as the power detector. All AFMR measurements were performed at 5 K, and the EPR spectra were taken over the range of 20 - 285 K, each with the use of an Oxford Instruments CF-1200 continuous flow liquid helium cryostat. Typical powder sample sizes were 20 - 30 mg when the Gunn oscillators were used as sources, and 100 - 200 mg when the MVNA was used as the source. Samples were ground into fine powders to ensure equal representation of all orientations.
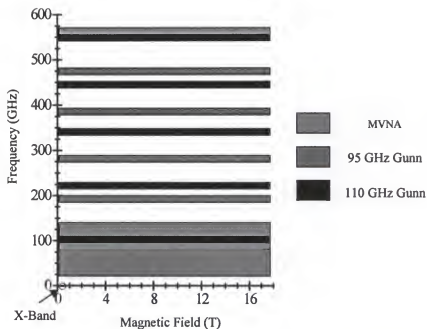
Figure 4-7. Summary of the frequency and field capabilities of the high-field EMR facilities at NHMFL.
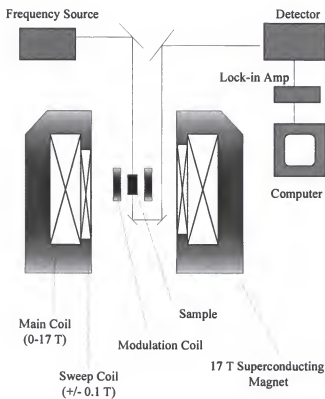
Figure 4-8. Design of the high-field electron magnetic resonance instrument.

Results and Discussion

Antiferromagnetic Resonance

At temperatures below the ordering temperature, T_N, antiferromagnetoc resonance (AFMR) signals were observed for each sample. Figure 4-9 gives representative spectra of the EPR signal at room temperature and the AFMR signals observed at 5 K for a powder of manganese pentylphosphonate, $Mn(O_3PC_5H_{11})H_2O$. As shown in this figure, with an excitation source frequency of 380.84 GHz the EPR signal occurs at 13.57 ± 0.01 T and the value of the g-factor is 2.00 ± 0.03. (*Note*: The reader is reminded that spectra, such as those in Figures 4-9 and 4-10, are actual data recorded with either an up-field or down-field sweep. The resonance field values reported in the text correspond to the actual spectra, whereas the resonance field values plotted in Figure 4-11 and the values of the reported g-factor represent the average value determined from both an up-field and down-field sweep.) For frequencies of 95 to 380 GHz, no anisotropy of the g-factor was apparent in the EPR signals for any of the samples studied. At this source frequency, for temperatures below T_N, three AFMR signals are clearly observed, as shown in Figure 4-9. The signal at lowest field, 12.65 ± 0.02 T, corresponds to the perpendicular mode where the applied field is along the direction of the net canted moment, labeled $PERP_2$. The next signal, at 13.45 ± 0.02 T, arises from the other perpendicular orientation, $PERP_1$, and the last signal at 13.71 ± 0.02 T, designated $PARA_{SF}$, is the mode where the applied field is parallel to the magnetic easy-axis and has values larger than the spin-flop field, H_{SF}. For excitation source frequencies of the higher harmonics of the 95 and 110 GHz Gunn oscillators, a similar pattern of three signals is detected for all six samples. The presence of two perpendicular modes is characteristic of an orthorhombic antiferromagnet, and the pronounced splitting between these two modes is indicative of large in-plane anisotropy. The zero-field resonance frequencies for the two perpendicular modes differed by ~ 60 GHz for each of the materials studied.
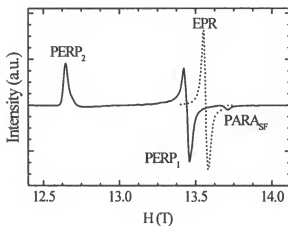
Figure 4-9. EPR and AFMR spectra of manganese pentylphosphonate. The AFMR spectrum, solid line, was recorded at 5 K, whereas the EPR spectrum, dashed line, was recorded at room temperature. Both spectra were recorded as up-field sweeps.
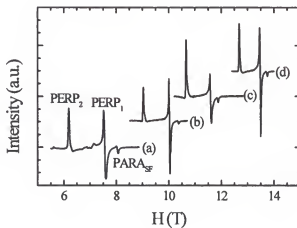
Figure 4-10. AFMR spectra detected for manganese pentylphosphonate at 5 K with source frequencies of (a) 218.18 GHz, (b) 285.42 GHz, (c) 330.37 GHz, and (d) 380.84 GHz, all with up-field sweeps.

Figure 4-10 shows AFMR spectra acquired for manganese pentylphosphonate at several frequencies. It is clear from this figure how the resonance field of each of the three signals changes as a function of source frequency. This dependence is depicted in Figure 4-11, which summarizes in the frequency and field plane the AFMR signals detected for (A) $KMnPO_4 \cdot H_2O$, (B) manganese phenylphosphonate, (C) manganese propylphosphonate, (D) manganese butylphosphonate, (E) manganese pentylphosphonate and (F) manganese hexylphosphonate. The solid lines are fits to available theory and will be discussed in greater detail below. Each data point in the frequency and field plane represents an observed AFMR signal of the types shown in Figures 4-9 and 4-10.

Data points in the frequency and field area of 30 - 130 GHz and 0 - 5 T were acquired with the MNVA source with appropriate Schottky-diode harmonic generators. Figure 4-12 shows typical AFMR signals for manganese hexylphosphonate detected with this source at 5 K. The signal at 1.36 ± 0.04 T for a source frequency of 50.24 GHz in Figure 4-12A belongs to the parallel branch below the spin-flop field. The small signal at 2.1 ± 0.1 T, as well as that at 2.0 ± 0.1 T in Figure 4-12B, indicate the field at which spin-flop[139] occurs, H_{SF}. Figure 4-12B shows signals originating from the parallel orientation for fields both below and above H_{SF}, occurring at 0.21 ± 0.04 T and 3.29 ± 0.04 T respectively. In Figure 4-12C, the signal at 0.25 ± 0.04 T for source frequency of 130.23 GHz originates from the perpendicular direction (PERP$_2$), along which the canted moment lies.

When using the MVNA source, assignment of the frequencies of the AFMR signals was sometimes complicated by more than one harmonic of the fundamental frequency passing through the system. To aid in the assignments, scans were taken above T_N, (typically 25 K for the organophosphonates and at 35 K for $KMnPO_4 \cdot H_2O$), and below T_N for each fundamental frequency run with a given harmonic generator. This procedure identified which harmonics of the fundamental frequencies were present as excitation sources in the AFMR spectra. When more than one frequency was present, modes were assigned by slightly changing the fundamental
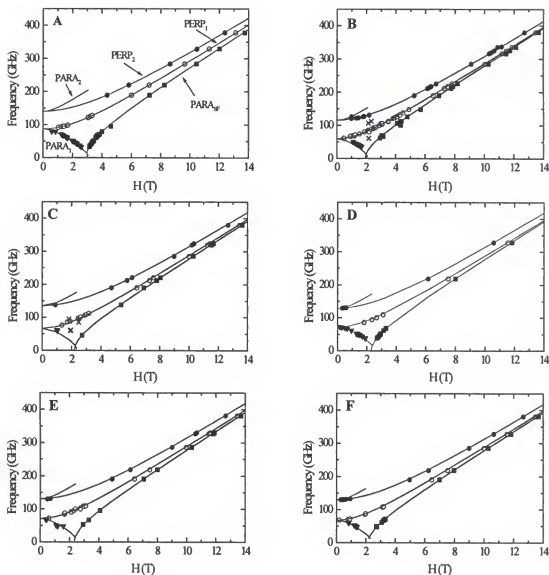
Figure 4-11. Frequency and field dependence of the AFMR signals detected at 5K for (A) KMnPO$_4$·H$_2$O, (B) manganese phenylphosphonate, (C) manganese propylphosphonate, (D) manganese butylphosphonate, (E) manganese pentylphosphonate, and (F) manganese hexylphosphonate. The solid lines are fits to conventional theory as described later in the text. The various signal origins are depicted as follows: solid circles, PERP$_2$; open circles, PERP$_1$; solid triangles, PARA$_1$ ($H_o < H_{SF}$); solid squares, PARA$_{SF}$ ($H_o > H_{SF}$): cross hatches, H_{SF}. Each resonance field represents the average of at least two signals detected in both an up-field and down-field sweep.
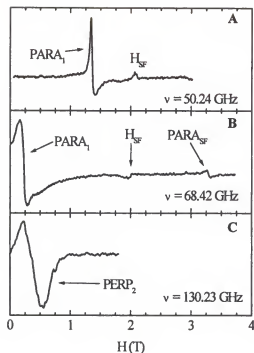
Figure 4-12. AFMR spectra detected for manganese hexylphosphonate at 5 K while using the MVNA source: **(A)** source frequency of 50.24 GHz with signals belonging to PARA$_1$ and H_{SF}, **(B)** source frequency of 68.4 GHz with signals belonging to PARA$_1$, PARA$_{SF}$ and H_{SF}, **(C)** source frequency of 130.23 GHz with signal belonging to PERP$_2$. The signals have been scaled to similar intensities.
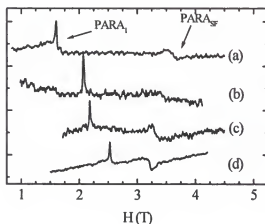
Figure 4-13. AFMR spectra detected at 5 K for KMnPO$_4$·H$_2$O with source fequencies of (a) 61.05 GHz, (b) 50.10 GHz, (c) 45.50 GHz, and (d) 36.32 GHz. The signals originating from the PARA$_1$ branch moves to higher field as the frequency decreases, while the opposite trend is observed for the PARA$_{SF}$ signals. The signals reported are scaled to similar intensities.

frequency and watching which way the AFMR signal(s) shifted. Signals belonging to the lower parallel mode, for applied fields < H_{SF} (mode assignments are discussed in more detail below), move to lower field with higher frequency, whereas all other modes shift to higher field as the frequency is increased. The progression of the AFMR signals of the PARA$_1$ and PARA$_{SF}$ modes as a function of frequency can be observed in Figure 4-13 for KMnPO$_4$·H$_2$O. For example, as the frequency increases from 36.32 GHz to 61.05 GHz, the signals belonging to the PARA$_1$ mode move from 2.52 ± 0.04 T to 1.81 ± 0.04 T, and are given by the solid triangles in Figure 4-11A, whereas the signals due to the parallel orientation once spin-flop has occurred (PARA$_{SF}$) move from 3.2 ± 0.1 T to 3.6 ± 0.1 T in Figure 4-13 and are given by the solid squares in Figure 4-11A.

Static SQUID Magnetometry

Spin-flop fields were determined for powdered samples from analysis of the frequency versus field dependence of the AFMR signals as well as from SQUID magnetometry magnetization versus field measurements. Figure 4-14 shows the results of magnetization versus field scans for each sample, with each curve vertically offset from the previous curve by 0.3 emu·G for clarity. Due to the presence of all orientations in a powdered sample, the spin flop field, H_{SF}, does not appear as a sharp transition in the magnetization curve, but rather as a small inflection.[49] For KMnPO$_4$·H$_2$O, H_{SF} was found to be 3.2 ± 0.1 T, higher than values of 2.3 to 2.6 T found for the manganese organophosphonates studied. These values are given for each compound in Table 4-1 and are in agreement with the values of the spin-flop field found from AFMR analyses.

Figure 4-15 shows the susceptibility versus temperature plots from 2 to 300 K for manganese pentyl- and hexylphosphonate, offset vertically by 0.1 emu/mol. The broad maximum in the temperature dependent static susceptibility is characteristic of antiferromagnetic exchange,[49] and the sharp change in the susceptibility near 14 K indicates the ordering transition
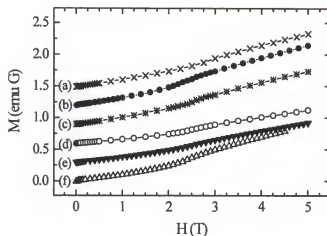
Figure 4-14. Magnetization vs. field curves for (a) manganese phenylphosphonate, (b) manganese hexylphosphonate, (c) manganese pentylphosphonate, (d) manganese butylphosphonate, (e) manganese propylphosphonate, (f) KMnPO$_4$·H$_2$O all at 2 K showing an inflection due to the spin-flop transition. Curves are vertically off-set by 0.3 emu·G for clarity.
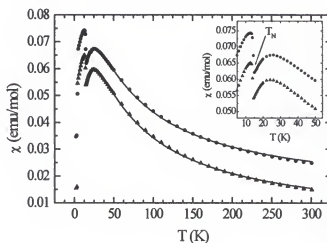
Figure 4-15. Magnetic susceptibility vs. temperature plots for manganese pentylphosphonate (filled circles) and manganese hexylphosphonate (filled triangles) with an applied field of 0.1 T, vertically off-set by 0.1 emu/mol for clarity. The solid lines are fits to the data and are discussed in the text. The data for $T < 50$ K are plotted in the inset for clarity of $T\chi_{max}$ and T_N.

to the "weak ferromagnetic" state.[141] The solid lines in Figure 4-15 are fits between 25 and 300 K using a quadratic-layer antiferromagnet model for a 2-dimensional lattice of $S = 5/2$ spins with Heisenberg antiferromagnetic nearest-neighbor exchange.[78] The values of the nearest neighbor exchange constants, J, for manganese pentyl- and hexylphosphonate are determined from the temperature of maximum susceptibility,[49] $T\chi_{max}$, according to $|J|/2k = T\chi_{max}/2.05S(S+1)$, and these values are included in Table 1. Values of J for the other materials are taken from literature references,[22,52,65] (Table 4-1). Figures 4-16A and 4-17A show field cooled and zero-field cooled magnetization data over the temperature range of 2 to 25 K. The difference plots are shown in Figures 4-16B and 4-17B for the pentyl and hexyl samples, respectively. The ordering temperature, T_N, is defined as the temperature of the onset of the sharp increase in the magnetic
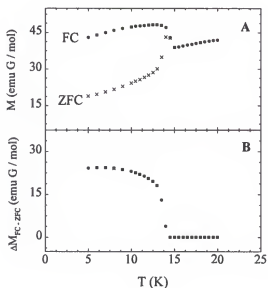
Figure 4-16. Magnetization vs. temperature for manganese pentylphosphonate. **(A)** Comparison of the data taken upon warming after cooling in zero-applied field (ZFC) and cooling in an applied field (FC). In both cases, the measuring field was 0.1 T. The ordering temperature, T_N, is observed as the discontinuity in the ZFC plot at 14.65 K. **(B)** The difference of the two plots in (A) showing the spontaneous magnetization below T_N.
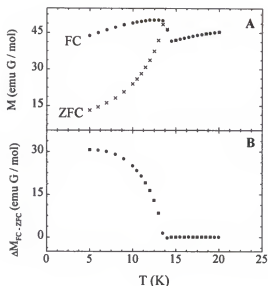
Figure 4-17. Magnetization vs. temperature for manganese hexylphosphonate. (A) Comparison of the data taken upon warming after cooling in zero-applied field (ZFC) and cooling in an applied field (FC). In both cases, the measuring field was 0.1 T. The ordering temperature, T_N, is observed as the discontinuity in the ZFC plot at 14.10 K. (B) The difference of the two plots in (A) showing the spontaneous magnetization below T_N.

Table 4-1. Magnetic Parameters Determined from SQUID Magnetometry Measurements.

Sample	T_N (K)	$T\chi_{max}$ (K)	$-J$ (K)	Θ (K)[a]	μ_{eff}/μ_β	μ_{ferro}/μ_β	α (deg)[b]	H_{SF} (T)[c]
KMnPO$_4$·H$_2$O[d]	18.40(2)	29.8(4)	3.31(6)	-62.7(3)	5.36(1)	3.5e-3(3)	0.03(1)	3.2(1)
Mn(O$_3$PC$_6$H$_5$)H$_2$O[e]	12.1(1)	19(1)	2.2(2)	-46(1)	6.00(3)	NA[f]	NA[f]	2.4(2)
Mn(O$_3$PC$_3$H$_7$)H$_2$O[g]	14.90(2)	22.4(4)	2.48(8)	-51.7(4)	5.45(1)	0.0143(1)	0.15(1)	2.6(2)
Mn(O$_3$PC$_4$H$_9$)H$_2$O[g]	15.00(2)	22.4(4)	2.48(6)	-54.49(3)	5.45(1)	0.0278(1)	0.29(1)	2.5(1)
Mn(O$_3$PC$_5$H$_{11}$)H$_2$O	14.65(2)	25.5(3)	2.85(4)	-48.9(1)	5.67(3)	0.0438(2)	0.44(2)	2.5(2)
Mn(O$_3$PC$_6$H$_{13}$)H$_2$O	14.10(2)	24.0(3)	2.65(4)	-56.1(1)	5.91(3)	0.0553(2)	0.54(2)	2.3(2)

[a] Weiss constant. [b] α is the canting angle determined from bulk magnetization measurements, $\sin^{-1}\alpha = \mu_{ferro}/\mu_{eff}$ (ref. 22).[c] H_{SF} values for all samples have been determined from our measurements. [d] Data taken from ref. 52. [e] Data are taken from ref. 65. [f] Values not reported in ref. 65. [g] Data are taken from ref. 22.

susceptibility.[141] Figures 4-16 and 4-17, and the inset in Figure 4-15, clearly show the sharp increase in the magnetic susceptibility that occurs at T_N. The values of T_N are 14.65 K for manganese pentylphosphonate and 14.10 K for manganese hexylphosphonate. Weak ferromagnetic moments of 0.044 and 0.055 μ_β, were calculated from the maximum of ΔM_{FC-ZFC}, for the pentyl- and hexylphosphonates, respectively. The value of the weak ferromagnetic moments determined from the magnetometry measurements are expected to represent a lower limit of the actual value (this issue is discussed in greater detail later in the text). Compilations of magnetic parameters from bulk magnetization measurements, which are taken from literature references[22,23,52,65] and from the present work, are given in Table 4-1.

Data Analysis

The data shown in Figure 4-11, representing the observed AFMR signals in the frequency and field plane, were fit with the conventional MFT of AFMR[144-146,159-161] for an orthorhombic antiferromagnet modified to include a Dzyaloshinsky-Moriya interaction, H_{D-M}, as a canting term.[165,166] In the following analysis, the magnetic easy-axis is denoted by the x-direction (which corresponds to the crystallographic b-axis). The y- and z-directions correspond to the ac crystallographic plane, with the z-direction taken as the direction along which the moments cant from the easy-axis. In Figure 4-11A, the curve labeled PERP$_2$ corresponds to the crystallographic c-axis for $KMnPO_4 \cdot H_2O$ (Figure 4-3), which is the direction along which the Mn^{II} S = 5/2 spins are canted.[52] This branch (PERP$_2$) for the organophosphonates also corresponds to the direction of the canting moment, however since measurements were made on powders and the relationship between the magnetic and chemical unit cells is unknown, the in-plane crystallographic orientation cannot be ascribed. The curve labeled PERP$_1$ represents the other in-plane direction perpendicular to the magnetic easy-axis, which is along the crystallographic a-axis in $KMnPO_4 \cdot H_2O$. The frequency and field dependence of these lines are given by:[160,165,166]

$$\text{PERP}_1; \qquad \omega/\gamma = (H_o^2 + C_1^2)^{1/2} \tag{4-1}$$

$$\text{PERP}_2; \qquad \omega/\gamma = (H_o^2 + H_{D-M}H_o + C_2^2)^{1/2} \tag{4-2}$$

$$C_1 = (2M_o^2(Q_x - Q_y)(A + 1/2Q_x))^{1/2} \tag{4-3}$$

$$C_2 = (2M_o^2(Q_x - Q_z)(A + 1/2Q_x))^{1/2} \tag{4-4}$$

where ω/γ is the resonance frequency, H_o is the applied field, H_{D-M} is the canting term, C_1 and C_2 are the zero-field resonance terms, all in units of Tesla (T), and with $M_o = N(g/2)\mu_B<S> = 13.96$ $Jmol^{-1}T^{-1}$. Here, C_1 and C_2 are expressed by the method of Date[160,161] with the removal of additional anisotropy terms (P_x, P_y, and P_z in reference 160) which were included in the original formulation of the theory to account for large orbital angular momentum contributions to the anisotropy energy. For Mn^{II}, where $S = 5/2$, contributions from orbital angular momentum can be neglected. This formalism is expressed in terms of the symmetric isotropic exchange term, A, and the anisotropic interaction terms, Q_x, Q_y, and Q_z, where the Q_i terms show the magnitude of the deviations from the isotropic Heisenberg limit. These are related to the exchange field H_E and the anisotropy fields, H_{A1} and H_{A2}, from the methods of Nagamiya, Yosida, and Kittel by:[144-146,159]

$$H_E = M_oA \tag{4-5}$$

$$H_{A1} = M_o(Q_x - Q_y) \tag{4-6}$$

$$H_{A2} = M_o(Q_x - Q_z). \tag{4-7}$$

The curve labeled PARA$_{SF}$ represents the orientation where the applied magnetic field is parallel to the magnetic easy-axis (perpendicular to the metal planes) and has a value $> H_{SF}$. The frequency and field dependence of this mode is given by:[160,165,166]

$$\text{PARA}_{SF}; \qquad \omega/\gamma = (H_o^2 + H_{D-M}H_o - C_3^2)^{1/2} \tag{4-8}$$

$$C_3 = (2M_o^2(Q_x - Q_y)(A + 1/2Q_y))^{1/2}. \tag{4-9}$$

The curves labeled PARA$_1$ and PARA$_2$ correspond to the orientation where the applied field is parallel to the magnetic easy-axis and where its value $< H_{SF}$. In contrast to ferromagnetic resonance[139] where there is only one parallel mode, there are two parallel AFMR modes for

applied fields $< H_{SF}$ due to the presence of two sublattices. The expressions for these modes are quite complicated and are found by solving expression 16 of reference 160. A simplification of this expression was made for our system, and the resulting equations were used to fit the data (simplifications and derivation are given in the Appendix-B).

$$\text{PARA}_{1\&2}; \quad \omega/\gamma = \{0.5 \,[C_1^2 + C_2^2 + H_o^2(1+\lambda^2)]$$

$$\pm \text{SQRT}\{(C_1^2 + C_2^2 + H_o^2(1+\lambda^2))$$

$$- 4(H_o^2\lambda^2 - H_o^2(C_1^2 + C_2^2) + C_1^2C_2^2)]\}\}^{1/2} \tag{4-10}$$

$$\lambda = [1 - (A + 1/2Q_x)\chi_{\parallel}] \tag{4-11}$$

where λ is a variable parameter which can be used to approximate the value of $\chi_{\parallel}$, and C_1 and C_2 are defined in equations (4-3) and (4-4).

Generally a modified field of the type, $H_{mod} = (g/2)H_{exp}$, which accounts for the reduction of the g-tensor to a scalar g-factor is applied to the observed signals before the data can be fit with theory.[144-146,159] However, this modification was neglected since no anisotropy was present in the g-factor, and the values of the g-factor for these materials were found to be 2.00 ± 0.03, producing corrections that were less than the experimental error in the resonance fields, typically 0.02 to 0.1 T. However, when anisotropy of the g-factor is present or when its value differs significantly from 2.00, this correction must be employed.

The observed AFMR resonance signals were fit with equations (4-1), (4-2) and (4-8), which provide values of H_{D-M}, C_1, C_2 and C_3. Although the canting of the sublattice magnetization vectors is too small to be determined from neutron diffraction experiments,[52] inclusion of the canting term is necessary to produce satisfactory fits of the frequency and field dependence of the AFMR signals. For the manganese phosphonates studied here, the canting term has the greatest effect on the PERP$_2$ and PARA$_{SF}$ modes in the frequency ranges of 35 - 70 GHz and 120 - 135 GHz, respectively. The MVNA source provides access to these frequencies, making it possible to observe the effect of the canting and to determine the value of the

Dzyaloshinsky-Moriya interaction. From the values of C_1, C_2 and C_3, along with the relation that $Q_x + Q_y + Q_z = 0$, equations (4-3), (4-4) and (4-9) are solved to determine the values of A, Q_x, Q_y and Q_z. These values are listed in Table 4-2. The values of the symmetric exchange field, H_E, and of the anisotropy fields, H_{A1} and H_{A2}, are listed in Table 4-3. The canting angle, β, is estimated from the expression:[167]

$$\tan 2\beta \cong H_{D\text{-}M} / H_E \qquad (4\text{-}12)$$

and the values of $H_{D\text{-}M}$ and β for each material are reported in Table 4-3.

The magnetic interaction parameters determined in the mean molecular field formalism can be related to the superexchange interactions of the spin-Hamiltonian formulation. The exchange field ($H_E = AM_o$) is related to J by $A = n|J|$, where n is the number of nearest neighbors. (Note: A conversion factor of $N\mu_B^2/k = 0.325$ emu/mol is useful for the conversion of units between K and mol/emu.[49,72]) The anisotropy fields, H_{A1} and H_{A2}, represent both single-ion and exchange anisotropy. If the value of J is known independently, for example from bulk magnetization measurements, then the anisotropic exchange terms, Q_i, can be easily determined by solving equations (2-3) and (2-4) along with the relationship $Q_x + Q_y + Q_z = 0$. For each of the materials studied here, the values of Q_i calculated in this way were consistent with those determined from fitting the AFMR data alone.

Table 4-2. Values of the Symmetric Isotropic Exchange Parameter, A, and of the Anisotropic Interaction Parameters, Q_x, Q_y, and Q_z, Determined from Analysis of the AFMR Signals.

Sample	$A \pm 0.02$ (T^2 mol/J)	$Q_x \pm 0.002$ (T^2 mol/J)	$Q_y \pm 0.001$ (T^2 mol/J)	$Q_z \pm 0.002$ (T^2 mol/J)
$KMnPO_4 \cdot H_2O$	1.33	0.022	0.003	-0.025
$Mn(O_3PC_6H_5)H_2O$	0.88	0.020	0.007	-0.027
$Mn(O_3PC_3H_7)H_2O$	1.01	0.025	0.010	-0.034
$Mn(O_3PC_4H_9)H_2O$	0.99	0.023	0.007	-0.030
$Mn(O_3PC_5H_{11})H_2O$	1.13	0.020	0.007	-0.028
$Mn(O_3PC_6H_{13})H_2O$	1.06	0.021	0.008	-0.030

Table 4-3. Magnetic Parameters Determined from AFMR Measurements.

Sample	H_E ± 0.1(T)	H_{A1} ± 0.3(T)	H_{A2} ± 0.3(T)	H_{SF} ± 0.1(T)	$H_{D\text{-}M}$ ± 0.1(T)	β ± 0.2(deg)
KMnPO$_4$·H$_2$O	18.5	0.26	0.65	3.1	0.5	0.9
Mn(O$_3$PC$_6$H$_5$)H$_2$O	12.2	0.18	0.66	2.2	0.4	0.9
Mn(O$_3$PC$_5$H$_7$)H$_2$O	14.1	0.21	0.82	2.3	0.3	0.7
Mn(O$_3$PC$_4$H$_9$)H$_2$O	13.9	0.22	0.74	2.5	0.4	0.8
Mn(O$_3$PC$_5$H$_{11}$)H$_2$O	15.8	0.20	0.67	2.5	0.5	0.7
Mn(O$_3$PC$_6$H$_{13}$)H$_2$O	14.8	0.19	0.73	2.4	0.4	0.8

Magnetostructural Correlations

Substituent effects

A comparison of how the substituents influence the magnetic properties within this series of layered solids is possible since they possess nearly isostructural frameworks within the metal-oxygen-phosphorus layers. In the metal phosphonates, the layers of manganese ions are separated by the phosphonate organic groups, while in the purely inorganic KMnPO$_4$·H$_2$O, potassium ions lie in the interlayer region and the organic groups are replaced by a phosphate oxygen. Crystal structures are known for KMnPO$_4$·H$_2$O[52] and Mn(O$_3$PC$_6$H$_5$)H$_2$O,[16] and the alkylphosphonates are isostructural with these based on unit cell determinations from powder X-ray data.[16,17]

The magnitude of the isotropic magnetic exchange, given by the exchange field, H_E, for the series of materials ranges from a high of H_E = 18.5 T for the inorganic KMnPO$_4$·H$_2$O to H_E = 12.2 T for Mn(O$_3$PC$_6$H$_5$)H$_2$O, with the alkylphosphonates having intermediate values of H_E. Assuming identical superexchange pathways, the trend can be accounted for by electronic effects of the XPO$_3{}^{2-}$ bridging ligands. Based on frontier orbital interaction considerations, electron donating substituents should increase antiferromagnetic interactions mediated by the XPO$_3{}^{2-}$ bridge due to a better energy match between the metal d-orbitals and the bridging ligand orbitals.[66] This effect was recently demonstrated for a series of dimeric vanadyl

arylphosphonates, where phosphonate mediated superexchange increased with the electron donating capacity of the arylphosphonate substituents.[48] For the series studied here, the electron donating character of the substituents decreases in the order O^- > alkyl > phenyl, consistent with the observed trend in exchange fields $H_E(KMnPO_4 \cdot H_2O)$ > $H_E(Mn(O_3PC_nH_{2n+1})H_2O)$ > $H_E(Mn(O_3PC_6H_5)H_2O)$.

The above discussion assumes that the exchange pathway is the same for each member of the series. Figure 4-18 depicts three possible pathways that connect each of the manganese ions to each of its four nearest neighbors. The exchange interaction through the Mn-O-Mn bridge, labeled as pathway one is the most direct and thought to be the dominant pathway for magnetic exchange. For $KMnPO_4 \cdot H_2O$[52] and $Mn(O_3PC_6H_5)H_2O$,[16] which have the highest and lowest exchange, the Mn-O-Mn bridging angles are similar, with values of 117.5° and 117.8°, respectively. Although the O-P-O and O-Mn-O bond angles differ, we expect these variations, that influence pathways two and three, to have little influence on the magnetic exchange by analogy with other systems.[48,71,168] In dinuclear transition metal complexes that are doubly- and triply-bridged by one μ-oxo bridge and one or more carboxylate or phosphonate ligands, it has been found that the carboxylate and phosphonate bridges play a negligible role as exchange pathways when compared to the bridging oxide.[67,168] Although chair-like O-P-O bridges are the sole pathways mediating magnetic exchange in materials such as $VO(O_3PC_6H_5)H_2O$,[48] this pathway requires proper symmetry and geometrical arrangements.[71] The magnitude of exchange in vanadyl phosphonates where the exchange pathway occurs through V-O-V bridges is much stronger than in those materials where the magnetic exchange is limited to V-O-P-O-V pathways.[48] Hence, it is expect that pathways two and three have only a small contribution to the magnetic exchange between nearest-neighbor Mn ions, and small changes in the O-P-O and O-Mn-O bond angles should not be able to account for the differences in exchange energies
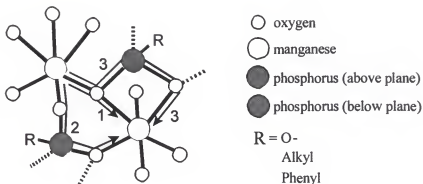
Figure 4-18. Representation of the exchange pathways that connect each of the Mn ions to its four nearest-neighbors.

observed for the materials studied here. Because the Mn-O-Mn bond angles are nearly identical for the inorganic phosphate and phenylphosphonate samples, the changes in exchange energies are most likely attributed to electronic perturbations of the XPO_3^{2-} bridge that result from the electron withdrawing/donating properties of the ligand substituents.

Exchange anisotropy

In general, the temperature at which a transition to long-range antiferromagnetic order occurs should scale with the strength of the exchange energy. In this series, the inorganic phosphate has the highest T_N (18.40 K) followed by the alkylphosphonates (14.10-15.00 K) and then the phenylphosphonate (12.1 K), and this progression is in agreement with the order of the measured exchange energies. The layered nature of these materials leads to very small interlayer exchange energies, and ordering is thought to be 2-dimensional (with subsequent 3-dimensional ordering as the temperature is lowered further[23]). The presence of Ising-type anisotropy is a

requisite for long-range magnetic order in a two-dimensional lattice.[1] Although Mn^{II} ($S = 5/2$)

ions nominally experience isotropic (Heisenberg) exchange interactions, analysis of the AFMR

signals reveals that magnetic anisotropy is present in the ordered state. In general, magnetic

anisotropy can be considered to arise from anisotropic exchange interactions and/or single-ion

anostropy terms, and the anisotropy fields, H_{A1} and H_{A2}, in the MFT formalism of AFMR have

contributions from both types of effects.[166] In the materials presented here, we are unable to

separate the contributions of each type of anisotropy to the Q_i values. Therefore, the values of Q_i

reported in Table 4-2, have contributions from both the anisotropy in the exchange and the single-

ion anisotropy terms.

The magnitude of the combined anisotropy of the magnetic interactions may explain an

anomaly observed in the ordering temperatures for the series of alkyl phosphonates. The

manganese propyl- and butylphosphonates order at higher temperatures than the manganese

pentyl and hexyl samples, although the exchange energies are larger in the latter two materials

(Table 4-1). Analysis of the AFMR data indicates that the magnetic anisotropy ((Q_x - Q_z)/A and

(Q_x - Q_y)/A) is greater in the manganese propyl- and butylphosphonates. This larger anisotropy

may be responsible for the increased ordering temperatures of the propyl- and butylphosphonates

despite similar or slightly lower exchange energies. Since crystal structures are not available for

the series of alkylphosphonates, it is not possible to unambiguously identify the subtle structural

changes that are responsible for the differences observed in the magnetic parameters. However,

assuming the same intralayer spacing of the XPO_3^{2-} ligands in the alkylphosphonates that are

present in the phenylphosphonate, van der Waals interactions between adjacent alkyl groups are

expected to become important for alkyl chain lengths greater than four carbons.[16] It is not

unreasonable to infer that subtle structural differences exist between the shorter chain propyl- and

butylphosphonates and the longer chain pentyl- and hexylphosphonates.

Canting moments

There are two kinds of anisotropic coupling mechanisms that can produce canting of the sublattice magnetization vectors.[49,141,166,169] Antisymmetric exchange, which is proposed to occur for a variety of site symmetries and which operates in addition to symmetric Heisenberg exchange, is described by:

$$\mathcal{H}_{aniso} = \mathbf{d}[S_1 \times S_2] \tag{4-12}$$

where $\mathbf{d}$ is a constant vector which depends upon the symmetry of the crystal. This type of interaction is seen in α-FeO_3 and is often referred to as a Dzyaloshinsky-Moriya vector.[49,141,165] The other mechanism, as seen in NiF_2 and related crystals, is single-ion magnetocrystalline anisotropy energy,[169] which results when there are two equivalent sites of magnetic ions but the directions of their anisotropy axes are different. In the metal organophosphonates, since the symmetry of the space group $Pmn2_1$ is sufficiently low, it is believed that the first mechanism operates and antisymmetric exchange is responsible for the spontaneous magnetization in these materials.[22]

The Dzyaloshinsky-Moriya exchange term, H_{D-M}, was determined from fitting the $PERP_2$ and $PARA_{SF}$ modes with equations (4-2) and (4-8), respectively. Although the canting of the sublattice magnetization vectors was too small to be detected in neutron diffraction experiments on $KMnPO_4 \cdot H_2O$, inclusion of the canting term in the AFMR analysis was necessary to produce satisfactory fits to the experimental data. The values of β for each material, which are listed in Table 4-3, show that the canting angle was quite similar for all of the materials and that its value ranged from 0.7-$0.9 \pm 0.2°$. Apparently the strength of this interaction in these materials is not directly affected by the identity of the phosphate/phosphonate substituent. This result is in contrast to the estimates of the canting angle determined from SQUID magnetometry measurements that show that the values of the canting angle (denoted by α in Table 4-1) are 2 - 5 times smaller than those determined from the AFMR measurements (denoted by β in Table 4-3)

and that these values change as the phosphonate substituent is varied. However, because these materials are powdered, magnetization measurements are a statistical average over all particle orientations, and estimates of the canting moment obtained in this way are lower than the canting moments measured by AFMR. Also, the varied estimates of the canting moment obtained from magnetization measurements may result from contributions of uncompensated spins at domain boundaries as well as having contributions from inhomogeneous sample packing because of irregular particle size and shape. The canting angles determined from AFMR are not affected by sample packing since H_{D-M} is determined by the energy of the AFMR modes and not the intensities. It is worth noting that had single crystals been available for this study, AFMR could have observed not only the magnitude, but also the direction of the spin canting.

Conclusions

AFMR provides a microscopic probe of antiferromagnetic materials. The high field EMR facilities at NHMFL, with field sweep capabilities from 0 to 17 T, the availability of several frequency sources, and variable temperature capabilites, make this technique applicable to a wide range of materials. This chapter has shown how AFMR can be easily used to compare the magnetic parameters of chemically similar materials. Some of the advantages of AFMR over other microscopic probes have been demonstrated, including high sensitivity to subtle differences in magnetic interactions, and the ability to work with a small amount of material.

Measurements performed on $KMnPO_4 \cdot H_2O$, a series of manganese alkylphosphonates $(Mn(O_3PC_nH_{2n+1})H_2O$ $n = 3 - 6)$ and manganese phenylphosphonate $(Mn(O_3PC_6H_5)H_2O)$ reveal that while the magnetic structures are similar among these materials, differences can be detected using AFMR. Since the superexchange pathways in these materials are nearly identical, the observed differences in the magnetic exchange are thought to arise from electronic perturbations caused by the phosphate/phosphonate substituents. It was observed that the symmetric exchange

field decreased as the electron donating ability of the substituent decreased, following the trend $H_E(\text{KMnPO}_4 \cdot \text{H}_2\text{O}) > H_E(\text{Mn}(\text{O}_3\text{PC}_n\text{H}_{2n+1})\text{H}_2\text{O}) > H_E(\text{Mn}(\text{O}_3\text{PC}_6\text{H}_5)\text{H}_2\text{O})$. Analysis of the frequency and field dependence of the AFMR signals revealed that the canting angle, β, for these materials was $0.7\text{-}0.9 \pm 0.2^\circ$. In addition, the anisotropy of the magnetic interactions is determined from analysis of the frequency and field dependence of the AFMR signals. Further, it is shown that the values of the exchange field determined from the mean molecular field formulation of AFMR, can be related to the value of the spin-Hamiltonian superexchange constant, J, determined from magnetic susceptibility measurements.

CHAPTER 5
APPLICATION OF PHOSPHORUS-31 SOLID-STATE MAGIC ANGLE SPINNING NUCLEAR MAGNETIC RESONANCE TO THE STUDY OF OCTADECYLPHOSPHONATE LANGMUIR-BLODGETT FILMS

Introduction

Nuclear magnetic resonance (NMR) is a very powerful spectroscopic tool that can be used to gain an understanding of the structure and/or dynamics of a particular substance, and it has found applications in fields ranging from structural biology to low temperature physics.[170] However, NMR spectroscopy has rarely been used to study the molecular structure and organization of Langmuir-Blodgett (LB) films. This lack of use results predominantly from two factors. Firstly, LB films are typically transferred onto flat surfaces of low surface area where the number of nuclei per monolayer (ca $10^{15}/ cm^2$) is well below the conventional NMR detection limit. Secondly, even when multilayer samples are prepared ($\sim10^{18}$ molecules / sample), ^1H and ^{13}C investigations (which can provide information about the organization and mobility of the alkyl chains) are difficult since the polymeric substrates onto which the LB films are transferred introduce large ^1H and ^{13}C background signals that obscure the interpretation of the NMR spectra of these spin species.

For example, Towns and co-workers[171] investigated the structure of a 1000 layer LB film formed from the octadecylester of pentadec-1-ene-maleic anhydride copolymer by ^1H wideline and ^{13}C cross polarization (CP) magic angle spinning (MAS) NMR spectroscopy. The polymeric LB film was deposited onto a polycarbonate flexible substrate for ease of packing into an NMR rotor for MAS experiments. The sample was tightly rolled in a spiral fashion and inserted into the circlular rotor. The results showed that solid-state NMR is a practical tool for obtaining

147

information about the molecular dynamic properties of LB films. In particular, by comparing the ^{1}H wideline NMR spectrum of the LB film to spectra of the bare substrate and the bulk polymer, it was inferred that in the multilayer sample the chains were considerably less mobile than in the bulk polymers. However, the relaxation properties obtained from the wideline ^{1}H NMR are an average over all of the different types of hydrogens in the sample.[172] Hence, only average dynamic properties can be probed without resolution of the specific groups in the LB films. This type of information can be obtained with high resolution solid-state ^{1}H NMR studies employing multilple pulse sequences.[173] Furthermore, additional information about the film properties may have been obtained if it were possible to use a substrate that did not provide a ^{13}C and/or ^{1}H NMR signal that had spectral overlap with those of the LB films.

Other possible substrates that could be used for these types of experiments include silicon wafers and quartz or glass slides. However, one drawback of these substrates is their relative rigidity and the complication this imposes upon efficient packing of the NMR rotors for MAS experiments that can mitigate the sensitivity of the experiment. Some commonly used substrates for the deposition of LB films are summarized in Table 5-1. Some of the advantages and disadvantages of each are also listed. For wideline ^{1}H NMR spectra, the constraint of efficient packing could be overcome by the use of specifically designed flat coil probes that are designed to enhance the sensitivity of such an aligned sample.[170] These probes have been commonly used in studies of membrane bound proteins that are aligned in lipid bilayers between glass plates. A substrate such as mica might offer an ideal solution for efficient packing into an NMR rotor since after the film is transferred onto the substrate, the mica can be crushed into a powdered-like sample and then packed more efficiently into the rotors. Additionally, the mica substrate may be ideal for performing ^{13}C and ^{1}H NMR measurements.

However, here it is pointed out that for NMR studies of phosphorus-containing molecules, such as phospholipids and organophosphonic acids that are of interest as LB films,[174]

Table 5-1. List of Substrates for LB Film Depositions and Their Applicability for NMR Investigations.

Substrates	^{1}H Detection	^{13}C Detection	Oriented Samples	Filling Factors
Silicon wafers	X	X	X	O
Glass Slides	◉	X	X	O
Quartz Slides	◉	X	X	O
Mica (strips/crushed)	◉/◉	X/X	X/O	O/X
Polymeric Film	O	O	X	X

Key : X = good, O = not so good, ◉ = may contain some hydroxy-protons that could interfere with ^{1}H wideline detections.

^{31}P NMR offers several important advantages over ^{13}C and ^{1}H detections. Solid-state ^{31}P MAS NMR investigations of these types of multilayer LB films can take advantage of the relatively high sensitivity and almost 100 % natural abundance of the phosphorus-31 nuclei along with the absence of any background signals arising from polymeric substrates.

Presented in this chapter are the results of the first solid-state ^{31}P MAS NMR investigations of multilayer Langmuir-Blodgett films. The results demonstrate that this is a useful and practical technique for characterizing the structure and organization of organophosphonic acid LB films. Specifically, both quantitative and qualitative information about the structure and organization of the phosphonate groups in octadecylphosphonic acid LB films is obtained. In view of the success of these studies, it is suggested that ^{31}P MAS NMR could be more generally applicable to investigating the structure of other layer-by-layer constructs. Additionally, the results confirm that the 2D continuous lattice structure of the lanthanum octadecylphosphonate LB film[37,111] is isostructural with that of the analogous lanthanum butylphosphonate solid-state material.
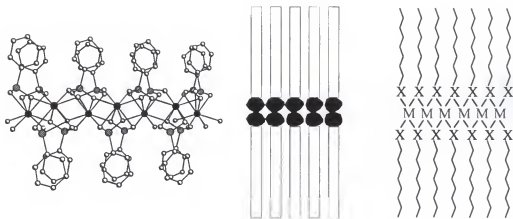
Figure 5-1. Comparison of the organic/inorganic layered structures of the solid-state metal phosphonates to metal phosphonate LB films. **(left)** The layered metal phosphonate structure of LaH(O$_3$PC$_6$H$_5$)$_2$. The crystallographic data are taken from ref. 37. Key: oxygen and carbon, open cirlces; phosphorus, hatched circles; and lanthanum, black circles. **(center)** Representation of a y-type LB film. **(right)** Metal phosphonate LB film where the polar region contains a 2D inorganic continuous lattice.

Metal phosphonates form a class of layered mixed organic/inorganic materials that contain 2D inorganic continuous lattice networks that are separated by layers of the organophosphonate substituents (Figure 5-1).[11,12] Interest in these materials includes their use as sorbents and intercalation hosts,[11,155] while thin films of functionalized metal organophosphonates have been explored for their potential optical,[26,27] nonlinear optical[102,103] and electronic properties.[104,105] In addition, metal phosphonates have been studied as models for 2D magnetic systems.[22,23] Langmuir-Blodgett (LB) techniques have been used to prepare single layers of these solid-state materials,[5,7,10,106,111] and multilayer films can be constructed where one layer of the metal phosphonate is formed during each deposition cycle.

Phosphorus - 31 NMR has previously been used to study metal phosphonates.[95,175-181] Several metal phosphonate 2D lattice structures are known,[11] and ^{31}P NMR spectroscopy has

been used to probe the in-plane metal-phosphonate bonding geometry in some solid-state examples.[177,181] Specifically, the isotropic chemical shift, chemical shift anisotropy and asymmetry values have been shown to correlate with different metal-oxygen-phosphorus in-plane connectivity schemes in a series of zinc organophosphonates. Furthermore, previous ^{31}P NMR investigations have identified the metal-oxygen-phosphorus bonding mode of organophosphonic acids self-adsorbed onto high surface-area metal oxide particles.[95,175,176] In what follows, it is demonstrate that ^{31}P NMR can also be employed to study the in-plane metal-oxygen-phosphorus bonding geometry of multilayer metal phosphonate LB films. These are the first NMR results to unambiguously characterize the structure of a LB film.

Experimental Details

Sample Preparation

Two lanthanum octadecylphosphonate (ODP) LB films consisting of 35-bilayers and 125-bilayers were prepared by deposition onto a Mylar (DuPont, DE) substrate. A 125-bilayer octadecylphosphonic acid (ODPA) LB film deposited from a 0.5 mM Cd^{2+} subphase was also prepared. Table 5-2 lists the deposition conditions used in each case. For each sample, the LB film was deposited onto a Mylar substrate of dimensions 60 mm x 40 mm. Prior to use, the Mylar substrate was cleaned by sonication in ethanol for 20 minutes, then sonicated in nanopure water for 10 minutes, dried by a stream of nitrogen gas and then dried in a 40° C oven overnight. For all depositions, each transfer ratio was within the range of 0.95 - 1.05.

Materials Used

All chemicals were purchased and used as supplied. Octadecylphosphonic acid (ODPA, $C_{18}H_{37}PO_3H_2$, 98%) was purchased from Ted Pella (Ward Hill, NJ), butylphosphonic acid ($C_4H_9PO_3H_2$, 99%) was purchased from Fluka (Buchs, Switzerland), and ethylphosphonic acid

$(C_2H_5PO_3H_2, 99\%)$ was purchased from Aldrich (Milwalkee, WI). $La(NO_3)_3 \cdot 6H_2O$ (99%) was purchased from Alfa Aesar (Ward Hill, MA), and $CdCl_2 \cdot 5/2H_2O$ (99.7%) was purchased from Fisher Scientific (Pittsburgh, PA). A Barnstead NANOpure purification system produced water with an average resistivity of 18 MΩ cm for all experiments. The powdered solid-state metal phosphonates, lanthanum butylphosphonate and cadmium ethylphosphonate, were prepared by standard literature procedures for growth of metal organophosphonates.[16,29,32]

Instrumentation Used

The LB experiments were performed using a KSV 3000 Instruments (Stratford, CT) system modified to operate with hydrophobic double barriers on a home-made Teflon trough with a surface area of 960 cm^2 (12.8 cm x 75 cm), respectively. The surface pressure was measured with a platinum Wilhelmy plate suspended from a KSV microbalance.

The static and MAS NMR phosphorus-31 spectra were acquired at 11.74 T using a Varian 500 MHz Unity Spectrometer equipped with a Jakobsen type 4 mm double resonance MAS probe with ^1H decoupling. All spectra are referenced to 85% phosphoric acid. MAS spectra were obtained at spinning rates indicated in the figures and figure captions, each with a recycle delay of 30 s. For cross-polarization (CP) experiments, the parameters were optimized for the analogous powders. A list of all parameters used for the NMR experiments is given in Appendix-C. For the NMR spectra of LB films, the number of transients acquired ranges from 5000-10,000, whereas 16-64 transients were accumulated to obtain the spectra of the solids. The LB film samples were cut into thin strips and packed into 0.5 mm outer diameter silicon nitride rotors as shown in Figure 5-2. The total area of film used that easily fit within the rotors was an area of approximately 50 mm x 35 mm.
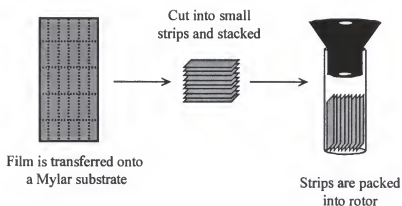
Figure 5-2. Packing of LB film samples into the NMR rotors.

Table 5-2. Deposition Conditions Used to Prepare the La ODP and ODPA LB Film Samples for NMR Investigations.

LB Film Sample	Subphase Composition	Subphase pH[a]	Target Pressure (mN/m)	Deposition Speed	
				Down-stroke (mm/min)	Up-stroke (mm/min)
La ODP[b]	0.5 mM La(NO$_3$)$_3$·6H$_2$O	2.55-2.65	22	8	3
ODPA[c]	0.5 mM CdCl$_2$·5/2H$_2$O	3.0-3.25	25	10	8

[a] The subphase pH was adjusted with a 0.12 M HCl solution. [b] Both La ODP LB film samples were prepared with the sample deposition conditions. [c] The ODPA LB film was prepared by continuous depositions whereas the La ODP films are deposited one bilayer at a time.

Results and Discussion

Lanthanum Octadecylphosphonate LB Film

Figure 5-3 shows ^{31}P MAS NMR spectra of a 35-bilayer and a 125-bilayer La octadecylphosphonate (ODP) LB film. Note that in the spectra of both samples, only one NMR signal is detected at a shift of 24.8 ppm. The presence of only one relatively narrow signal reflects a single structural type within the multilayer sample. Previously, others have used ^{31}P MAS NMR to study the metal-oxygen-phosphorus bonding motif in polycrystalline metal phosphonate solids[177-181] and in organophosphonic acids adsorbed onto high surface area particles.[95,175,176] From these earlier reports it is known that the isotropic shift and the chemical shift anisotropy can be related to the type of metal phosphonate bonding geometry. As is evident from Figure 5-3, this isotropic shift, δ_{iso} = 24.8 ppm, occurs at the same value, within error, as the shift obtained from a sample of polycrystalline lanthanum butylphosphonte, and indicates that the structure in the LB film is analogous to that of the powdered solid. The slight broadening of the resonance line in the film suggests a distribution of geometries that presumably results from strain at the domain boundaries in the film. This strain is likely since atomic force microscopy results[10] show that the metal phosphonate LB films consist of structurally ordered domains no larger than 700 Å, which is considerably smaller than the average particle size of the metal phosphonate powders.

In addition, the slower spinning spectrum of the 125-bilayer film (Figure 5-4) displays a well-defined spinning side band pattern analogous to that of the solid-state polycrystalline material. Slight differences in the intensities of the spinning sidebands of the solid and film are apparent and result from the partial orientation of the LB sample. A detailed account of the fitting of a spinning sideband pattern of a partially oriented system will be the focus of some future work.
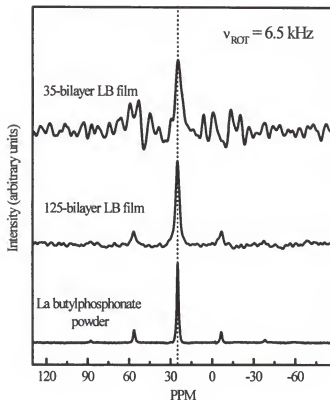
Figure 5-3. MAS ^{31}P NMR spectra of La ODP LB films and of lanthanum butylphosphonate powder. The spectra of the films contain 5000 transients, whereas the spectrum of the powder contains 32 transients. The isotropic shift occurs at 24.5 ppm in each case. The dotted line is a guide for the eyes. The other peaks are the spinning sidebands. In each case, the sample was spun at a rate of 6.5 kHz.

The 24.8 ppm shift in the La ODP LB film can be compared to that of solid octadecylphosphonic acid (ODPA) which occurs at 31.5 ppm (Figure 5-5).[175] The absence of any detectable peak at 31.5 ppm in the spectrum of the films and because the signal: noise ratio in the spectrum of the La ODP LB film is 33:1, it can be estimated that there are less than 3% free acid sites present in the 125-bilayer sample.

These results show that the in-plane metal phosphonate structure of the La ODP LB film is isostructural with that of polycrystalline lanthanum butylphosphonate, and that solid-state ^{31}P MAS NMR can be used to determine whether or not the metal phosphonate lattice structure has formed within the LB architecture.
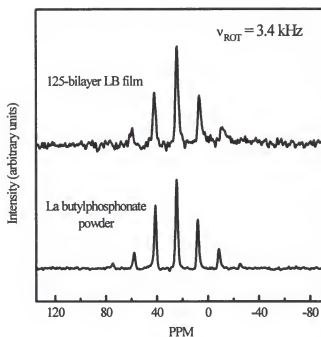
Figure 5-4. MAS ^{31}P NMR spectra of the 125-bilayer La ODP LB film and lanthanum butylphosphonate each at a spinning rate of 3.4 kHz.
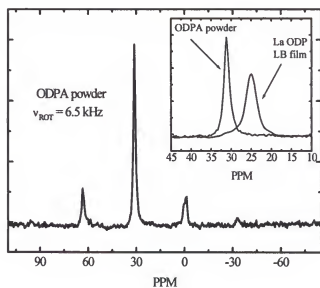
Figure 5-5. MAS ^{31}P NMR spectrum of octadecylphosphonic acid powder. The inset shows a comparison of the isotropic peaks for ODPA and the 125-bilayer La ODP LB film.

Octadecylphosphonate LB Film

Octadecylphosphonic acid (ODPA, $C_{17}H_{37}PO(OH)_2$) is known to form quality Langmuir monolayers,[131] but, on its own, it does not transfer well, nor does it transfer with monovalent ions present in the subphase. However, it is well known that many LB films are stabilized by the presence of divalent metal ions incorporated into the films,[83] and for the 125-bilayer ODPA LB film prepared for these studies, a 0.5 mM Cd^{2+} subphase was used to help improve film stability. Previous work shows that at a subphase of pH 4.5-5.3 the $Cd(O_3PR)H_2O$ cadmium phosphonate continuous lattice structure crystallizes within the ODP LB films.[10] For this sample, the subphase was adjusted to pH 2.8-3.1, which is lower than that required to form the 2D continuous lattice. Hence, for this sample, the cadmium ions are incorporated into the film through ion pairing with the $C_{18}H_{37}PO_3H^-$ and/or $C_{18}H_{37}PO_3^{2-}$ groups, but not as the 2D continuous inorganic lattice.

The preparation of this film had two purposes. Firstly, this film was prepared to demonstrate the generality of the NMR technique for investigating the structure of LB films containing phosphorus, and not necessarily for demonstrating the formation of continuous lattice metal phosphonate LB films. This first point is important, otherwise the NMR investigations may be limited to only the metal phosphonate LB systems which are unique because of their relatively extended 2D continuous lattice structures. Secondly, from other characterization methods, it is known that with the conditions used to prepare the ODPA film, the cadmium ions are included in the film, but not as the $Cd(O_3PR)H_2O$ phase. However, from infrared analyses (Figure 5-6), the nature of the phosphonic acid structure is not clear, and it was hoped that the NMR investigations could be used to determine the structure of this type of film.

Figure 5-7 shows the ^{31}P MAS NMR spectrum of the 125-bilayer ODPA LB film with two resolved peaks, one at δ_{iso} = 28.3 ppm and the other at δ_{iso} = 22.5 ppm. The signal at 28.3 ppm integrates to approximately 65% of the film structure and can be assigned to the free acid
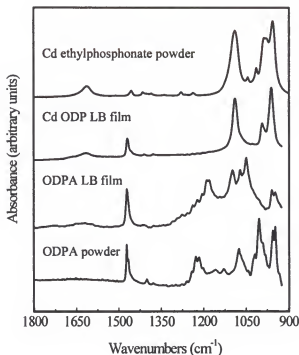
Figure 5-6. IR spectra of cadmium ethylphosphonate powder, cadmium octadecylphosphonate LB film, ODPA LB film (with cadmium ions in the subphase at pH 2.8-3.1) and solid ODPA. The IR spectrum of the ODPA LB film does not resemble the spectrum of the Cd ethylphosphonate solid or the Cd ODP LB film, but rather has some similarities to the spectrum of ODPA. From comparison of the IR spectra, it is difficult to determine the structure of the phosphonate groups in this ODPA LB film.

form of ODPA.[175] The isotropic shift of the second signal occurs at δ_{iso} = 22.5 ppm and corresponds to dibasic octadecylphosphonic acid weakly interacting with Cd^{2+} ions which are incorporated into the film for charge-stabilization. The stronger signal at 28.3 ppm is slightly shifted from δ_{iso} = 31.5 ppm of solid ODPA (Figure 5-5) due to weak associations between the free phosphonic acid and nearby Cd^{2+} ions. The assignments for both of these signals are based upon comparison to sodium octadecylphosphonates, where for the mono- and disodium salts, the corresponding ^{31}P NMR resonances are shifted up-field from the free acid form of ODPA and occur at 26.5 and 23.8 ppm, respectively.[176] Both ^{31}P NMR resonances of the ODPA LB film
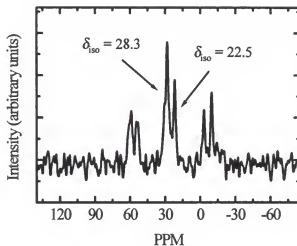
Figure 5-7. MAS ^{31}P NMR spectrum of a 125-bilayer ODPA LB film prepared on a 0.5 mM Cd^{2+} subphase at pH 2.8-3.1. The spectrum was acquired with a spinning rate of 6.5 kHz and 8000 transients were accumulated.
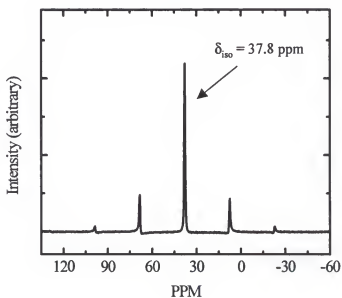
Figure 5-8. MAS ^{31}P NMR spectrum of cadmium ethylphosphonate powder, $Cd(O_3PC_2H_4)H_2O$. The spectrum was acquired at a spinning rate of 6.8 kHz and consists of 16 transients.

differ from δ_{iso} = 37.8 ppm found for a polycrystalline sample of Cd(O$_3$PC$_2$H$_4$)H$_2$O (Figure 5-8), showing clearly that the inorganic continuous lattice is not formed. Instead, the film contains cadmium ions that are incorporated in an ion-pairing fashion when prepared under these conditions.

Interestingly, the NMR results provide an answer to the problem of structural organization of this type of organophosphonate LB film. The transferred film contains both the free phosphonic acid sites and dibasic phosphonate ions that are paired to Cd^{2+} ions. The result is not what may intuitively be expected, but it is not unreasonable since the LB film is a condensed phase and disproportionation of the phophonic acid group is possible.

Generality of the NMR Technique

These results demonstrate that it is possible to obtain quality ^{31}P MAS NMR spectra of multilayer LB films. In addition, by comparing the spectra of the films with the analogous solid state materials, the in-plane structure of the LB film can be determined. Based on the cross-sectional area of the organophosphonates in the LaH(O$_3$PR)$_2$ structure of 24 Å^2/molecule,[12,29] it is estimated that the 35-bilayer and both 125-bilayer samples contain 1.0 x 10^{18} and 3.5 x 10^{18} phosphorus-31 nuclei, respectively. Given the signal to noise ratio of the spectra in Fig. 5-3, a lower detection limit (ie signal to noise of 2:1) of 2.0 x 10^{17} spins (or 5 bilayers) can be established under the present conditions, keeping in mind that efficient packing of the rotor is an important parameter that can severely affect this limit. Usually the detection limit can be improved by cross-polarization (CP) techniques.[172] Figure 5-9 compares the ^{31}P MAS NMR spectra acquired from a sample of cadmium ethylphosphonate powder, with and without CP. A total enhancement of approximately 3 is obtained, and an enhancement factor of 4 is obtained for a powdered sample of lanthanum butylphosphonate. Figure 5-10 shows the ^{31}P CP/MAS NMR spectra from the 125-bilayer La ODP LB film acquired at two different spinning rates.
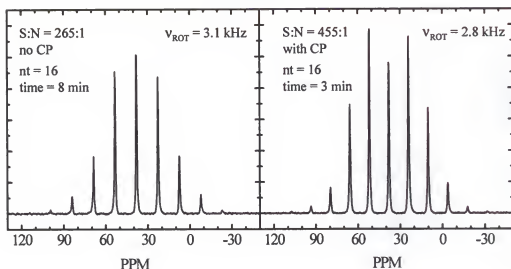
Figrue 5-9. MAS ^{31}P NMR spectra of cadmium ethylphosphonate taken without (left) and with (right) cross polarization (CP). The slower spinning speed in the spectrum acquired with CP accounts for the observed difference in the relative heights of the spinning side band patterns in the two spectra. An overall signal enhancement of 2.8 is obtained with CP.
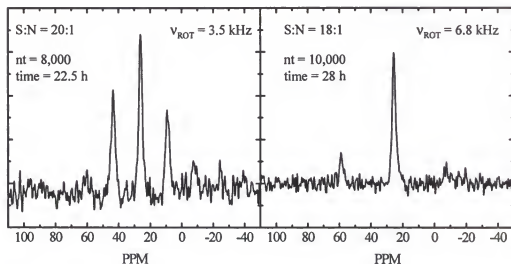
Figure 5-10. MAS ^{31}P Cross-polarized (CP) spectra of the 125-bilayer La ODP LB film acquired with spinning rates of 3.5 kHz (left) and 6.8 kHz (right). The CP spectral parameters used were optimized from a polycrystalline lanthanum butylphosphonate sample (Appendix – C).

Comparison of the signal to noise ratios of these spectra (approximately 20:1 in each case) to those of the same film acquired without cross-polarization (approximately 33:1 and 26:1 at 6.5 and 3.4 kHz, respectively) and accounting for differences in the total acquisition time shows that for the La ODP LB film there is essentially no signal enhancement with CP. The lack of significant enhancement of the signals in the LB films with cross-polarization is probably due to the semi-solid nature, or in other words, a greater mobility of the alkyl chains within the films.

However, the detection limit could be further reduced by obtaining the spectra at higher field, because the signal to noise ratio is proportional to $B_o^{(11/4)}$.[172] Given these factors, a conservative estimate is that ^{31}P MAS NMR with signal to noise of 8:1 of LB films containing 5 bilayers is possible (assuming a 800 MHz spectrometer). Hence, this technique may find future applications as a general tool for the structural characterization of low surface area thin films containing phosphorus, such as other phosphonate or phospholipid LB films, as well as some spontaneously absorbed multilayer films.[12,100]

Conclusions

In conclusion, these results demonstrate that NMR can be used to study structure in LB and related thin films, and more specifically that this technique provides a way of characterizing the structure of phosphorus containing LB films. Other efforts to use NMR to characterize thin films have been unsuccessful, but our efforts suceeded by using ^{31}P MAS NMR which takes advantage of both the relatively high NMR sensitivity of phosphorus-31 and the lack of any background signals from the substrate that might complicate the interpretation of the spectra. By comparing the spectra of the films with those of the analogous solid state materials, a definitive determination of the LB film structure can be made. Examples of other systems that might benefit from similar studies include other phosphonate or phospholipid LB films, as well as some spontaneously assembled monolayer and multilayer films.

APPLICATION OF DEUTERIUM QUADRUPOLE ECHO SOLID-STATE NUCLEAR
MAGENTIC RESONANCE TO THE STUDY OF PHENYL RING DYNAMICS IN METAL
PHOSPHONATE SOLIDS

Introduction

Deuterium quadrupole echo nuclear magnetic resonance (^{2}H NMR) is a powerful
technique for the study of dynamical processes that occur on the time scale of milliseconds to tens
of microseconds, and during the last 10-15 years, it has emerged as a general tool for studies of
motion in solid, semisolid and ordered phases.[182] Although phenyl ring dynamics were originally
attributed to biological activity, the observation of phenyl ring flips in crystalline amino acids,
and in polymers / biopolymers suggests that the motion is not necessarily related to biological
activity, but rather the motion reflects the local structure of the material.[183] In the work presented
here, ^{2}H quadrupole echo NMR is applied to the study of phenyl ring dynamics in a series of
known solid-state metal phosphonates. These systems are of interest because they form
alternating layers of organic and inorganic components. Solid-state materials, where alternating
organic and inorganic components each contribute specific functionality, can potentially impact
areas such as catalysis, optics, magnetics, and conducting and superconducting devices.[11,13,155]
Frequently, these mixed organic/inorganic materials form layered or porous three-dimensional
structures.[11] In efforts to better understand how the choice of metal ions could affect the
subsequent packing of the organic groups, deuterium NMR studies have been performed on two
structurally similar metal phosphonate compounds, cadmium phenylphosphonate and magnesium
phenyphosphonate. Figure 6-1 shows a cross-sectional view of the magnesium
phenylphosphonate structure, and the lattice parameters for both materials are given in Table 6-1.

The series of divalent metal phenylphosphonates, $M^{II}(O_3PC_6H_5)H_2O$ M = Mn, Mg, Zn, Cd, which crystallize in the same space group,[16] provide systems where structural differences are small, but where the physical properties of the solids can be immensely affected by the identity of the metal ion. In the present work, deuterated samples of both cadmium phenylphosphonate (Cd-*d*PP) and magnesium phenylphosphonate (Mg-*d*PP), have been prepared. Motion of the phenyl groups has been characterized by measuring the deuterium quadrupole echo NMR spectra of these samples at a series of temperatures. For Cd-*d*PP and Mg-*d*PP, the phenyl ring motion is found to vary from 10^3-10^7 Hz over the temperature range of 150 – 300 K, making ^{2}H NMR line shape analysis a suitable technique for studying the molecular motion of the phenyl rings in this system. Line shape simulations of experimental spectra show that the phenyl ring motion in both samples can be described by discrete 180° flips around the C_{2v} (C_1-C_4) axis. A linear relationship between 1/T and ln(rate) is observed, and the activation energy (E_a) of the flipping process for both samples is determined. Different E_a values are experimentally obtained for the two materials, which indicates that although these samples have similar crystal structures, slight changes in the size of the metal ions affect the dynamics of the organic substituents in these compounds.

Experimental Section

Sample Preparation

Per-deuterated phenylphosphonic acid ($C_6D_5PO_3D_2$) was prepared by use of the nickel catalyzed Arbuzov reaction starting with d_5-bromobenzene (25g , Aldrich, WI) and hydrolyzing with 37% DCl/D_2O (50ml, Aldrich, WI).[162] Perdeuterated cadmium phenylphosphonate and magnesium phenylphosphonate were prepared by standard literature procedures,[11,12] where hydrogenated water was used as the solvent. A typical procedure for preparing powder samples consists of mixing equimolar amounts of aqueous solutions of the organo-phosphonic acid and

the corresponding metal salt ($Mg(NO_3)_2 \cdot 6H_2O$ or $CdCl_2 \cdot 5/2H_2O$), and adjusting to the proper pH until precipitation is complete. To improve upon the crystallinity of the powder samples, solutions are warmed to 80 - 85°C and allowed to stir for a few days. Samples are then collected, washed, and dried. The final products were of composition $Cd(O_3PC_6D_5)H_2O$ and $Mg(O_3PC_6D_5)H_2O$. Characterization of the compounds consisted of both elemental combustion analysis and IR spectroscopy of each prepared as a KBr pellet.
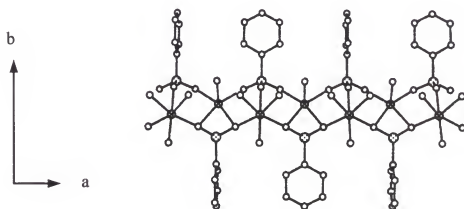
Figure 6-1 Cross sectional view of the structure of Mg phenylphosphonate (crystallographic data are taken from ref. 16).

Table 6-1. Lattice Parameters for Magnesium and Cadmium Phenyl Phosphonate.

Sample	Space group	a (Å)	b (Å)	c (Å)
Cd phenylphosphonate[a]	$Pmn2_1$	5.860(4)	14.459(14)	5.054(3)
Mg phenylphosphonate[b]	$Pmn2_1$	5.61(3)	14.28(7)	4.82(3)

[a] Parameters are taken from ref. 32. [b] Parameters are taken from ref. 16 and 28.

Deuterium Quadrupole Echo NMR Experimental Conditions

Deuterium quadrupole echo experiments can be performed on an NMR instrument capable of high speed acquisition (1 MHz), short receiver dead times, and high power rf pulses. For determining E_a values, variable temperature capabilities are also required.[184] A typical ^{2}H quadrupole echo sequence (Appedix-C) employs 90° pulses of duration of 1.5 -2.0 µs, with interpulse delays ranging between 30 -150 µs and recycle delay times varying from 0.5 –100's of seconds depending upon the longest spin lattice relaxation time (T_1).[182,184] Phase cycling is often employed to increase the quality of the spectra, as this helps remove the dc offset, probe ringing, and quadrature echo artifacts. The quadrupole echo sequence is used when performing ^{2}H solid state NMR because the relatively short spin-spin relaxation lifetime (T_2) causes the signal to decay very rapidly. Instrumental limitations such as pulse breakthrough into the receiver and probe ringing can distort the first few points of the free induction decay, thereby, severely distorting the spectrum. The echo sequence allows collection of the signal at a time sufficiently long enough after the second pulse to ensure that all instrumental "ringing" has ceased. It is important to note that collection of the signal from the echo overcomes this instrumental distortion, but it can also introduce other artifacts due to echo-attenuation factors.[182,185]

The deuterium quadrupole echo NMR spectra of cadmium d_5-phenylphosphonate (Cd-dPP) and of magnesium d_5-phenylphosphonate (Mg-dPP) were recorded at 45.6 MHz on a 300 MHz Techmag spectrometer with a homebuilt rf section (homodyne design) and a homebuilt single-channel transmission-line probe. The pulses were amplified to 600 W using an American Microwave Technologies, Inc. 1 kW broadband amplifier. The conventional quadrupole echo pulse sequence[182] $[(90°)_\phi - \tau - (90°)_{\phi + \pi/2} - \tau' - \text{acquire} - \text{recycle}]$ was used with a 90° pulse duration of 1.5 µs. Two separate sets of spectra were recorded with echo delays of $\tau = 60$ and 100 µs. Because of instrument ring-down effects, a minimum τ value to obtain undistorted spectra was 60 µs for these samples. Since the spectra acquired at these two τ values are quite

similar, data are given only for $\tau = 100$ μs. A recycle delay of 60 s was programmed for all temperatures. Phase cycling was employed to eliminate quadrature phase errors. Spectra consist of 1024 transients unless stated otherwise. The temperature was controlled by an Oxford ITC 503 temperature controller and a CF1200 continuous flow cryostat (T = 1.5 – 300 K). Liquid nitrogen was used as the cryogen.

Lineshape Simulations

The quadrupole echo ^{2}H NMR spectra were simulated using the FORTRAN based program MXQET developed by R.L. Vold, R.R. Vold and co-workers.[186] This program accounts for various spectral distortions, including effects due to finite pulse-widths.[182,186] The spectral simulations were obtained by Fourier transformation of the calculated echo decay where both Gaussian and Lorentzian apodizations were applied before Fourier transformation. Typical program input consists of a hypothesized mechanism of motion (180° flips) and the geometry of the molecule (i.e. specify water versus a phenyl ring) along with the values of the quadrupole coupling constant and the asymmetry parameters for each unique deuteron, as well as the experimental parameters of the quadrupole echo pulse sequence. A sample input file is provided in Appendix-C. Due to the inability of the simplex algorithm to converge to a good fit between the experimental and calculated spectrum, fits to the data had to be performed by visually comparing the computer generated line shape to the experimental spectra while iteratively adjusting the rate and the quadrupole coupling constant.

Background Information

Deuterium Quadrupole Echo NMR Spectroscopy

Contrary to liquid-state NMR spectroscopy, where the quadrupole interaction is averaged to zero by fast molecular tumbling, in solid-state NMR, where molecular motion is restricted, the

quadrupole interaction does not vanish but instead dominates the features of the ^{2}H NMR spectrum.[187] Because ^{2}H is a spin-1 nucleus, the presence of a magnetic field generates three Zeeman nuclear spin states. When the quadrupole electric moment of the deuterium atom interacts with the electric field gradient at the nucleus, often from distortions of the electron clouds, the Zeeman energy states become perturbed. The quadrupole coupling can be treated as a perturbation of the Zeeman energy levels.[172,187] The energy (E_m) of these levels can be written as:

$$E_m^{(p)} = E_m^{(0)} + E_m^{(1)} + E_m^{(2)} + \ldots \tag{6-1}$$

where $E_m^{(p)}$ represents the pth order perturbation energy. The first order perturbation of the three Zeeman states generates two non-degenerate $\Delta m = \pm 1$ transitions whose frequencies are symmetric about the ^{2}H Larmor frequency. (Figure 6-2). The energy of each transitions is given by:

$$\Delta E = \gamma \hbar^2 H_0 \pm 3/8 e^2 q Q (3\mu^2 - 1 - \eta(1 - \mu^2)\cos 2\phi) \tag{6-2}$$
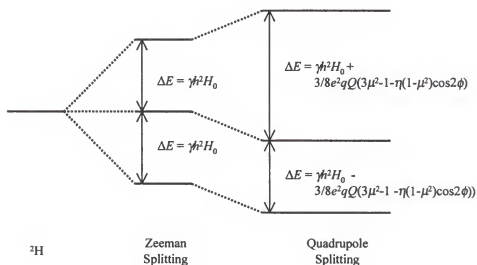
Figure 6-2. Energy level diagram for $\Delta m \pm 1$ transitions for a deuterium nucleus with Zeeman and quadrupole splittings. Variables are defined in the text.

where h is Plank's constant, eq is the electric field gradient, Q is the quadrupole moment, $\mu = \cos \theta$, where θ is the angle between the z-principal axis of the electric field gradient (efg) tensor (V) and the direction of the applied magnetic field, and $\eta = (|v_{YY}| - |v_{XX}|)/|v_{ZZ}|$ is the asymmetry parameter where v_{ii} are the diagonal elements of V in its principle axis system. The Euler angles θ and ϕ specify the orientation of the efg tensor with respect to the applied magnetic field, with ϕ locating the efg tensor in the xy-plane. In most chemical bonding environments, the ^2H nucleus has the useful characteristic that its quadrupole moment leads to a splitting that is much larger than the broadening of the line width due to dipolar interactions. Yet, the splitting is still small enough that it requires only a moderate bandwidth for excitation and digitization of the spectrum. (*Note*: The ^2H quadrupole moment is relatively small (100-200 kHz) compared to any other quadrupolar nucleus, including ^{14}N, the next smallest, which is > 2-4 MHz.) Also, note that the quadrupole splitting is not a function of the applied field. Thus, the splittings and fine structure of the deuterium powder patters give structural and chemical information about the solid environment under study.[172,187,188]

In a single crystal, the ^2H NMR spectrum appears as a symmetric sharp doublet for each crystallographically unique deuteron (Figure 6-3), where the splitting is determined by the quadrupolar coupling constant and the crystal orientation with respect to the applied magnetic field. This splitting given by:

$$\Delta(\Delta v) = 3/4\chi(3\mu^2-1-\eta(1-\mu^2)\cos(2\phi)) \qquad (6-3)$$

where $\chi = eVQ/h$ is the quadrupole coupling constant. In a polycrystalline sample, where all orientations of the crystallites are represented equally, the ^2H spectrum takes on an envelope shape that represents the sum of the transitions arising from all possible values of θ and ϕ. In general, the ^2H NMR powder pattern line shapes are symmetric around the Larmor frequency, with three pairs of distinctive features:[187] the steps, the shoulders, and the singularities; which are
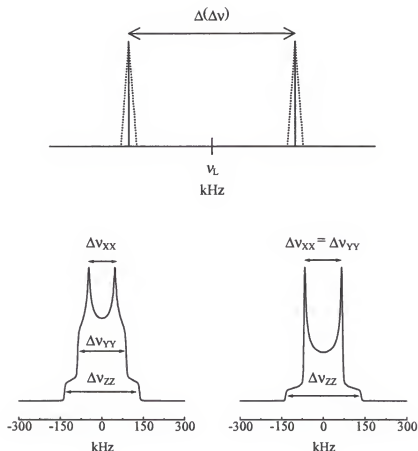
Figure 6-3. (top) Idealized ^{2}H quadrupole echo spectrum of one unique deuterium atom in a single crystal. (bottom) ^{2}H quadrupole spectra for a polycrystalline sample with less than axial (left) and axial symmetry (right).

shown in Figure 6-3. The separations between these features are proportional to the magnitude of principal components of the efg tensor, Vxx, Vyy, and Vzz, and are given by:

$$\Delta v_{ZZ} = v_Q \qquad \text{(steps)} \qquad (6\text{-}4)$$

$$\Delta v_{YY} = v_Q(1+\eta)/2 \qquad \text{(shoulders)} \qquad (6\text{-}5)$$

$$\Delta v_{XX} = v_Q(1-\eta)/2 \qquad \text{(singularities)} \qquad (6\text{-}6)$$

respectively, where here, $v_Q = 3\chi/2$ and η is the asymmetry parameter. In an axially symmetric system $\Delta v_{ZZ} > \Delta v_{YY} = \Delta v_{XX}$. In cases where axial symmetry is not present, it is conventional that

$\Delta v_{ZZ} > \Delta v_{YY} > \Delta v_{XX}$, and it is useful to define an asymmetry parameter η, where $\eta = (|V_{YY}| - |V_{XX}|)/|V_{ZZ}|$ with $0 < \eta < 1$.

Deuterium NMR Line Shape Analysis

The quadrupole coupling interaction, which dominates the line shapes of ^2H NMR spectra, is extremely sensitive to molecular motion.[182,187,189-192] This is because motions in the solid change the orientation of the efg tensor with respect to the applied magnetic field during acquisition of the NMR signal. When a ^2H nucleus undergoes a motion on an appropriate time scale, the ^2H NMR line shape is altered in a well defined manner, allowing detailed dynamical information to be elucidated from analysis of the NMR line shapes. This appropriate time scale is defined by the size of the quadrupole coupling constant and limits the line shape sensitivity to dynamical events that occur within 10^3 and 10^7 Hz.

The ^2H NMR line shape can easily be simulated,[186,193,194] and information about the rate and mechanism of the dynamic process can be extracted from the ^2H powder spectra in three ways. First, changes in the rates of motion produce dramatic effects in the appearance of the line shapes. Variation of the temperature provides a means of adjusting the rates of the dynamical processes and allows for a way of systematically studying these changes as a function of the temperature. Second, for motions occurring with rates on the order of 10^5-10^7 Hz, the quadrupole echo line shape shows a dependence on the pulse spacing,[186] thus allowing for further evidence to support a probable mechanism of motion. Third, echo attenuation studies[185,186] provide further evidence to help determine a possible mechanism of motion. Examples of motions which have been studied are methyl group rotations in lipid bilayers or in amino acids,[191,192] rotations of benzene or other planar structures,[186] flips of phenyl rings in amino acids/small peptides,[195-197] and polymers[183] and gauche-trans isomerizations in long chain bilayer structures.[191]

Molecular motions occurring in solids are grouped into three regimes: slow, fast, and intermediate.[185,190] Motions that occur on a time scale much longer than v_Q^{-1} (rates < 10^4 Hz) have minimal effects on the appearance of the NMR spectrum.[185,186] These spectra are termed static or rigid because there is essentially no reorientation of the efg tensor during the time scale of the experimental pulse sequence. Molecular motions occurring with rates less than 10^4 Hz typically cannot be studied by line shape analyses. However, their spectra can be used to calculate the static quadrupole coupling constant. For studies of motion in the slow-time regime, T_2 measurements and spin alignment techniques can be employed.[189,198]

Motions that occur on a time scale much shorter than v_Q^{-1} (rates > 10^7 Hz) are categorized in the fast regime.[185] The appearance of the spectral line shape is similar to that of the slow motion limit, with the frequencies between features being reduced. These motions are best represented by an averaged efg tensor and are characterized by order parameters which are related to the average symmetry and position of the efg tensor and molecular motion.[192] Line shapes in this regime do not significantly differ for varying mechanisms of motion; however, it is possible to make distinctions between large angular jumps and continuous diffusional motion.[195,196] For the fast motion limit, T_1 relaxation experiments can also provide important information about the mechanism of the motion.[191] Head group rotation and gauche-trans isomerizations in model lipid bilayer membranes are examples of systems studied that possess these fast molecular reorientations.[191]

Motions that occur on a time scale on the order of v_Q^{-1} (rates ranging from 10^5-10^7 Hz) fall into the intermediate regime.[182,185,186] The line shapes are not only dramatically affected by the rates of motions, but are affected differently for different types of motion. It is also on this time scale that the effects of both echo-attenuation and different pulse spacings are observed.[186] Fortunately, the rates of motions occurring in many solid systems fall within this range and lend themselves well to study by ^2H NMR techniques. In solids, motion of groups that contain ^2H

affect the orientation of deuterium's efg tensor, thus changing the precession frequency of those spins. Because the molecular correlation time is on the order of ν_Q^{-1}, the resulting efg tensor is a weighted average of the different positions occupied throughout the motion. Assuming a random distribution of particle orientation in a powdered sample, the different crystallite orientations will experience different changes in the principle components of the efg tensor. Now, the line shape is not only a summation of the crystallite orientations over θ and ϕ, but it is also a summation over a motionally "averaged" efg tensor. For a given mechanism of motion, it is possible to simulate the motional effect on the observed line shape. Many simulation programs now exist that allow for a parameterized fit to the experimental spectrum to determine the type of dynamical process occurring and the corresponding rate.[182,193,194] These simulation programs are quite sophisticated and account for experimental distortions due to finite pulse widths,[199] incomplete excitations,[200,201] and echo-attenuation factors[185] and for computational problems such as mathematical recursion of the FID in the intermediate motion regime.[200] The mechanisms which can be simulated range from simple two-site exchange (180° flips) to multi-site exchange and composite processes.[186] If spectra are collected as a function of temperature, and if the motional rates are determined by comparison to simulated spectra, then an Arrhenius plot can be constructed to determine the activation energy for that mode of motion. Careful inspection of the line shapes can also provide information about concurrent motions.

Results and Discussion

Dynamical Model

For the Mg-dPP and Cd-dPP compounds, a dynamic model for the phenyl ring motion as discrete 180° flips around the C_1-C_4 axis is assumed. Because the phenyl ring is directly bonded to the phosphonate P-atom that is incorporated into a continuous solid inorganic lattice, significant wobbling motion of the C_1-C_4 axis of the phenyl moiety is not expected at any
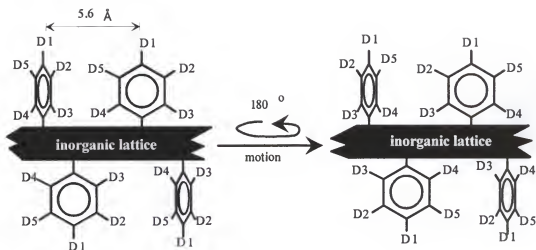
Figure 6-4. Representation of the phenyl ring flipping motion in the layered metal phenylphosphonate lattice.
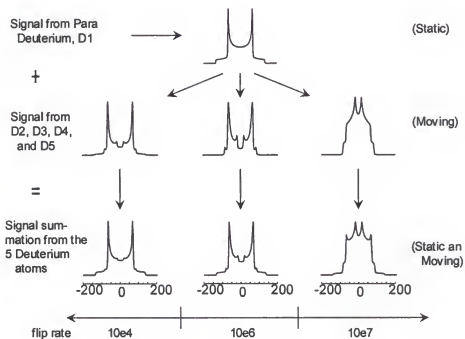
Figure 6-5. Simulated ^2H quadrupole echo NMR spectra for a phenyl ring undergoing $180°$ discrete flips about its C_1-C_4 axis for various flipping rates.

temperature. A schematic representation of the 180° ring flips within the galleries of the layered metal phosphonate architecture is shown in Figure 6-4. Because of the almost axial symmetry of the quadrupole coupling tensor which has its principal z-axis directed along the C-D bond, the para-deuteron, D_1, remains essentially stationary with respect to the flip-axis during this motion, whereas the ortho- and meta-dueterons rotate by 180° around the flip-axis. Here, the ortho- and meta-deuterons are considered to be magnetically equivalent, and simulations of the ^2H NMR line shapes are thus composed of a 1:4 ratio of one static (D_1) and four moving (D_2, D_3, D_4 and D_5) deuterium atoms. Figure 6-5 shows examples of the simulated line shapes, summated over all 5 deuterons, for this 2-site jump model for various phenyl ring flip rates.

Qudrupole Echo Deuterium NMR Spectra and Line Shape Analysis

Static limit

The ^2H quadrupole echo NMR spectra of Cd-dPP and Mg-dPP were each recorded at 150 K, and are shown in Figure 6-6. The two spectra are very similar, and both are well fit by simulations assuming the static limit ($\kappa < 10^3$ Hz) of motion for the flipping process with $\chi = e^2qQ/h = 181 \pm 1$ kHz and $\eta = 0.03 \pm 0.005$ for the ortho and meta deuterons and $\eta = 0.01 \pm 0.005$ for the para deuterium atom.

The intensity distribution in some of the recorded spectra is not symmetric around zero frequency, and none of the experimental spectra have been artificially symmetrized. The instrumental effects that can contribute to the asymmetry of the ^2H NMR powder patterns have been discussed by others.[182] In all cases, efforts were made to obtain the least distortion in the experimental spectra. In the most severely asymmetric spectra, the spectra were fit by using the half of the spectrum with positive frequency.
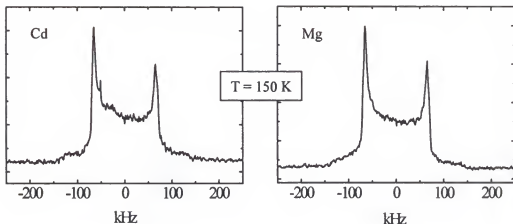
Figure 6-6. Static ^{2}H NMR spectra of Cd-dPP and Mg-dPP each recorded at 150 K.

The different η values for the two groups of phenyl ring deuterons is not surprising considering the electronic perturbations caused by the metal phosphonate continuous inorganic lattice. An aliphatic C-D EFG tensor is axially symmetric,[185] and distortion of the π-electron cloud of the benzene ring towards the metal phosphonate layer is not unrealistic and acts to restore axially symmetry to the para deuteron EFG tensor. Different η values for para and ortho/meta deuterons are also seen in perdeuterated benzoic acids.[202]

Intermediate regime

Figures 6-7 and 6-8 show the experimental ^{2}H NMR spectra acquired over the temperature range of 220 – 290 K for Cd-dPP and Mg-dPP, respectively. The silmulated spectra are given by the dotted lines. As stated earlier, simulated spectra are the summation of 1 static and 4 dynamic spectra corresponding to the para and ortho/meta deuterons, respectively and using a 2-site 180° discrete jump model. The ^{2}H NMR line shape for both samples changes as a
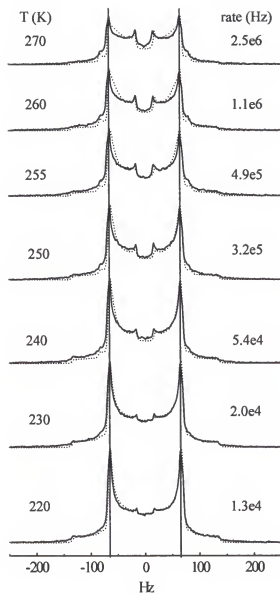
Figure 6-7. Quadrupole echo ^{2}H NMR spectra for cadmium d_5-phenylphosphonate as a function of temperature. The dotted line in each case is a fit to the spectra with the indicated rate constant. All other spectral parameters are listed in Table C-5. The solid lines are included as guides.
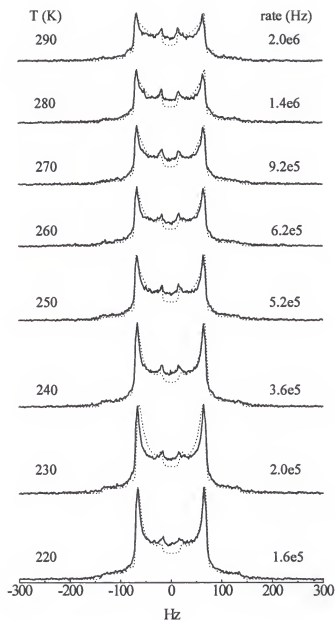
Figure 6-8. Quadrupole echo ^{2}H NMR spectra for magnesium d_5-phenylphosphonate as a function of temperature. The dotted line in each case is a fit to the spectra with the indicated rate constant. All other spectral parameters are listed in Table C-5.

function of temperature and clearly indicates that the phenyl rings are mobile within this temperature range. The NMR spectra of Cd-dPP coincide well with the simulated spectra and show that motion by discrete 180° flips is consistent with the experimental data. However, the fits to the Mg-dPP data are not as good, indicating that some other model of motion may be necessary to better fit the NMR line shapes of this system. The phenyl ring flipping rates in both samples vary from $10^3 - 10^7$ Hz over this temperature range. Assuming Arrhenious behavior for the temperature dependence of the rate (κ), the activation energies determined from plots of $\ln(\kappa(Hz))$ vs. $1/T(K)$, which are shown in Figure 6-9 for the 2-site jump model, are found to be $E_a = 3.7 \pm 0.2$ and 1.2 ± 0.2 kcal/mol for the cadmium and magnesium samples, respectively. Although the fits to the data of the Mg-dPP sample were worse than those of the Cd-dPP sample, the activation energy for the flipping process in this sample was calculated from the data that assumed the model of motion presented earlier.

In all ^{2}H NMR spectra, the components of Δv_{ii} can be identified for both groups of deuterons (para and ortho/meta). The values of Δv_{ii} do not change as a function of temperature (Figure 6-10 and 6-11) reflecting the absence of any small amplitude librations around an axis perpendicular to the plane of the phenyl ring, or in other words a wobbling of the flip axis.[186] However, for Cd-dPP, at higher temperatures there are some deviations of the simulated spectra from the experimental line shapes in the breadth of the singularities of the spectra. These effects have previously been ascribed to small angle oscillation of the phenyl rings about the C_1-C_4 flip axis.[183] These oscillations may be present at lower temperatures but are not detected in the line shapes because the experimental τ value of 100 μs makes the quadrupole echo sequence more sensitive to motions of faster rates.[186]

Better fits to the Mg-dPP data may be possible if a different model for the molecular motion is assumed. Two possibilities are described below. Because it is difficult to simulate
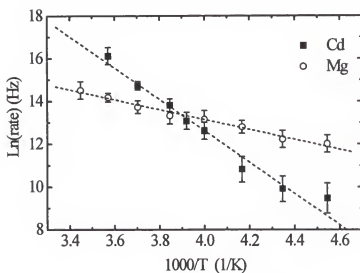
Figure 6-9. Arrhenius plots for the phenyl ring flips in both Cd-dPP and Mg-dPP.

the relative intensities of both the $\Delta v_{XX\text{-moving}}$ and $\Delta v_{XX\text{-static}}$ features in the experimental ^{2}H line shapes at all temperatures, it may be likely that a certain percentage of phenyl rings remain static over the entire temperature range. This model of motion could be implemented by allowing for superposition of f moving phenyl rings and (1-f) static phenyl rings. On the other hand, it is also possible that there are two sets of rings with different flipping rates, with one group being considerably slower than the other. Hence, the simulations would need to consist of the 2 sets of deuterons in a 1:4 ratio (as described above), but now with different flipping rates. In any case, the situation would be simplified if it were possible to synthesize d_4-phenylphosphonic acid with the para position non-deuterated. Then, any occurrence of a static site would be attributed to rings that were not flipping.[183,202] Future work is aimed at solving this question.
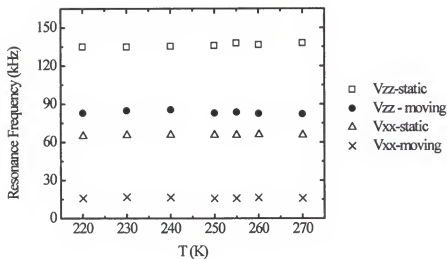
Figure 6-10. Frequencies of the characteristic features of the ^{2}H NMR lineshape as a function of temperature for Cd-*d*PP. The data point size is representative of the error in the measurement.
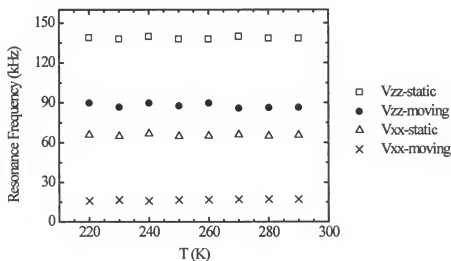
Figure 6-11. Frequencies of the characteristic features of the ^{2}H NMR lineshape as a function of temperature for Mg-*d*PP. The data point size is representative of the error in the measurement.

Conclusions

Dynamical processes in solid state materials that occur on a time scale of milliseconds to tens of microseconds can be studied by deuterium quadrupole echo NMR spectroscopy. Deuterated samples of both cadmium and magnesium phenylphosphonates, $(M(O_3PC_6D_5)H_2O,$ M = Cd, Mg), have been prepared, and the motion of the phenyl groups has been characterized by measuring the deuterium NMR spectra of these samples at a series of temperatures, ranging from the essentially static limit at low temperature to the fast motion regime at higher temperatures where the quadrupole interaction obtains its time-averaged value. The results demonstrate that the phenyl ring motion in both samples occurs by discrete 180° flips around the C_{2v} (C_1-C_4) axis. A linear relationship between 1/T and ln(rate) is obtained, and the activation energy of the flipping process for each sample has been determined.

Differences in the phenyl ring dynamics are detected between the two systems studied, demonstrating that slight differences in the lattice parameters can dramatically affect the molecular dynamics of the phenyl rings in the interlayer galleries. Because many of the phosphonate solids are of interest for their intercalation properties, an understanding of the dynamical processes occurring in these materials is of great importance.

Substrate Preparation

Glass and silicon substrates are first cleaned by sonication in ethanol and dried by a stream of nitrogen (typically, the ATR crystals are not subjected to sonication because of their susceptibility to chipping). The substrates are then cleaned in a piranha etch solution of 3:1 concentrated H_2SO_4 : 30% H_2O_2 for 15-30 minutes (*warning!!*: this solution is potentially explosive around organics, when preparing add acid to the H_2O_2). They are then rinsed with copious amounts of water. The old oxide layer is removed by the RCA base procedure and a new one is formed with the RCA acid procedure. In the RCA base procedure, the substrates are placed into vials containing a 5:1:1 H_2O:30% H_2O_2:conc. NH_4OH at 75 - 85 °C and allowed to sit for 15 minutes (*Caution*: add reagents as written). The RCA acid procedure consists of letting the substrates sit in a 6:1:1 H_2O:30% H_2O_2:conc. HCl at 75 - 85 °C for 15 minutes (*Caution*: add reagents as written). The substrates are then rinsed with copious amounts of nanopure water and dried under a stream of nitrogen.

The formation of a monolayer of OTS proceeds by taking the dried substrates and sonicating them in a solution of 2% by volume OTS in a 1:4 CHCl$_3$:hexadecane solution for 30-60 minutes. The substrates are then sonicated in chloroform to remove any excess OTS and hexadecane. Usually, Soxlett extraction in chloroform is necessary to remove the excess hexadecane.

XPS Calculations

In XPS spectroscopy, a high-energy source of X-rays strikes the surface of the sample, ionizes the atoms and photoelectrons are ejected. Analysis of the XPS data proceeds on the basis of the photoelectic effect, where the kinetic energy of an ejected electron is simply the difference between the source energy and the binding energy of that electron and hence is given by:

$$KE = h\nu - BE \qquad\qquad\qquad (A–1)$$

where KE is the kinetic energy of the photoelectron, $h\nu$ is the energy of the X-ray source and BE is the binding energy of the electron. Since each electron for a given element has a specific binding energy, the observed peaks in the XPS data can be used to identify the elements present in the samples.

Although quantitative information from XPS data is sometimes quite difficult to obtain, we have effectively worked out a procedure for determining the relative percentage of phosphorus and metal ions in the metal phosphonate LB film samples, and this procedure appears to give reliable results. This process consists of integrating the areas of the $P_{2p3/2}$ and appropriate metal ion photoelectron peaks, taking into account instrument sensitivity factors and the photoelectron escape depths. One important aspect to remember when acquiring the XPS multiplex spectra is to have selected the correct photoelectron profile in the set-up parameters. For example, for a given metal ion 2p electron, there may be two signals what correspond to the $2p_{1/2}$ and $2p_{3/2}$ photoelectrons. When these two signals are sufficiently separated, it is best to choose the set-up parameters that contain the sensitivity profiles for integration of only one of the photoelectron peaks. The set-up parameters for integration of both peaks contains an averaged sensitivity factor for both photoelectrons. These parameters are chosen in the set-up Multiplex screen by entering the correct photoelectron name. Often there are two or more choices that correspond to the same energy range, and the differences are in their sensitivity profiles. The profiles can be read in the Semiperm/Element table screens. Consider a hypothetical example.

For manganese, the element names Mn1 and Mn4 may correspond to the energy ranges of the 2p photoelectron signals. An entry of Mn1 in the element table will say either 2p or 2p3 in the entry of photoelectron. This is where one can tell if the sensitivity factor corresponds to only one or both signals. The 2p reading is the average of the two, whereas the 2p3 reading indicates that this profile is specific for the 2p3/2 photoelectron.

To correlate a given stoichiometry of the solid-state metal phosphonate phase to the integrated area from the phosphorus and metal XPS signals of the LB films, corrections for the photoelectron escape depths must be made. These corrections are necessary when the binding energies of the phosphorus and metal ion photoelectrons differ significantly in energy.

The following is an example of how one calculates the areas for a 2:1 P:M stoichiometry of the $CeH(O_3PR)_2$ phase. The relative area of any XPS signal is given by:

$$I_i = \frac{e^{-d_i/\lambda_i \sin\theta}}{\sum_{i=1}^{n} e^{-d_i/\lambda_i \sin\theta}} \tag{A-2}$$

where d_i is the distance of the ion from the surface, θ is the angle that the X-ray source makes with the surface normal, and λ_i is the photoelectron escape depth. One way to calculate the photoelectron escape depth is with expression A-3,

$$\lambda_i = 10\left(\frac{49}{KE^2} + 0.11\sqrt{KE}\right) \tag{A-3}$$

where KE is the kinetic energy of the photoelecton and is calculated by A-1. From the XPS spectrum of the Ce ODP LB film, the $P_{2p3/2}$ photoelectron binding energy is 134.5 eV, giving a value of 1118.2 eV for the kinetic energy of this photoelectron. Likewise, the $Ce_{3d5/2}$ peak appears at 886.3 eV, with a kinetic energy of 367.3 eV (The X-ray source operates at 1253.6 eV in all cases). For this specific example, the photoelectron escape depths are calculated to be:

$$\lambda_P = 10 \left(\frac{49}{1118.2^2} + 0.11\sqrt{1118.2} \right) = 36.7 \text{ Å}, \tag{A-4}$$

$$\lambda_{Ce} = 10 \left(\frac{49}{367.3^2} + 0.11\sqrt{367.3} \right) = 20.7 \text{ Å} \tag{A-5}$$

with the relative area (percentage) of Ce is calculated by:

$$I_{Ce} = \frac{e^{-26/20.7\sin 45}}{e^{-26/20.7\sin 45} + 2e^{-26/36.7\sin 45}} = 0.20 \tag{A-6}$$

and corresponds to 20 % with the phosphorus percentage conversely calculated to be 80%. The value of d_i is determined from X-ray diffraction measurements and is taken as half of the bilayer thickness.

Analysis of XRD Results

The XRD data is acquired with a Phillips APD 3720 X-ray powder difractometer with the CuKα line, λ= 1.54 Å, as the source. The output files are created in JCAMP format. This format contains the intensities acquired for each data point arranged sequentially going across eight columns and as many rows necessary to contain all of the data points. We have written a program called "fixit" which will convert the JCAMP format to a single column of data that contains the XRD intensities for each data point in a sequential order going down the column. The corresponding x-axis values (the 2θ values) can be calculated from the hardcopy output data which contains the initial 2θ value and the step-size. The program works by typing the following command:

```
fixit <JCAMP format filename> <filename for ASCII format>
```
The program code is written in the language perl and the code is given below:

```perl
#!/usr/local/bin/perl -w
# program to extract data from *.udf data files.

unless ($#ARGV == 1){
    print "Usage: fixit <data file> <output file>\n";
    exit;
}

$infile = $ARGV[0];
$outfile = $ARGV[1];

open(IN,$infile) || die "Cannot open $infile for reading: $!\n";
open(OUT,">$outfile") || die "Cannot open $outfile for writing:
$!\n";

# this variable controls whether or not we print out lines.  It's
# not set until we hit the 'RawScan' bit in the text.  From then
on, we
# should just have rows of numbers followed by a trailing '/'
$spigot = 0;
@num = ();

while(<IN>){
if (/^\/$/) {$spigot = 0}
    if ($spigot == 1){
        @nums = split /,?\s+/;
        foreach $num (@nums){
            print OUT "$num\n" if $num =~ /\d+/;
        }
    }
    if (/^RawScan/){$spigot = 1}
}


# Usage: fixit <data file> <output file>
```

EPR Data Analysis

Often when analyzing EPR data, it is necessary to determine the area of the signal. The area of an isotropic EPR signal can easily be calculated by the expression:

$$A = \Delta H_{p-p}^2 * I \tag{A-7}$$

where ΔH_{p-p} is the peak-to-peak line width of the EPR signal, and I is the intensity. These values can easily be read from the data acquisition program SPEX. However, the peak-to-peak linwidth reading is digitized in rather large step sizes so it is best to export the data for analysis by another program. The Covert program will convert the SPEX files (*.SPX) into files that can be read by the EPRDAP program (*.DAT and *.PAR files). After each file is loaded into EPRDAP, each one can be saved as a *.TXT file to be imported into any graphing program such as MicroCal Origin or SigmaPlot.

When the EPR signal is not isotropic, the area must be explicitly integrated. One way to do this is by using a script in MicroCal Origin. Note that the spectra must be baseline corrected or an approximate value for baseline offset must be entered into the script. It is important to realize that the baseline correction in the script can only correct for vertical offsets and not diagonal drifts of the baseline. Also note that the scaling factors of the spectra in the EPRDAP program must be taken into consideration when integrating the areas explicitly. Each change in scale, ie from 10 to 11, corresponds to a factor of 2 enhancement of the vertical scaling. The script for use in MicroCal Origin is as follows:

```
npts=1025;
baseadj=0;
col(4)[i]=0;
for (i=1;i<npts;i+=1){
  A=(col(2)[i]+baseadj+col(2)[i+1]+baseadj)/2*(col(1)[i+1]-
col(1)[i]);
  col(4)[i+1]=col(4)[i]+A;
  col(3)[i+1]=(col(1)[i]+col(1)[i+1])/2;
}
integrate col(4) -b 2;
col(5)[1]=integ.area;
```

Constants and Units

μ_B	= 9.274e-21 erg/G	= 9.274e-24 J/T
k	= 1.381e-16 erg K	= 1.381e-23 J K
h	= 6.626e-27 erg s	= 6.626e-34 J s

emu $\Leftrightarrow$ erg/G^2 $\Leftrightarrow$ J/T^2

Expressions

The spin-only value of the Curie constant, C, is given by expression B-1, where N is Avagadro's number, g is the Lande factor, μ_B is the Bohr magnaton and S is the spin. The value of g can be determined from the EPR spectrum using the relation in B-2, where h is Planks constant, v is the microwave source frequency, and H is the central field of the EPR signal.

$$C = \frac{Ng^2\mu_B^2 S(S+1)}{3k} \tag{B-1}$$

$$hv = g\mu_B H \tag{B-2}$$

Derivation of Expression 4-10

For orthorhombic antiferromagnets, expression 4-10 relates the frequency and field dependence of the two parallel AFMR signals when the applied field has a value less than the spin-flop field. This expressions is derived from a simplification of the following expression which is taken from ref. 160 :

$$
\begin{bmatrix}
\dfrac{-i\omega}{\gamma} & H\{1 + \frac{1}{2}(P_x - P_y)\chi_\parallel\} & 0 & (Q_x - Q_x)M_0 \\
-H\{1 - \frac{1}{2}(P_y - P_x)\chi_\parallel\} & \dfrac{-i\omega}{\gamma} & (Q_y - Q_x)M_0 & 0 \\
0 & 2\{A + \frac{1}{2}(P_y + Q_z)\}M_0 & \dfrac{-i\omega}{\gamma} & H\{1 - [A + \frac{1}{2}(P_z - Q_y)\chi_\parallel]\} \\
-2\{A + \frac{1}{2}(P_y + Q_z)\}M & 0 & -H\{1 - [A + \frac{1}{2}(P_z - Q_y)\chi_\parallel]\} & \dfrac{-i\omega}{\gamma}
\end{bmatrix} \quad (B\text{-}3)
$$

The first simplification is the assumption that $P_x \cong P_y \cong P_z \cong 0$. This approximation is justified from both experimental and theoretical considerations. The original formulation of this theory was for the treatment of AFMR of $CoCl_2 \cdot 6H_2O$ where a second rank tensor **P** was included in the exchange energy expression to account for contributions to the anisotropy energy originating from orbital angular momentum. For our system of Mn^{II}, where $S = 5/2$, it is expected that these effects would be minimal. In addition, if $P_i \neq 0$, fits to the AFMR signals for PERP$_1$, PERP$_2$, and PARA$_{SF}$ (equations (4-1), (4-2), and (4-8)) would have included a non-unity coefficient in front of the H_o^2 term (See equations (18) and (19) of reference 160). Since a non-unity coefficient of the H_o^2 term in these expressions was not necessary to fit our data, this simplification is justified. The second simplification made was the assumption that $A - 1/2Q_z = A + 1/2Q_y = A + 1/2Q_x$ ($A \gg Q_i$) which allowed for the reduction of the expression to a quadratic form. The new matrix expression with $\lambda = [1 - (A + 1/2Q_x)\chi_\parallel]$ now becomes:

$$
\begin{bmatrix}
\dfrac{-i\omega}{\gamma} & H & 0 & (Q_x - Q_x)M_0 \\
-H & \dfrac{-i\omega}{\gamma} & (Q_y - Q_x)M_0 & 0 \\
0 & 2\{A + \frac{1}{2}(Q_z)\}M_0 & \dfrac{-i\omega}{\gamma} & H\lambda \\
-2\{A + \frac{1}{2}(Q_x)\}M & 0 & -H\lambda & \dfrac{-i\omega}{\gamma}
\end{bmatrix} \quad (B\text{-}4)
$$

which has a solution:

$$\frac{\omega}{\gamma} = 28.1 * SQRT\left[\begin{array}{l} R + S + H_0^2\left(1+\lambda^2\right) \\ \pm \sqrt{\left(R+S+H_0^2\left(1+\lambda^2\right)-4\left(H_0^4\lambda^2-H_0^2(R+S)+R*S\right)\right)} \end{array}\right]$$

(B-5,4-10)

$$R = 2\left(Q_x - Q_y\right)M_0^2\left\{A + \tfrac{1}{2}Q_x\right\} \text{(lower zero-field resonance)}$$ (B-6)

$$S = 2\left(Q_x - Q_z\right)M_0^2\left\{A + \tfrac{1}{2}Q_x\right\} \text{(upper zero-field resonance)}$$ (B-7)

where 28.1 is a conversion from units of Tesla to GHz, and λ is temperature dependent since $\chi_\parallel$ is temperature dependent.

Pulse Sequences Used

Phosphorus-31 with Proton Decoupling
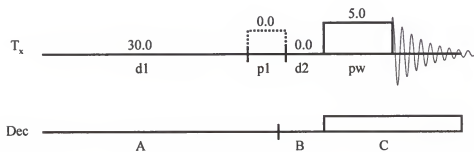
Figure C-1. Varian s2pul sequence .

Phosphorus-31 / Proton Cross-Polarization (CP)
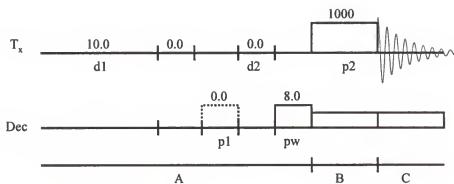
Figure C-2. Varian xpolar pulse sequence.

Quadrupole Echo
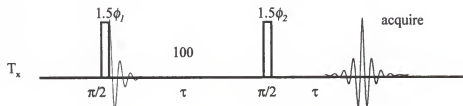
Figure C-3. Quadroploe echo pulse sequence.

Table C-1. Phase Cycling Parameters for Quad-Echo Sequnece.

cycle	$\pi/2\phi_1$	$\pi/2\phi_2$	Phase	ϕ_{acq}
1	x (0)	y (64)	0	0 (0)
2	y (64)	x (128)	180	90 (64)
3	x (128)	y (64)	180	180(124)
4	y (192)	x (128)	0	270(192)
5	x (0)	y (192)	0	0(0)
6	y (64)	x (0)	180	90(64)
7	x (128)	y (192)	180	180(124)
8	y (192)	x (0)	0	270(192)

Spectral Parameters

Phosphorus-31 with Proton Decoupling

Table C-2. Typical Spectral Parameters for the Varian 2pul Pulse Sequence.

	SAMPLE			DEC & VT	
Date		Jun 4 1998	dfreq		499.647
Solvent		NA	dn		H1
file		Zndecyl_spin_01.fid	dpwr		55
	ACQUISITION		dof		74.7
sfrq		202.264	dm		nny
tn		P31	dmm		c
at		0.029	dmf		200
np		5888	dseq		
sw		100000.0	dres		1.0
fb		51200	homo		n
bs		1		PROCESSING	
tpwr		63	lb		100.00
pw		5.0	lsfid		1
d1		30.000	wtfile		
tof		9846.8	proc		ft
nt		64	fn		4096
ct		0	math		i
alock		N			
gain		30	werr		logain
	FLAGS		wexp		wft
il		N	wbs		
in		N	wnt		
dp		Y			
hs		Nn			
	DISPLAY				
sp		-8337.3			
wp		28089.9			
vs		5293			
sc		0			
wc		240			
hzmm		117.04			
is		229.65			
rfl		44048.1			
rfp		0			
th		4			
ins		100.000			
ai		ph			

Phosphorus-31 / Proton CP for Lanthanum Butylphosphonate

Table C-3. Optimized Spectral Paramaters of the Varian xpolar Pulse Sequence for Lanthnum Butylphosphonate.

SAMPLE		DECOUPLING	
Date	Nov 20 1997	dn	H1
Solvent	NA	dof	74.7
file	Labut_CPspin_01.fid	dm	nny
ACQUISITION		dmm	c
sfrq	202.274	dpwr	
tn	P31	level1	
at	0.05	level1f	
np	3968	level2	
sw	40,000	PROCESSING	
xpol	y	lb	50
tpwr	55	lsfid	1
tpwrf	1240	wtfile	not used
pw	8	proc	ft
p1	0	fn	not used
p2	1000	math	i
d1	10	sb	not used
tof	13.4531	gf	not used
nt	4	awc	not used
ct	4	phfid	not used
alock	n		
gain	16	werr	logain
FLAGS		wexp	wft
il	n	wbs	
toss	n	wnt	
pdp	n	SPECIAL	
dp	y	srate	0
DISPLAY		temp	not used
sp	14214.3		
wp	4000		
vs	5385.86		
sc	186.944		
wc	13.0556		
hzmm	160		
is	194205		
rfl	14214.3		
rfp	0		
th	3.67346		
ins	100		
ai	NA		
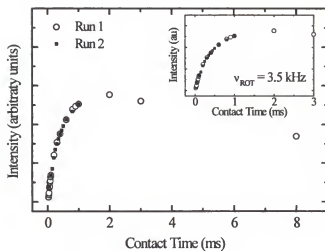
Figure C-4. Contact time dependence for lanthanum butylphosphonate at a spinning rate of 3.5 kHz. Other spectral parameters are given in Table C-3.
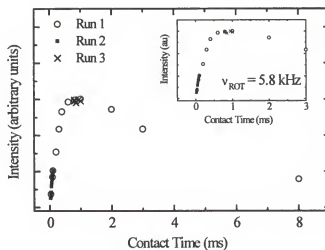
Figure C-5. Contact time dependence for lanthanum butylphosphonate at a spinning rate of 5.8 kHz. Other spectral parameters are given in Table C-3.

Deuterium Quadrupole Echo NMR

Table C-4. Typical Spectral Parameters for the Techmag Quadrupole Echo Pulse Sequence.

Points 1D	4096
Scans 1D	1024
Dummy Scan	16
Scan Count	1024
SW + / -	500000.0
FILTER	51400
Acq. Time	4.096 m
Dwell 1D	1 μs
Obs. Freq.	46.0504000
F1 base	46.0520000
F1 offset	-1.6000 kHz
F2 freq	100.5640000
F2 base	100.5640000
F2 offset	0.000 kHz
RCVR gain	0
DEC Scheme	NA
DEC Power	NA
Sequence	QuadEchoSimple
Last Delay	60 s
PW01	1.45 μs
LB 1D	1000.0
TZ 1 1D	0
TZ 2 1D	51
TZ 3 1D	384
TZ 4 1D	460
Nucleus	H2
Temp K	290
Phase 0	-46.38
Phase 1	0.00
Filename	MgCheck.fid
Spin rate	0
Shift # pts	24
Scans 2D	1
Lock freq	0.000
Field	7.0465630
Print label	None
Solvent	None
Acq. Points	4096

Deuterium Lineshape Simulation Parameters

Table C-5. Spectral Parameters for the Simulated Deuterium NMR Line Shapes.

Spectral Parameter	Sample	
	Cd-*d*PP	Mg-*d*PP
Qcc (kHz)	181 ± 1	181 ± 1
η (P) / (O/M)	0.01 ± 0.005 / 0.03 ± 0.005	0.01 ± 0.005 / 0.03 ± 0.005
lb (Hz)	1000	1000
glb (Hz)	2000	1500

Listed below are the contents of an input file for the deuterium NMR line shape calculation program, calc2, which incorporates the program MXQET. The input file can be written in any Unix text. The calc2 program works by the command:

Calc2 <input-file-name.in> <outputlog-file-name.out>

Note that the outputlog file and the output file are two different files. The output file (OutputFile), which is specified in the input file, will be produced by the calculation and it will contain four columns of data in ASCII format. These are the frequency and intensity data points for the experimental file indicated in the input file and the calculated spectrum, which will be scaled to equivalent intensity if this option is selected in the input file. The outputlog file (outputlog-file-name) will contain information regarding the quality of the fit spectrum. The experimental data file (ExperimentFile) must consist of two columns of data points, which are the real and imaginary points of the experimental spectrum. Therefore, each calculated spectrum will have the following four associated files:

```
1.)Input-file-name.in
2.)outputlog-file-name.out
3.)Experimentfile.dat
4.)OutputFile.xy
```

```
*** contents of <input-file-name.in> ***
num_lineshapes    2                        *number of calc. lineshapes*
num_vars          2                        *number of different 2H sites*
ExperimentFile    cd270_2.dat              *file of the experimental data*
OutputFile        cd270_01.xy              *output file name*
FourierTrans      yes                      *data in the freq(FT) domain*
OutputStyle       gnuplot                  *creates ascii data -4 columns*
Overlay           yes                      *scales the lineshape to exp*
max_iterations    50                       *used for symplex fitting*
tolerance         0.0001                   *symplex tolerence*
sweepwidth        1000000                  *sweepwidth for calculation*
ndp               1024                     *number of data points*
zerofill          1024                     *zero fill points*
num_increments    100                      *increments for linehsape calc*
pulse_width       1.5                      *exp. 90 time*
tau               100                      *exp. pulse spacing*
lb                1000.0                   *lorentzian broadening*
glb               3000.0                   *gaussian broadening*
Qcc               181                      *quadrupole coupling const.*
eta               0.03 0.01                *assymetry parameter of C-D*
flip_rate         2.0e6 1.e-33             *rate of motion*
ratio             4 1                      *ratio of lineshapes*
jump_model        two_site two_site        *model of motion to use*
simplex_params    flip_rate1 Qcc           *variables in simplex fit*
simplex_deltas    5.e4 5                   *tolerance of variables*
```

REFERENCES

(1) de Jongh, L. J. In *Magnetic Properties of Layered Transition Metal Compounds*; L. J. de Jongh, Ed.; Kluwer Academic Publishers: Dordrecht, 1990; pp 1-51.

(2) *Extended Linear Chain Compounds*; Miller, J. S., Ed.; Plenum Press: New York, 1983.

(3) *Solid State Chemistry: Compounds*; Cheetham, A. K.; Day, P., Ed.; Clarendon Press: Oxford, 1992.

(4) Day, P. *Chem. Br.* **1983**, 306-314.

(5) Byrd, H.; Pike, J. K.; Talham, D. R. *Chem. Mater.* **1993**, *5*, 709-715.

(6) Byrd, H.; Whipps, S.; Pike, J. K.; Ma, J.; Nagler, S. E.; Talham, D. R. *J. Am. Chem. Soc.* **1994**, *116*, 295-301.

(7) Byrd, H.; Pike, J. K.; Talham, D. R. *J. Am. Chem. Soc.* **1994**, *116*, 7903-7904.

(8) Byrd, H.; Pike, J. K.; Talham, D. R. *Syn. Met.* **1995**, *71*, 1977-1980.

(9) Seip, C. T.; Byrd, H.; Talham, D. R. *Inorg. Chem.* **1996**, *35*, 3479-3483.

(10) Seip, C. T.; Granroth, G. E.; Meisel, M. W.; Talham, D. R. *J. Am. Chem. Soc.* **1997**, *119*, 7084-7094.

(11) Clearfield, A. In *Progress in Inorganic Chemistry* John Wiley & Sons: NY, 1998; Vol. 47; pp 371-510.

(12) Cao, G.; Hong, H.-G.; Mallouk, T. E. *Acc. Chem. Res.* **1992**, *25*, 420-427.

(13) Clearfield, A. *Comm. Inorg. Chem.* **1990**, *10*, 89-128.

(14) Bujoli, B.; Palvadeau, P.; Rouxel, J. *Chem. Mater.* **1990**, *2*, 582-589.

(15) Drumel, S.; Janvier, P.; Barboux, P.; Bujoli-Doeff, M.; Bujoli, B.; *Inorg. Chem.* **1995**, *34*, 148-156.

(16) Cao, G.; Lee, H.; Lynch, V. M.; Mallouk, T. E. *Inorg. Chem.* **1988**, *27*, 2781-2785.

(17) Cao, G.; Lee, H.; Lynch, V. M.; Mallouk, T. E. *Solid State Ionics* **1988**, *26*, 63-69.

(18) Alberti, G.; Casciola, M.; Costantino, U.; Vivani, R. *Adv. Mater.* **1996**, *8*, 291-303.

(19) Le Bideau, J.; Payen, C.; Palvadeau, P.; Bujoli, B. *Inorg. Chem.* **1994**, *33*, 4885-4890.

(20) Clearfield, A.; Smith, G. D. *Inorg. Chem.* **1969**, *8*, 431-436.

(21) Alberti, G.; Costantino, U.; Allulli, S.; Tomassini, N. *J. Inorg. Nucl. Chem.* **1978**, *40*, 1113-1117.

(22) Carling, S. G.; Day, P.; Visser, D.; Kremer, R. K. *J. Solid State Chem.* **1993**, *106*, 111-119.

(23) Carling, S. G.; Day, P.; Visser, D. *J. Phys.: Condens. Matter.* **1995**, *7*, L109-L113.

(24) Dines, M. B.; DiGiacomo, P. M. *Inorg. Chem.* **1981**, *20*, 92-97.

(25) Katz, H. E.; Bent, S. F.; Wilson, W. L.; Schilling, M. L.; Ungashe, S. B. *J. Am. Chem. Soc.* **1994**, *116*, 6631-6635.

(26) Thompson, M. E. *Chem. Mater.* **1994**, *6*, 1168-1175.

(27) Vermeulen, L. A.; Snover, J. L.; Sapochak, L. S.; Thompson, M. E. *J. Am. Chem. Soc.* **1993**, *115*, 11767-11774.

(28) Cunningham, D.; Hennelly, P. J. D. *Inorg. Chim. Acta* **1979**, *37*, 95-102.

(29) Cao, G.; Lynch, V. M.; Swinnea, J. S.; Mallouk, T. E. *Inorg. Chem.* **1990**, *29*, 2112-2117.

(30) Bujoli, B.; Pena, O.; Palvadeau, P.; Le Bideau, J.; Payen, C.; Rouxel, J. *Chem. Mater.* **1993**, *5*, 583-587.

(31) Bellitto, C.; Federici, F. *Chem. Mater.* **1998**, *10*, 1076-1082.

(32) Cao, G.; Lynch, V. M.; Yacullo, L. N. *Chem. Mater.* **1993**, *5*, 1000-1006.

(33) Johnson, J. W.; Jacobson, A. J.; Brody, J. F.; Lewandowski, J. T. *Inorg. Chem.* **1984**, *23*, 3842-3844.

(34) Johnson, J. W.; Brody, J. F.; Alexander, R. M.; Pilarski, B.; Katritzky, A. R. *Chem. Mater.* **1990**, *2*, 198-201.

(35) Ortiz-Avila, Y.; Rudolf, P. R.; Clearfield, A. *Inorg. Chem.* **1989**, *28*, 2137-2141.

(36) Poojary, D. M.; Zhang, B.; Cabeza, A.; Aranda, M. A. G.; Bruque, S.; Clearfield, A. *J. Mater. Chem.* **1996**, *6*, 639-644.

(37) Wang, R.-C.; Zhang, Y.; Hu, H.; Frausto, R. R.; Clearfield, A. *Chem. Mater.* **1992**, *4*, 864-870.

(38) Zhang, Y.; Clearfield, A. *Inorg. Chem.* **1992**, *31*, 2821-2826.

(39) Martin, K. J.; Squattrito, P. J.; Clearfield, A. *Inorg. Chim. Acta* **1989**, *155*, 7-9.

(40) Frink, K. J.; Wang, R.-C.; Colón, J. L.; Clearfield, A. *Inorg. Chem.* **1991**, *30*, 1438-1441.

(41) Cao, G.; Mallouk, T. E. *Inorg. Chem.* **1991**, *30*, 1434-1438.

(42) Burwell, D. A.; Thompson, M. E. *Chem. Mater.* **1991**, *3*, 730-737.

(43) Poojary, M. D.; Hu, H.-L.; Campbell, I., F. L.; Clearfield, A. *Acta Cryst. B* **1993**, *49*, 996.

(44) Le Bideau, J.; Bujoli, B.; Jouanneaux, A.; Payen, C.; Palvadeau, P.; Rouxel, J. *Inorg. Chem.* **1993**, *32*, 4617-4620.

(45) Zhang, Y.; Scott, K. J.; Clearfield, A. *Chem. Mater.* **1993**, *5*, 495-499.

(46) Huan, G.; Jacobson, A. J.; Johnson, J. W.; E. W. Corcoran, J. *Chem. Mater.* **1990**, *2*, 91-93.

(47) Huan, G.; Jacobson, A. J.; Johnson, J. W.; Goshorn, D. P. *Chem. Mater.* **1992**, *4*, 661-665.

(48) Le Bideau, J.; Papoutsakis, D.; Jackson, J. E.; Nocera, D. *J. Am. Chem. Soc.* **1997**, *119*, 1313-1316.

(49) Carlin, R. L. *Magnetochemistry;* 1st ed.; Springer-Verlag: Berlin, 1986.

(50) Palacio, E. In *Molecular Magnetism: From Molecular Assemblies to the Devices*; E. Coronado, P. Delhaes, D. Gatteschi and J. S. Miller, Ed.; Kluwer Academic Publishers: Boston, 1996; Vol. 321.

(51) Kahn, O.; Pei, Y.; Nakatani, K.; Journaux, Y.; Sletten, J. *New J. Chem.* **1992**, *16*, 269-276.

(52) Carling, S. G.; Day, P.; Visser, D. *Inorg. Chem.* **1995**, *34*, 3917-3927.

(53) Visser, D.; Carling, S. G.; Day, P.; Deportes, J. *J. Appl. Phys.* **1991**, *69*, 6016-6018.

(54) Boersma, F. L.; de Jonge, W. J. L.; Kopinga, K. *Phys. Rev. B* **1981**, *23*, 186-214.

(55) de Jongh, L. J.; Miedema, A. R. *Adv. Phys.* **1974**, *24*, 1-260.

(56) Coronado, E.; Tsukerblat, B. S.; Gorges, R. In *Molecular Magnetism: From Molecular Assemblies to the Devices*; E. Coronado, P. Delhaes, D. Gatteschi and J. S. Miller, Ed.; Kluwer Academic Publishers: Boston, 1996; Vol. 321.

(57) Wynn, C. M.; Girtu, M. A.; Brinckerhoff, W. B.; Sugiura, K. I.; Miller, J. S.; Epstein, A. J. *Chem. Mater.* **1997**, *9*, 2156-2163.

(58) Onsager, L. *Phys. Rev.* **1944**, *65*, 117-149.

(59) Pokrovsky, V. L.; Uimin, G. V. In *Magnetic Properties of Layered Transition Metal Compounds*; L. J. de Jongh, Ed.; Kluwer Academic: Dordrecht, 1990; pp 53-103.

(60) Bloch, F. *Z. Phys.* **1930**, *61*, 206.

(61) Johnston, D. C.; Johnson, J. W.; Goshorn, D. P.; Jacpbson, A. J. *Phys. Rev. B* **1987**, *35*, 219-222.

(62) Barnes, T.; Riera, J. *Phys. Rev. B* **1994**, *50*, 6817-6822.

(63) Garrett, A. W.; Nagler, S. E.; Tennant, D. A.; Sales, B. C.; Barnes, T. *Phys. Rev. Lett.* **1997**, *79*, 745-748.

(64) Tennant, D. A.; Nagler, S. E.; Garrett, A. W.; Barnes, T.; Torardi, C. C. *Phys. Rev. Lett.* **1997**, *78*, 4998-5001.

(65) Le Bideau, J.; Payen, C.; Bujoli, B.; Palvadeau, P.; Rouxel, J. *J. Magn. Magn. Mater.* **1995**, *140-144*, 1719-1720.

(66) Hay, P. J.; Thibeault, J. C.; Hoffman, R. *J. Am. Chem. Soc.* **1975**, *97*, 4884-4899.

(67) Weihe, H.; Gudel, H. U. *J. Am. Chem. Soc.* **1997**, *119*, 6539-6543.

(68) Crawford, V. H.; Richardson, H. W.; Wasson, J. R.; Hodgson, D. J.; Hatfield, W. E. *Inorg. Chem.* **1976**, *15*, 2107-2110.

(69) Bencini, A.; Gatteschi, D. *Inorg. Chim. Acta* **1978**, *31*, 11-18.

(70) Guliants, V. V.; Benzinger, J. B.; Sundaresan, S. *Chem. Mater.* **1995**, *7*, 1493-1498.

(71) Beltran-Porter, D.; Amoros, P.; Ibanez, R.; Martinez, E.; Beltran-Porter, A.; Le Bail, A.; Ferey, G.; Villeneuve, G. *Solid State Ionics* **1989**, *32/33*, 57-69.

(72) Kahn, O. *Molecular Magnetism*; VCH Publishers, Inc.: New York, New York, 1993.

(73) Jeter, D. Y.; Lewis, D. L.; Hempel, J. C.; Hodgson, D. J.; Hatfield, W. E. *Inorg. Chem.* **1972**, *11*, 1958-1960.

(74) Willet, R. D.; Gatteschi, D.; Kahn, O. *Magneto-Structural Correlations in Exchange Coupled Systems*; D. Reidel Publishing Company: Dordrecht, 1985.

(75) Kahn, O.; Galy, J.; Journaux, Y.; Jaud, J.; Morgenstern-Badarau, I. *J. Am. Chem. Soc.* **1982**, *104*, 2165-2176.

(76) Kahn, O.; Briat, B. *J. Chem. Soc. Farad. Trans. II* **1976**, *72*, 268-281.

(77) Hayward, C. A.; Poilblanc, D.; Levy, L. P. *Phys. Rev. B* **1996**, *18*, 12649-12652.

(78) Lines, M. E. *J. Phys. Chem. Solids* **1970**, *31*, 101-116.

(79) Ulman, A. *An Introduction to Ultrathin Organic Films: From Langmuir-Blodgett to Self-Assembly*; Academic Press: Boston, 1991.

(80) Coradin, T.; Backov, R.; Jones, D. J.; Roziere, J.; Clement, R. *Mol. Cryst. Liq. Cryst.* **1998**, *311*, 275.

(81) Backov, R.; Jones, D. J.; Roziere, J. *J. Chem. Soc., Chem. Commun.* **1996**, 599-601.

(82) Backov, R.; Bonnet, B.; Jones, D. J.; Roziere, J. *Chem. Mater.* **1997**, *9*, 1812.

(83) Roberts, G. G. *Langmuir-Blodgett Films*; Plenum Press: New York, 1990.

(84) Maoz, R.; Sagiv, J. *J. Colloid Interface Sci.* **1984**, *100*, 465-496.

(85) Wasserman, S. R.; Tao, Y.-T.; Whitesides, G. M. *Langmuir* **1989**, *5*, 1074-1087.

(86) Bain, C. D.; Troughton, E. B.; Tao, Y.-T.; Evall, J.; Whitesides, G. M.; Nuzzo, R. G. *J. Am. Chem. Soc.* **1989**, *111*, 321-335.

(87) Laibinis, P. E.; Whitesides, G. M.; Allara, D. L.; Tao, Y.-T.; Parikh, A. N.; Nuzzo, R. G. *J. Am. Chem. Soc.* **1991**, *113*, 7152-7167.

(88) Laibinis, P. E.; Whitesides, G. M. *J. Am. Chem. Soc.* **1992**, *114*, 1990-1995.

(89) Caldwell, W. B.; Campbell, D. J.; Chen, K.; Herr, B. R.; Mirkin, C. A.; Malik, A.; Durbin, M. K.; Dutta, P.; Huang, K. G. *J. Am. Chem. Soc.* **1995**, *117*, 6071-6082.

(90) Ritchie, J. E.; Wells, C. A.; Zhou, J.-P.; Zhao, J.; McDevitt, J. T.; Ankrum, C. R.; Jean, L.; Kanis, D. R. *J. Am. Chem. Soc.* **1998**, *120*, 2733-2745.

(91) Zhu, J.; Xu, F.; Schofer, S. J.; Mirkin, C. A. *J. Am. Chem. Soc.* **1997**, *119*, 235-236.

(92) Clevenger, M. B.; Zhao, J.; McDevitt, J. T. *Chem. Mater.* **1996**, *8*, 2693-2696.

(93) Xu, F.; Chen, K.; Piner, R. D.; Mirkin, C. A.; Ritchie, J. E.; McDevitt, J. T.; Cannon, M. O.; Kanis, D. *Langmuir* **1998**, *14*, 6505-6511.

(94) Hong, H.-G.; Sackett, D. D.; Mallouk, T. E. *Chem. Mater.* **1991**, *3*, 521-527.

(95) Gao, W.; Dickinson, L.; Grozinger, C.; Morin, F. G.; Reven, L. *Langmuir* **1996**, *12*, 6429 - 6435.

(96) Netzer, L.; Sagiv, J. *J. Am. Chem. Soc.* **1983**, *105*, 674-676.

(97) Lee, H.; Kepley, L. J.; Hong, H.-G.; Mallouk, T. E. *J. Am. Chem. Soc.* **1988**, *110*, 618-620.

(98) Lee, H.; Kepley, L. J.; Hong, H.-G.; Akhter, S.; Mallouk, T. E. *J. Phys. Chem.* **1988**, *92*, 2597-2601.

(99) Akhter, S.; Lee, H.; Hong, H.-G.; Mallouk, T. E.; White, J. M. *J. Vac. Sci. Technol.* **1989**, *7*, 1608-1613.

(100) Yang, H. C.; Aoki, K.; Hong, H.-G.; Sackett, D. D.; Arendt, M. F.; Yau, S.-L.; Bell, C. M.; Mallouk, T. E. *J. Am. Chem. Soc.* **1993**, *115*, 11855-11862.

(101) Kepley, L. J.; Sackett, D. D.; Bell, C. M.; Mallouk, T. E. *Thin Solid Films* **1992**, *208*, 132-136.

(102) Katz, H. E.; Scheller, G.; Putvinski, T. M.; Schilling, M. L.; Wilson, W. L.; Chidsey, C. E. D. *Science* **1991**, *254*, 1485-1487.

(103) Katz, H. E.; Wilson, W. L.; Scheller, G. *J. Am. Chem. Soc.* **1994**, *116*, 6636-6640.

(104) Katz, H. E.; Schilling, M. L. *Chem. Mater.* **1993**, *5*, 1162-1166.

(105) Ungashe, S. B.; Wilson, W. L.; Katz, H. E.; Scheller, G. R.; Putvinski, T. M. *J. Am. Chem. Soc.* **1992**, *114*, 8717-8719.

(106) Talham, D. R.; Seip, C. T.; Whipps, S.; Fanucci, G. E.; Petruska, M. A.; Byrd, H. *Comments Inorg. Chem.* **1997**, *19*, 133-151.

(107) Blodgett, K. B. *J. Am. Chem. Soc.* **1935**, *57*, 1007.

(108) Byrd, H.; Pike, J. K.; Talham, D. R. *Thin Solid Films* **1994**, *242*, 100-105.

(109) Byrd, H.; Pike, J. K.; Showalter, M. L.; Whipps, S.; Talham, D. R. In *Interfacial Design and Chemical Sensing*; T. E. Mallouk and D. J. Harrison, Ed.; American Chemical Society: Washington, 1994; Vol. ACS Symposium Series 561; pp 49-59.

(110) Byrd, H.; Whipps, S.; Pike, J. K.; Talham, D. R. *Thin Solid Films* **1994**, *244*, 768-771.

(111) Fanucci, G. E.; Seip, C. T.; Petruska, M. A.; Ravaine, S.; Nixon, C. M.; Talham, D. R. *Thin Solid Films* **1998**, *327-329*, 331-335.

(112) Kern, W. *J. Electrochem. Soc.* **1990**, *137*, 1887-1892.

(113) Ganguly, P.; Paranjape, D. V.; Sastry, M.; Chaudhari, S. K.; R., p. K. *Langmuir* **1993**, *9*, 487 - 490.

(114) Linden, D. M. J.; Peltonen, J. P. K.; Rosenholm, J. B. *Langmuir* **1994**, *10*, 1592-2595.

(115) Linden, M.; Rosenholm, J. B. *Langmuir* **1995**, *11*, 4499 - 4504.

(116) Pike, J. K.; Byrd, H.; Morrone, A. A.; Talham, D. R. *Chem. Mater.* **1994**, *6*, 1757-1765.

(117) Brundle, C. R.; Hopster, H.; Swalen, J. D. *J. Chem. Phys.* **1979**, *70*, 5190-5196.

(118) Seah, M. P.; Dench, W. A. *Surf. Interface Anal.* **1979**, *1*, 1-11.

(119) Porter, M. D.; Bright, T. B.; Allara, D. L.; Chidsey, C. E. D. *J. Am. Chem. Soc.* **1987**, *109*, 3559-3568.

(120) Wood, K. A.; Snyder, R. G.; Strauss, H. L. *J. Chem. Phys.* **1989**, *91*, 5255-5267.

(121) Bellamy, L. J. *The Infra-red Spectra of Complex Molecules;* 3rd ed.; Chapman and Hall: London, 1975.

(122) Bellamy, L. J. *Advances in Infrared Group Frequencies;* 2 ed.; Chapman and Hall: London, 1975.

(123) Frey, B. L.; Hanken, D. G.; Corn, R. M. *Langmuir* **1993**, *9*, 1815-1820.

(124) Wulfsberg, G. *Principles of Descriptive Inorganic Chemistry*; University Science Books: Mill Valley, 1991, pp pp 25.

(125) Bryce, M. R.; Petty, M. C. *Nature* **1995**, *374*, 771-776.

(126) Pomerantz, M.; Pollak, R. A. *Chem. Phys. Lett.* **1975**, *31*, 602-604.

(127) Pomerantz, M. In *NATO ASI Series - Phase Transitions in Surface Films*; J. G. Dash and J. Ruvalds, Ed.; Plenum: New York, 1980; pp 317-346.

(128) Clement-Leon, M.; Mingotaud, C.; Agricole, B.; Gomez-Garcia, C.; Coronado, E.; Delhaes, P. *Angew. Chem. Int. Ed. Engl.* **1997**, *36*, 1114-1116.

(129) Petruska, M. A.; Fanucci, G. E.; Talham, D. R. *Chem. Mater.* **1998**, *10*, 177-189.

(130) Petruska, M. A.; Fanucci, G. E.; Talham, D. R. *Thin Solid Films* **1998**, *327-329*, 131-135.

(131) Ries Jr, H. E.; Cook, H. D. *J. Colloid Sci* **1954**, *9*, 535-546.

(132) Tillman, N.; Ulman, A.; Schildkraut, J. S.; Penner, T. L. *J. Am. Chem. Soc.* **1988**, *110*, 6136-6144.

(133) *5000 Series ESCA Systems Version 2.0 Instruction Manual*; Perkin-Elmer Physical Electronics Division: Eden Prairie, MN, 1989.

(134) Siegbahn, K.; Nordling, C.; Fahlman, A.; Nordberg, R.; Hamrin, K.; Hedman, J.; Johansson, G.; Bergmark, T.; Karlsson, S.-E.; Lindgren, I.; Lindberg, B. *ESCA; Atomic, Molecular, and Solid State Structure by Means of Electron Spectroscopy;* 0 ed.; Almqvist & Wiksells: Uppsala, 1967.

(135) *Perkin Elmer Handbook of X-Ray Photoelectron Spectroscopy;* 0 ed.; Perkin Elmer Physical Electronics Division: Eden Prairie, MN, 1994.

(136) Cammarata, V.; Atanasoska, L.; Miller, L. L.; Kolaskie, C. J.; Stallman, B. J. *Langmuir* **1992**, *8*, 876-886.

(137) Varsanyi, G. *Vibrational Spectra of Benzene Derivatives*; Academic: New York, 1969.

(138) Benner, H.; Boucher, J. P. In *Magnetic Properties of Layered Transition Metal Compounds*; L. J. de Jongh, Ed.; Kluwer Academic: Dordrecht, 1990; pp 323-378.

(139) Foner, S. In *Magnetism*; G. T. Rado and H. Suhl, Ed.; Academic Press: 1963; Vol. 1; pp 383-447.

(140) Fanucci, G. E.; Krzystek, J.; Meisel, M. W.; Brunel, L.-C.; Talham, D. R. *J. Am. Chem. Soc.* **1998**, *120*, 5469 - 5479.

(141) Moriya, T. *Phys. Rev.* **1960**, *120*, 91-98.

(142) Endoh, Y.; Yamada, K.; Birgeneau, R. J.; Gabbe, D. R.; Jenssen, H. P.; Kastner, M. A.; Peters, C. J.; Picone, P. J.; Thurston, T. R.; Tranquada, J. M.; Shirane, G.; Hidaka, Y.; Oda, M.; Enomoto, Y.; Suzuki, M.; Murakami, T. *Phys. Rev. B* **1988**, *37*, 7443-7453.

(143) Elstner, N.; Sokol, A.; Singh, R. R. P.; Greven, M.; Birgeneau, R. J. *Phys. Rev. Lett.* **1995**, *75*, 938-941.

(144) Kittel, C. *Phys. Rev.* **1951**, *82*, 565.

(145) Keffer, F.; Kittel, C. *Phys. Rev.* **1952**, *85*, 329-337.

(146) Nagamiya, T. *Progr. Theoret. Phys.* **1954**, *11*, 209-327.

(147) Hagiwara, M.; Katsumata, K.; Tuchendler, J. *J. Phys.: Condens. Matter* **1994**, *6*, 545-550.

(148) Katsumata, K.; Tuchendler, J. *J. Phys. C: Solid State Phys.* **1987**, *20*, 4873-4879.

(149) Ohta, H.; Yoshida, K.; Matsuya, T.; Nanba, T.; Motokawa, M.; Yamada, K.; Endoh, Y.; Hosoya, S. *J. Phys. Soc. Jpn.* **1992**, *61*, 2921-2929.

(150) Ohta, H.; Yamauchi, N.; Nanba, T.; Motokawa, M.; Kawamata, S.; Okuda, K. *J. Phys. Soc. Japan* **1993**, *62*, 785-792.

(151) Ohta, H.; Kimura, S.; Motokawa, M. *J. Phys. Soc. Jpn.* **1995**, *64*, 3934-3940.

(152) Ohta, H.; Sumikawa, M.; Motokawa, M.; Noro, S.; Yamadaya, T. *J. Phys. Soc. Jpn.* **1995**, *64*, 1759-1765.

(153) Yoshioka, H.; Saiki, K. *J. Phys. Soc. Jpn.* **1972**, *33*, 1566-1573.

(154) Saiki, K. *J. Phys. Soc. Jpn.* **1972**, *33*, 1284-1291.

(155) Clearfield, A. *Chem. Rev.* **1988**, *88*, 125-148.

(156) Besset, H.; Baldwell, W. L. *J. Chem. Soc.* **1933**,

(157) Dzyaloshinsky, I. *J. Phys. Chem. Solids* **1958**, *4*, 241-255.

(158) Kittel, C. *Introduction to Solid State Physics;* 6th ed.; John Wiley & Sons: New York, 1986.

(159) Nagamiya, T.; Yosida, K.; Kubo, R. *Adv. Phys.* **1955**, *4*, 1-112.

(160) Date, M. *J. Phys. Soc. Japan* **1961**, *16*, 1337-1351.

(161) Date, M.; Nagata, K. *J. Appl. Phys.* **1963**, *34*, 1038-1044.

(162) Tavs, P. *Chem. Ber.* **1979**, *103*, 2428.

(163) Grabiak, R. C.; Miles, J. A.; Schwenzer, G. M. *Phosphorus and Sulfur* **1980**, *9*, 197-202.

(164) Mueller, F.; Hopkins, M. A.; Coron, N.; Grynberg, M.; Brunel, L. C.; Martinez, G. *Rev. Sci. Instr.* **1989**, *60*, 3681.

(165) Pincus, P. *Phys. Rev. Lett.* **1960**, *5*, 13-15.

(166) Gurevitch, A. G.; Sanina, V. A.; Golovenchitis, E. I.; Starobinets, S. S. *J. Appl. Phys.* **1969**, *40*, 1512-1517.

(167) Herrmann, G. F. *J. Phys. Chem. Solids* **1963**, *24*, 597-606.

(168) Norman, R. E.; Yan, S.; Que, J. L.; Backes, G.; Ling, J.; Sanders-Loehr, J.; Zhang, J. H.; O'Conner, C. J. *J. Am. Chem. Soc.* **1990**, *112*, 1554-1562.

(169) Moriya, T. *Phys. Rev.* **1960**, *117*, 635-647.

(170) Opella, S. J. In *Biological NMR spectroscopy*; J. L. Markley and S. J. Opella, Ed.; Oxford University Press: Oxford, 1997.

(171) Davis, F.; Heatley, F.; Hodge, P.; Towns, C. *Polymer* **1994**, *35*, 885 - 887.

(172) Mehring, M. *Principles of High resolution NMR in Solids*; Springer-Verlag: Berlin, 1983.

(173) Chmelka, B. F.; Schmit-Rohr, K.; Spiess, H. W. In *Nuclear Magetic Resonance Probes of Molecular Dynamics*; R. Tycko, Ed.; Kluwer Academic Publishers: Boston, 1994; pp 113-153.

(174) Mingotaud, A.-F.; Mingotaud, C.; Patterson, L. K. *Handbook of Monolayers;* 1st ed.; Academic Press: London, 1993; Vol. 1, pp 1378.

(175) Gao, W.; Reven, L. *Langmuir* **1995**, *11*, 1860 - 1863.

(176) Gao, W.; Dickinson, L.; Morin, F. G.; Reven, L. *Chem. Mater.* **1997**, *9*, 3113 - 3120.

(177) Massiot, D.; Drumel, S.; Janvier, P.; Bujoli-Doeuff, M.; Bujoli, B. *Chem. Mater.* **1997**, *9*, 6 - 7.

(178) Burwell, D., A.; Valentine, K. G.; Timmermans, J., H.; Thompson, M. E. *J. Am. Chem. Soc.* **1992**, *114*, 4144-4150.

(179) Burwell, D. A.; Valentine, K. G.; Thompson, M. E. *J. Magn. Reson.* **1992**, *97*, 498-510.

(180) Neff, G. A.; Page, C. J.; Meintjes, E.; Tsuda, T.; Pilgrim, W.-C.; Roberts, N.; Warren, W. W. J. *Langmuir* **1996**, *12*, 238-242.

(181) Zhang, B.; Poojary, D., M.; Clearfiled, A. *Inorg. Chem.* **1998**, *1998*, 1844-1852.

(182) Vold, R. R. In *Nuclear Magentic Resonance Probes of Molecular Dynamics*; R. Tycko, Ed.; Kluwer Academin Publishers: Boston, 1994; pp 27-112.

(183) Cholli, A. L.; Dumais, J. J.; Engel, A. K.; Jelinski, L. W. *Macromolecules* **1984**, *17*, 2399-2404.

(184) Henrichs, P. M.; Hewitt, J. M.; Linder, M. *J. Magn. Reson.* **1984**, *60*, 280-298.

(185) Vega, A. J.; Luz, Z. *J. Chem. Phys.* **1987**, *86*, 1803-1813.

(186) Greenfield, M. S.; Ronemus, A. D.; Vold, R. L.; Vold, R. R.; Ellis, P. D.; Raidy, T. E. *J. Magn. Reson.* **1987**, *72*, 89-107.

(187) Abragam, A. *Principles of Nuclear Magnetic Resonance*; Oxford University Press: London, 1985.

(188) *Nuclear Magnetic Resonance Probes of Molecular Dynamics*; Kluwer Acvademic Publishers: Boston, 1994.

(189) Speiss, H. W. *J. Chem. Phys.* **1980**, *72*, 6755-6761.

(190) Wittebort, R. J.; Olejniczak, E. T.; Griffin, R. G. *J. Chem. Phys.* **1987**, *86*, 5411-5420.

(191) Smith, R. L.; Oldfield, E. *Science* **1984**, *225*, 280-288.

(192) Griffin, R. G. *Meth. Enzymol.* **1981**, *72*, 108-156.

(193) Lin, T. H.; DiNitale, J. A.; Vold, R. R. *J. Am. Chem. Soc.* **1994**, *116*, 2133-2134.

(194) Roy, A. K.; Jones, A. A.; Inglefield, P. T. *J. Magn. Reson.* **1985**, *64*, 441.

(195) Rice, D. M.; Meinwald, Y. C.; Scheraga, H. A.; Griffin, R. G. *J. Am. Chem. Soc.* **1987**, *109*, 1636-1640.

(196) Rice, D. M.; Wittebort, R. J.; Griffin, R. G.; Meirovitch, E.; Stimson, E. R.; Meinwald, Y. C.; Freed, J. H.; Scheraga, H. A. *J. Am. Chem. Soc.* **1981**, *103*, 7707-7710.

(197) Gall, C. M.; Cross, T. A.; DiVerdi, J. A.; Opella, S. J. *Proc. Nat. Acad. Sci. USA* **1982**, *79*, 101.

(198) Speiss, H. W.; Sillescu, H. *J. Magn. Reson.* **1981**, *42*, 381-389.

(199) Bloom, M.; Davis, J. H.; Valic, M. I. *Can. J. Phys.* **1980**, *38*, 1510-1517.

(200) Price, W. S.; Hayamizu, K. *J. Magn. Res. Ser. A* **1995**, *114*, 73-79.

(201) Siminovitch, D. J.; Raleigh, D. P.; Olenjniczak, E. T.; Griffin, R. G. *J. Chem. Phys.* **1986**, *84*, 2556.

(202) Hiyama, Y.; Silverton, J. V.; Torchia, D. A.; Gerig, J. T.; Hammond, S. J. *J. Am. Chem. Soc.* **1986**, *108*, 2715-2723.

BIOGRAPHICAL SKETCH

Gail E. Fanucci was born in Scranton, Pennsylvania, on February 20, 1972. She lived with parents Joyce and Steve Lesavage in Scranton throughout high school and remained in Scranton for college where she attended the University of Scranton. Gail graduated with a B.S. in biochemistry and a B.S. in biophysics from the University of Scranton in May 1994.

In the summer of 1994 Gail married Theodore J. Fanucci and then shortly afterwards moved to Gainesville, Florida to attend graduate school at the University of Florida starting in the fall of 1994.

In December 1994, she joined the research group of Daniel R. Talham. After 4.5 years under his supervision, Gail defended her dissertation and graduated from the University of Florida with a PhD in chemistry.
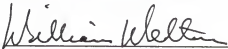
I certify that I have read this study and that in my opinion it conforms to acceptable standards of scholarly presentation and is fully adequate, in scope and quality, as a dissertation for the degree of Doctor of Philosophy.

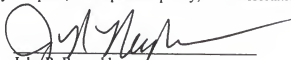Daniel R. Talham, Chairman
Associate Professor of Chemistry

I certify that I have read this study and that in my opinion it conforms to acceptable standards of scholarly presentation and is fully adequate, in scope and quality, as a dissertation for the degree of Doctor of Philosophy.

C. Russell Bowers,
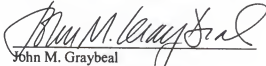Assistant Professor of Chemistry

I certify that I have read this study and that in my opinion it conforms to acceptable standards of scholarly presentation and is fully adequate, in scope and quality, as a dissertation for the degree of Doctor of Philosophy.

William Weltner
Professor of Chemistry

I certify that I have read this study and that in my opinion it conforms to acceptable standards of scholarly presentation and is fully adequate, in scope and quality, as a dissertation for the degree of Doctor of Philosophy.

John R. Reynolds
Professor of Chemistry

I certify that I have read this study and that in my opinion it conforms to acceptable standards of scholarly presentation and is fully adequate, in scope and quality, as a dissertation for the degree of Doctor of Philosophy.

John M. Graybeal
Associate Professor of Physics

This dissertation was submitted to the Graduate Faculty of the Department of Chemistry in the College of Liberal Arts and Sciences and to the Graduate School and was accepted as partial fulfillment of the requirements for the degree of Doctor of Philosophy.

May 1999

Dean, Graduate School